2003

Crevassing and Calving of Glacial Ice

James Patrick Kenneally

CREVASSING AND CALVING OF GLACIAL ICE

By

James Patrick Kenneally

B.S. Rensselaer Polytechnic Institute, 1995

M.S. University of California San Diego, 1998

A THESIS

Submitted in Partial Fulfillment of the

Requirements for the Degree of

Doctor of Philosophy

(in Physics)

The Graduate School

The University of Maine

August, 2003

Advisory Committee:

Terence Hughes, Professor of Geological Sciences, Advisor

James Fastook, Professor of Computer Science

Roger Hooke, Research Professor of Geological Sciences

Peter Kleban, Professor of Physics

Donald Mountcastle, Associate Professor of Physics

External Reader:

Brian Hanson, Associate Professor of Geography, University of Delaware

CREVASSING AND CALVING OF GLACIAL ICE

By James Patrick Kenneally

Thesis Advisor: Dr. Terence Hughes

An Abstract of the Thesis Presented
in Partial Fulfillment of the Requirements for the
Degree of Doctor of Philosophy
(in Physics)

August, 2003

Calving of ice is a relatively new area of research in the still young field of glaciology. In the short time that calving has been studied, it has been mainly treated as an afterthought, with the predominant mode of thinking being that it will happen so to concern oneself with why is not important. Many studies dealt with observations of calving front positions over time vs. ice velocity in an attempt to quantify the calving rate as the difference between the two, while others have attempted to deduce some empirical relationship between calving rate and variables such as water depth or temperature. This study instead addresses the question of why, where, and when ice will first become crevassed, which is an obviously necessary condition for a later calving event to occur. Previous work examining the causes of calving used ideas put forth from a variety of fields, including civil engineering, materials science, and results from basic physics and mechanics. These theories are re-examined here and presented as part of a larger whole. Important results from the field of fracture mechanics are utilized frequently, and these results can be used as a predictor of ice behavior and

intrinsic properties of ice, as well as properties like back stresses induced by local pinning points and resistive shears along glacial ice boundaries. A theory of fracture for a material experiencing creep is also presented with applications to ice shelves and crevasse penetration. Finally, a speculative theory regarding large scale iceberg formation is presented. It is meant mainly as an impetus to further discussion on the topic, with the hope that a model relating crevasse geometries to flow parameters can result in crevasse spacings that could produce the tabular icebergs which are so newsworthy.

The primary focus of this thesis is to move away from the "after the fact" studies that are so common in calving research, and instead devote energy to determining what creates the conditions that drive the calving of ice in the first place.

PREFACE

The ice age is coming... but I have no fear...
–The Clash

The most real things in the world are those
that neither children nor men can see.
–Francis P. Church

Even the fool sometimes has sage insights.
–Chinese fortune cookie

ACKNOWLEDGEMENTS

A project of this type always requires the support of a great many people. It would be difficult to name everyone that has aided me during my time at the University of Maine, but there are several people that I would like to mention.

I would like to thank my parents, sister, and brother for always supporting the decisions I make.

I would like to thank Jesse Johnson for introducing me to glaciology during my first visit to this campus. Jesse and I shared an office for three years, and his friendship and assistance have been greatly appreciated. I would also like to thank Simon Krughoff, who has rescued me from the many computer disasters in which I found myself, usually of my own creation. Simon was also never averse to a trip to the Dome or playing a round of golf in the driving rain.

I would like to acknowledge the members of my committee for their valuable insights and suggestions, and their understanding when progress was slow. Peter Kleban and Don Mountcastle were brave enough to assist in a project with which they had little familiarity and approached it with much enthusiasm. Jim Fastook was always encouraging, and seemed to know something about everything. Roger Hooke provided solid advice at all times and was extraordinarily considerate and thorough in reviewing this thesis.

Finally, I would like to thank Terry Hughes, who has patiently guided me through my time at Maine. The education I received from Terry was not relegated to only glaciology. Terry was more than willing to pass on to me knowledge he has gained from a lifetime of first-hand experience. His willingness to entertain new ideas is invaluable in an advisor, and his gentle prodding allowed me to discover things on my own, without ever straying too far from the herd.

TABLE OF CONTENTS

LIST OF TABLES

LIST OF FIGURES

CHAPTER 1

INTRODUCTION

calve ('kav) *v.* **1:** to give birth to a calf; *also*: to produce offspring
2: *of an ice mass*: to separate or break so that a part becomes detached

1.1 Why Study Calving?

Any discussion regarding the calving of ice must first address the fundamental question, "What is calving?" The second definition given above is the focus of this thesis. Calving, as defined by glaciologists, is the removal of ice from a system by a mechanism that displaces a large quantity of ice. Mass can be removed from a system in any number of ways, and in the case of ice in the natural environment there are also melting and wind ablation mechanisms to consider. In polar regions, where temperatures are usually well below freezing, melting is not usually a concern and removal of ice by natural mechanisms like wind, is small. On the other end of the spectrum is calving, which can remove massive quantities of ice almost instantaneously. Small scale calving events like slab calving from ice cliffs can remove tens of cubic meters while large scale events like the release of iceberg B-15 into the Ross Sea in Antarctica in March 2000 can remove upwards of 6000 km^3 from the system in a single event. The dominant ablation mechanism in Antarctica is calving, while in Greenland, calving represents nearly half the mass loss of the Greenland Ice Sheet.

When calving events of all sizes are considered together over some period of time, their contribution to the mass balance of an ice system is substantial. While melting and wind ablation processes do contribute to the evacuation of ice mass from the system, the thermodynamics of these processes is inefficient. Trying to melt ice when

temperatures rarely rise above freezing in an environmental system requires energy that most polar regions cannot provide. Calving of ice, at least in regions where there are outlets for the newly released ice to migrate toward warmer climates, does not require the thermodynamic energy necessary to actually melt the ice. Instead, the ice can be carried away by currents to locations where the climate is more favorable for this to occur. The work necessary to melt the ice and the supply of energy to do this work no longer needs to be part of the original mass balance system being examined.

In addition to the local effects of calving on the mass balance of ice sheets, there are also considerations in overall global climate. As ice is calved and carried away by global ocean currents, the cold ice then melts at a location far away from the normally cold water associated with polar regions. When this cold water is released outside the polar region and into the global ocean conveyor, the dynamics of this conveyor may change dramatically (Broecker and Denton, 1989; Broecker, 1994; Hulbe et al., In press). Heinrich events (quasi-periodic events where large amounts of ice are released into the oceans) in the North Atlantic have been studied. It has been demonstrated that the Laurentide ice sheet, with an areal extent of nearly all of Canada and the northern United States, could have undergone rapid periods of surging of an ice stream draining the Hudson Bay/Hudson Strait region, releasing massive quantities of fresh water into the ocean currents (MacAyeal, 1993; Alley and MacAyeal, 1994). The global ocean conveyor is dependent on temperature and salinity gradients of the ocean; as a result, when massive quantities of cold, fresh water are carried into these currents and released, the conveyor may shut down. The ocean is thought to be the biggest influence on atmospheric dynamics and climate, and once the currents in the ocean are disturbed, the global climate can be drastically affected.

The climate is also affected by simply the presence of large terrestrial ice sheets, like the Greenland and Antarctic ice sheets, as well as the Laurentide ice sheet. Abrupt climate change can be caused by the feedback between the climate/ice sheet

system, possibly causing rapid retreat of the ice sheet. In the case of the Laurentide ice sheet, which retreated approximately 10,000–15,000 years ago, the retreat was relatively quick; it occurred in only a few thousand years. Simulations have also been done on this climate/ice sheet feedback mechanism, showing there is a point where the ice sheet grows to such an extent as to cause noticeable change to the jet stream flowing over North America (research results currently located at <http://www-bprc.mps.ohio-state.edu/PolarMet/paleonwp.html>). Similar results are obtained by Calov et al. (2002), also using a coupled climate/ice sheet model which is able to produce short (approximately several hundred years) surging events between long (7,000 yrs) periods of inactivity in the ice sheet. In situations of this type, calving of ice as a result of climate forcing would aid in physically reducing the size of the ice sheet, possibly allowing the climate to revert back to its original state or draining the ice sheet entirely.

Of more practical interest, at least on a more immediate, human scale, is the danger posed by calved ice as it floats out to the sea. Even slab calving and small scale tabular iceberg formation events can be dangerous (Epprecht (1987), pers. comm. Hughes). Icebergs released from the Greenland ice sheet are numerous in the North Atlantic shipping lanes, posing many dangers. These types of icebergs have inflicted damage in the past, with the Titanic perhaps the most famous example, and they continue to be of concern to shipping interests. The International Ice Patrol <http://www.uscg.mil/lantarea/iip/home.html> uses the United States Coast Guard to observe and map iceberg locations and motions during those times when iceberg release is at its highest, typically between the months of February and July. The icebergs themselves are not the only danger; as the cold water of the Labrador Current merges with the warmer waters of the Gulf Stream, dense fog is formed, creating a possibly lethal mixture of ice, fog, and the severe storms that are so common in the North Atlantic. There is even some evidence to suggest that

the number of icebergs in the North Atlantic is increasing rapidly, which may be a bellwether of an overall climatic condition. In the Antarctic, as well as in commercial shipping ports in Arctic regions, icebergs can clog harbors, necessitating the use of means other than ships to deliver supplies. Outside of Antarctica this may not be an issue, as airports are never too far from iced-in locations, but for crews working in Antarctica, the nearest airport is thousands of miles away and unpredictable weather is the norm. Icebergs that close off supply routes to Antarctic research stations have the potential to be very dangerous to the people who live there, perhaps necessitating a type of "Berlin air-lift" scenario, where supplies would need to be flown in to the isolated parties. All this leads one to believe that there are important reasons to study calving and to attempt to quantify how and when calving events occur, for both scientific and humanitarian reasons.

1.2 Previous Work

Modern glaciology is a young discipline, with the work of John F. Nye setting the groundwork only 50 years ago. The study of calving is still in its infancy, even in the context of glaciology. Much of the work on calving and attempts to quantify the process have dealt with observation of active calving fronts on glaciers that calve into lakes, called lacustrine calving, and active calving fronts that extend into arms of the sea, called tidewater calving. Work of this type was always done from afar, due to the inherent danger associated with fractured ice fronts. The ice in these areas is very unstable, with deep crevasses and constant movement. The main focus of the work was to get a measure of the ice velocity U_i and compare that to the position of the ice front L, which could be advancing, retreating, or stationary. An ice front velocity $U_f = \mathrm{d}L/\mathrm{d}t$ was then deduced and these two velocities were subtracted to get a calving rate $U_c = U_i - U_f$. This result was purely empirical, with no real attempt at explaining why the ice was calving at the rate observed. In recent years,

with the advent of high resolution satellite imagery, the same approach was taken on larger scales, with observations made over entire fronts of ice shelves in Antarctica and Greenland. As large icebergs were released, the new front position was noted as well as the velocity of the ice shelf to determine the calving rate. Again, the why of the process was not examined.

There has been theoretical work done through the years, perhaps starting with the work of Reeh (1968), who made an attempt to explain fracture initiation in floating ice due to the bending moment and resulting arching near the ice front. There was later work contributed by Iken (1977), who examined the stress fields of a large overhanging ice mass as it calved into the water below. Lingle et al. (1981) studied calving linked to tidal flexure along grounding lines of Jakobshavn Isbræ, West Greenland. Recent work has attempted to determine, through numerical modeling, whether a relation exists between calving speed and water depth (Hanson and Hooke, 2000), as observation has suggested (Brown et al., 1982; Pelto and Warren, 1991). This hypothesis has been questioned by van der Veen (1996, 2002).

1.3 Why This Study?

Calving has previously been relegated to the sidelines in glaciology, or as Terry Hughes might put it, "outside the big-top, relegated to the midway biting the heads off chickens with the freaks." Much good work has been done in the observation of calving fronts (for example Warren and Aniya (1999); Warren (1999) and references therein) but as stated earlier, the front of a calving glacier is inherently dangerous, so most of this work is done from afar. This results in a lack of firm knowledge of the physical processes that are actually taking place in the ice that lead to crevassing (see Warren et al., 2001 with correction in Kenneally, In press) and thus to calving events, large or small. This study aims to quantify these physical processes by examining the material properties of ice and attempting to determine how the ice fails, thus becoming cracked

and crevassed in the first place. Again, there is little field data to fall back on, since the where and when of crevasse formation is difficult to ascertain. By detailing the processes that can initiate and propagate crack formation and growth, it is hoped that a new definition of calving can be brought forth. This definition will move away from the previously stated definition of $U_c = U_i - U_f$, which is purely observational, to a definition that takes into consideration where cracks form, how fast they grow in the ice, and where they are liable to initiate a calving event. With this knowledge a calving rate can be defined in terms of physical, or intrinsic, properties of the ice and mechanical, or external, properties of the earth-ice system. A model of this type could lead to prediction based on how these parameters change rather than attempting to extrapolate observed data to current conditions.

1.4 Organization

This study is organized in several parts. The first section deals with ice as an elastic (brittle) material. An assumption of this type is reasonable in polar regions where ice is exposed to bitter cold air temperatures. This assumption allows the use of linear elastic fracture mechanics and dislocation based fracture mechanics to determine geometrical properties of cracks that form in the ice, such as penetration depths, opening displacements and speed of crack propagation.

The second part concerns the use of a crack propagation law for materials undergoing creep deformation. Ice was shown to be experience creep by Glen (1955) and it is this idea of creep deformation that governs the modeling of ice to this day. A model of crack propagation involving both elastic and ductile material properties is derived and the values describing the crack geometry are found using fracture mechanics. These are then used as initial conditions in the growth model. This model can be used to determine the rate at which a crack can penetrate through a given thickness

of ice. When used in conjunction with the flow velocity of the ice, predictions can be made as to where crevasses will penetrate entirely through some thickness in the ice.

The third part of the thesis returns to fracture mechanics and its application in finding a quantitative description of the back stresses that are present in floating ice. The back stress is posited to exist almost anyplace that a detriment to forward ice flow exists. It results from side shear for ice flowing through confined fjords, local grounding points, and drag from slower tributaries entering the main trunk of ice flow. The back stress cannot be measured directly, so it must be inferred from measurements taken in the field. When the fracture mechanics machinery that is developed is combined with observed crevassing phenomena, a derived mathematical model can be used to predict the value of the back stress. This eliminates the need for actual field measurements, as crevasses can be measured by remote sensing techniques, and allows for a check on any field measurements that have been made. This technique will be applied to the floating portion of Byrd Glacier, which flows from the East Antarctic Ice Sheet, through the Transantarctic Mountains, into the Ross Ice Shelf in western Antarctica.

Finally, the last part of new work presented attempts to explain how geometric properties of crevasses can be used to predict crevasse spacing and thus the size of icebergs that are ultimately released from a floating ice shelf. This is applied to the Ross Ice Shelf where various strain rate, back stress, and ice hardness parameter measurements are known. An argument is made as to how the variation in strain rates along a single flow band can control tabular iceberg formation or the smaller, more common iceberg releases.

The conclusion of the thesis takes the term "warts and all" (see Johnson, 2002, pg. 175) to heart and makes an accounting of the validity as well as the shortcomings of the work. Any attempt to completely describe crevassing and calving thoroughly will have to answer for its underlying assumptions so that future research can understand

where possible shortcuts, and maybe even mistakes, were made. Recommendations on the direction future work should take are made, and the reasons for their not being included here are also presented.

1.5 What to Take Away

The primary focus of this thesis in its infancy was a description of calving from a "first principles" standpoint. It was hoped that some kind of law could be derived that would take the how and predict the when and where of calving events. This goal soon proved elusive. The processes that lead to calving of ice are so many and so relatively poorly understood, or not understood at all, that it would be almost impossible to create such a law that would adequately describe calving for the numerous environments where it takes place. There are many paths that can be followed to pursue what is possible. The path chosen here is to try to keep all solutions analytical, or at least as computationally unintensive as possible, without sacrificing too much in the way of accuracy. Assumptions are made that also contribute to this keep-it-analytical philosophy. While complex modeling of calving events can be done, such as with the finite element method, this was not the road chosen in this work.

Ultimately, what should be taken away from this work is the idea that there are processes in ice that contribute to crevassing and calving, and that these processes can be described in relatively simple terms, and still give viable and relevant results. Building on these first order solutions will undoubtedly be a long process, with enough work to keep many researchers involved for many years.

CHAPTER 2

FRACTURE OF ELASTIC MATERIALS

2.1 Linear Elastic Fracture Mechanics: Background

Fracture mechanics began in earnest as a field of study with the work of A.A. Griffith in the early 20th century (Griffith, 1921). At the time, Griffith was studying the brittle fracture of glass fibers in an attempt to quantify what was observed during fracture, as well as to rectify some inconsistencies that arose with current theories. Prior to this time, the prevailing theory predicted that as flaws arose in materials, stresses would concentrate around the tips of these flaws and ultimately become infinite. This theory then predicted that flawed materials could not withstand any load without failure. These early theories dealt with yielding criteria, but Griffith set forth to create a theory that did not contain this apparent paradox.

The study of linear elastic fracture mechanics unites two aspects that control fracture in a material: the stress analysis of the loads acting on a structure and the material properties of the structure itself. With these considerations, brittle fracture will occur when (Kanninen and Popelar, 1985)

$$K(a, \sigma, D) = K_c(T, \dot{\sigma}, B)$$

where K will be shown later to be a controlling parameter of fracture, dependent on crack length a, applied stress σ and specimen dimension D. The material property K_c depends on temperature T, rate of loading $\dot{\sigma}$ and dimensions of the cracked section B. Individually, the two values K and K_c are of no use and must be considered in conjunction with each other.

How a flaw develops initially is of minimal concern here. It is simply assumed that a flaw can appear in one of three ways: as an inherent defect in the material, as a defect introduced during the fabrication of the material, or as damage incurred during the life of the material. With the last assumption being the most appropriate for ice in its natural environment, a careful study of how flaws evolve into large scale cracks that can produce icebergs can be undertaken. The question of how the flaws are initially created can be swept aside since it is already known that they do in fact exist. The scale of these flaws will be examined later in this thesis.

Griffith expanded upon Inglis' previous work in elasticity (Inglis, 1913) to determine the factors that control brittle fracture in solids. The initial step was the study of the stress field around an elliptical flaw contained within a solid, subjected to far-field stresses that acted perpendicular to the major axis of the ellipse. The Inglis solution to this problem relates the yield stress σ_Y of the material to geometric properties of the elliptical flaw

$$\frac{\sigma_Y}{\sigma} = 1 + 2\sqrt{\frac{a}{\rho}} \tag{2.1}$$

where $2a$ is the length of the ellipse's major axis and ρ is the minimum radius of curvature. The second term on the right in Eq. 2.1 is a *stress multiplier*. It increases with flaw size (major axis length $2a$ increasing) and it decreases with increasing tip radius ρ. For a typical theoretical calculation, one can choose parameters to get an idea of the magnitude of the stress multiplier. Let ρ be the interatomic spacing, approximately 0.1 nm, and the flaw size $a = 1\,\mu$m. The stress multiplier is then found to be $\sigma_Y/\sigma = 200$. In the case of glass, a theoretical strength of $\approx 13,700$ MPa has been determined, while the typical strength is only about 70–140 MPa. These differ by roughly a factor of 200, the number found in the simple calculation for the stress multiplier. The ultimate, and probably obvious, conclusion to all this is that cracks reduce material strength by concentrating stress around the crack tips.

There are two basic approaches in attacking this problem: the energy approach and the stress intensity approach. Griffith began with the energy approach. His basic assumption was that cracks would grow when it was energetically favorable to do so; namely, the potential energy of the system would decrease. The total energy Π of the system is defined to be

$$\Pi = U_P + U_E + W = U_M + W \tag{2.2}$$

where

U_P – potential energy of load system

U_E – elastic energy stored in the material

W – energy required to form new crack surfaces.

Consider an infinitesimal crack extension in a material of unit width. If the crack grows some incremental length $\mathrm{d}a$, the mechanical energy U_M will decrease due to material relaxation, and the surface energy W will increase due to the increase in surface area of the crack faces. Mathematically this can be written as

$$\frac{\mathrm{d}U_M}{\mathrm{d}a} < 0, \qquad \frac{\mathrm{d}W}{\mathrm{d}a} > 0 \tag{2.3a}$$

where the critical situation arises when the two are equal, or

$$\frac{\mathrm{d}\Pi}{\mathrm{d}a} = 0 \tag{2.3b}$$

From this, Griffith then defined the condition for crack opening as

$$\frac{\mathrm{d}\Pi}{\mathrm{d}a} < 0 \tag{2.3c}$$

Explicitly determining the form of Eq. 2.2 is straightforward for the simple geometry of a crack of length $2a$ within a solid body. The elastic energy U_E is given as

$$U_E = \frac{\pi a^2 \sigma^2}{E} \tag{2.4}$$

where E is the elastic modulus of the material. There are two methods employed to physically study fracture: load control, where the applied load remains fixed, and

displacement control, where induced displacements are held constant. For a system under load control, the potential energy U_P is

$$U_P = -2U_E \tag{2.5}$$

If γ is defined as the surface energy per unit area, then the energy required to form new crack surfaces W is

$$W = 4a\gamma \tag{2.6}$$

Together these give the total energy of the system Π from Eq. 2.2 as

$$\Pi = -\frac{\pi a^2 \sigma^2}{E} + 4a\gamma \tag{2.7}$$

Using Eq. 2.3 the critical length of a crack a_c can be determined:

$$\frac{\mathrm{d}\Pi}{\mathrm{d}a} = 0 \quad \rightarrow \quad a_c = \frac{2\gamma E}{\pi \sigma^2} \tag{2.8}$$

There are limitations in this form of the energy approach, however. The equation is only valid for specific geometries and the assumption that all energy is dissipated through new crack surface creation is not necessarily the case for real materials. A second, equivalent approach dealing directly with the stresses around the crack tip is more valuable for practical applications and will be covered next. However, the energy-balance approach will be revisited when treating rates of crack growth in §2.5.

2.2 The Stress Intensity Approach

Of more practical use in the treatment of fracture is the so-called *stress intensity approach.* Rather than concerning oneself with the energies that contribute to crack growth, it is appropriate to look at the stresses located near the crack tip. A re-derivation of the pertinent equations is unnecessary in this treatment since the mathematical analysis is very involved and beyond the scope of this thesis. The derivations are easily referenced and the final forms of the equations are well known, so they will

simply be stated. The stress field at the tip of a crack in an infinite solid being acted upon by a far field tensile stress σ is (for more detailed analysis see Kanninen and Popelar (1985); Broek (1978, 1988); Lawn (1993))

$$\sigma_1 = \frac{K_I}{\sqrt{2\pi r}} \cos\frac{\theta}{2}\left(1 + \sin\frac{\theta}{2}\sin\frac{3\theta}{2}\right) \tag{2.9a}$$

$$\sigma_2 = \frac{K_I}{\sqrt{2\pi r}} \cos\frac{\theta}{2}\left(1 - \sin\frac{\theta}{2}\sin\frac{3\theta}{2}\right) \tag{2.9b}$$

$$\sigma_{12} = \frac{K_I}{\sqrt{2\pi r}} \sin\frac{\theta}{2}\cos\frac{\theta}{2}\cos\frac{3\theta}{2} \tag{2.9c}$$

in a polar coordinate system with the origin located at the crack tip and the positive z-axis along the plane of crack growth. Figure 2.1 illustrates this geometry. In these

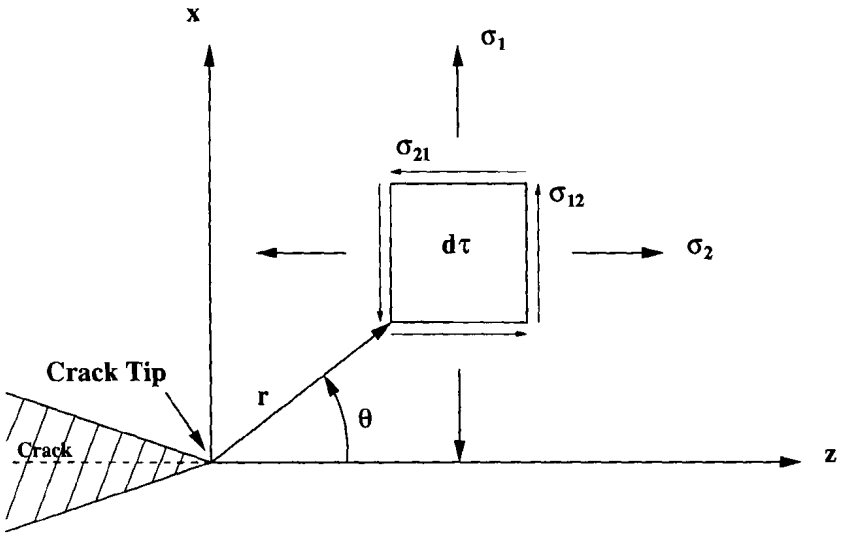

Figure 2.1: Stress fields acting on an infinitesimal element $d\tau$ a distance r and angle θ from the tip of a crack. Note the directions of the coordinate axes.

equations a new variable K_I has been introduced. This is called the *stress intensity factor*, or SIF. The SIF is an alternative method of characterizing cracking. The subscript I denotes that this is the stress field for a mode I crack problem. There are three distinct modes of cracking (Fig. 2.2): mode I, called tensile opening, mode II, which is in-plane shearing, or sliding, and mode III, which is out-of-plane shearing,

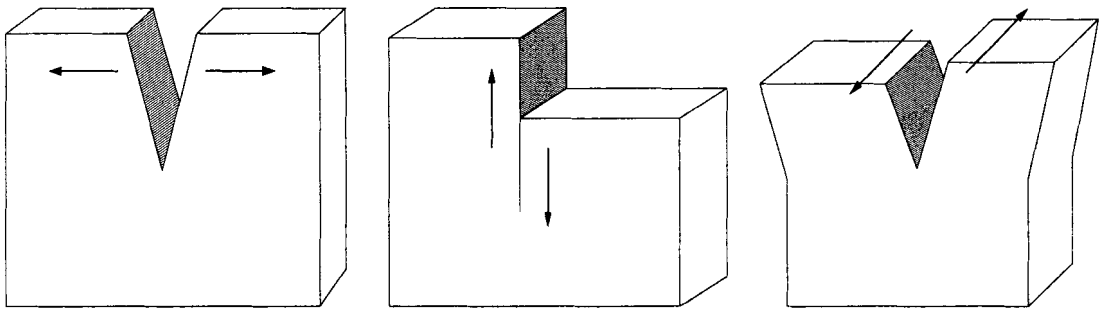

(a) Mode I (b) Mode II (c) Mode III

Figure 2.2: The three distinct modes of crack growth for use with the stress intensity approach.

or tearing. Each mode has its characteristic stress field and SIF. For the purposes of this study, only mode I cracking will be considered.

Since the stress field is thus readily known, the problem now becomes one of determining the SIF for the problem being studied. On dimensional grounds it can be shown that the general form for the mode I SIF is

$$K_I = \beta\sigma\sqrt{a} \tag{2.10}$$

In this relation, σ is the far field tensile stress, $2a$ is the length of the crack (fracture mechanics convention dictates this choice) and β is a multiplicative factor that is dependent on the geometry of the specimen. The simplest example to study is a crack of length $2a$ completely contained in a specimen subjected to a tensile stress (see §2.3.1), where β has been determined to be $\sqrt{\pi}$, so the SIF is given by

$$K_I = \sigma\sqrt{\pi a}$$

The condition for fracture to occur is that K_I must exceed some critical value K_{Ic}, which is a material property called the fracture toughness. Generally, the difficulty lies in determining the proper value for the constant β.

2.3 Stress Intensity Factors For Various Geometries

As with most aspects of fracture mechanics, how one arrives at the final result (as long as it is done with a sound approach) is of less importance than what the final result actually is and how it can be applied to the problem at hand. In other words, there is no need to re-invent the wheel. This philosophy holds true for the determination of stress intensity factors for various geometries. For the most common systems, as well as many uncommon ones, the work has already been done so one only needs to look up the results in a handbook. The actual derivation of these SIFs is usually very difficult, but comprehensive collections of these SIFs and the techniques used to determine them can be found in numerous sources, such as Sih (1973a,b) Tada et al. (1973) and Rooke and Cartwright (1976). All stress intensity factors presented in the following sections can be found in these references.

2.3.1 Center Crack

This problem has already been mentioned but will be included here for completeness. Consider a crack of length $2a$ wholly contained within a solid of infinite length and width (Fig. 2.3). A far field tensile stress of magnitude σ acts perpendicular to the crack faces, tending to extend the crack. In this case the the mode I SIF is given by

$$K_I = \sigma\sqrt{\pi a} \tag{2.11}$$

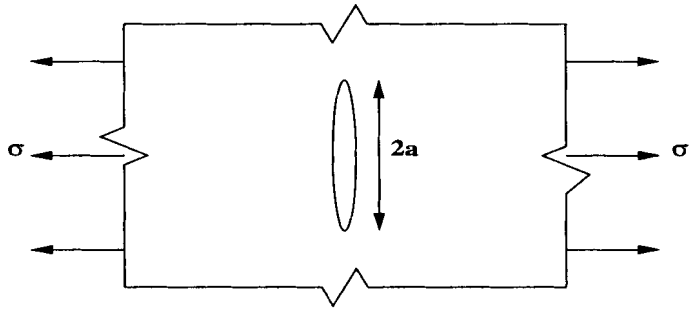

Figure 2.3: Geometry for the SIF of a center crack within a solid.

2.3.2 Single Edge Crack

The geometry for this case is a single crack nucleated at the surface of a sample and extending a distance a into the material (Fig. 2.4). The specimen has a total thickness H and again is subjected to a far field tensile stress of magnitude σ. The mode I SIF is given by

$$K_I = \sigma\sqrt{\pi a}F(a/H) \tag{2.12a}$$

where β now equals $\sqrt{\pi}F(a/H)$ and $F(a/H)$ is a polynomial determined through numerical methods to be

$$F(a/H) = 1.12 - 0.231\left(\frac{a}{H}\right) + 10.55\left(\frac{a}{H}\right)^2 - 21.72\left(\frac{a}{H}\right)^3 + 30.39\left(\frac{a}{H}\right)^4 \tag{2.12b}$$

It should be noted that for $H \gg a$, this polynomial reduces to a constant 1.12, the first order solution for an edge crack and a familiar result in fracture mechanics (Kanninen and Popelar, 1985). Equation (2.12) is of great importance in this study since the large scale surface crevasses that will later be examined are obviously edge cracks.

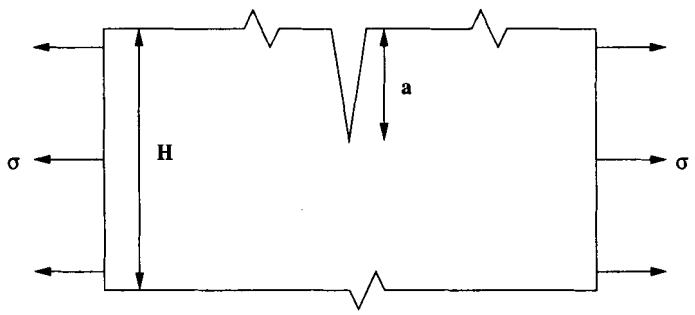

Figure 2.4: Geometry for the SIF of a single edge crack in a solid.

2.3.3 Parallel Edge Cracks in a Half-Plane

This result takes the previous result one step further, considering a series of evenly spaced, equal depth edge cracks in an infinitely long half-plane (Fig. 2.5). The spacing

between cracks is $2b$ and the depth of each crack is again a. A far field tensile stress of magnitude σ acts on the specimen. The mode I SIF for a single crack within the crack field is

$$K_I = \sigma\sqrt{\pi a}\sqrt{b/s}F(b/s) \tag{2.13a}$$

where $s = b + a$ and the polynomial $F(b/s)$ is

$$\begin{aligned} F(b/s) \;=\; & \frac{1}{\sqrt{\pi}}\left[1 + \frac{1}{2}\left(\frac{b}{s}\right) + \frac{3}{8}\left(\frac{b}{s}\right)^2 + \frac{5}{16}\left(\frac{b}{s}\right)^3\right. \\ & \left. + \frac{35}{128}\left(\frac{b}{s}\right)^4 + \frac{63}{256}\left(\frac{b}{s}\right)^5 + \frac{231}{1024}\left(\frac{b}{s}\right)^6\right] + 22.501\left(\frac{b}{s}\right)^7 \\ & - 63.502\left(\frac{b}{s}\right)^8 + 58.045\left(\frac{b}{s}\right)^9 - 17.577\left(\frac{b}{s}\right)^{10} \end{aligned} \tag{2.13b}$$

The behavior of this function is shown in Figure 2.6.

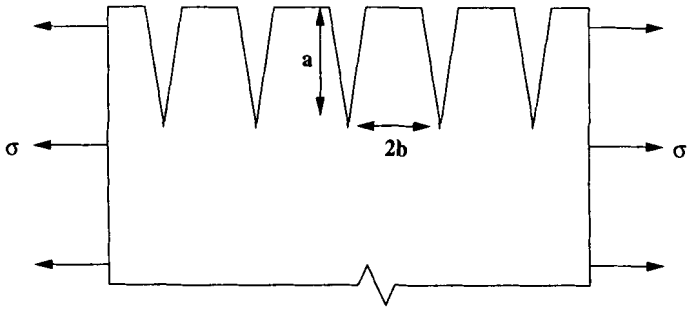

Figure 2.5: Geometry for the SIF of a single edge crack within a field of evenly spaced, equal depth edge cracks in a solid.

2.3.4 Single Edge Crack Subject to a Varying Load

Up to this point, only constant loads acting at infinity have been considered. Here, a spatially varying load on the crack face is considered. First, the case of a linearly increasing tensile load on an edge crack of depth a is examined. The load increases from 0 at the surface to a maximum of $2\sigma_{\text{ave}}$ at the crack tip. The mode I SIF is given by

$$K_I = 1.366\sigma_{\text{ave}}\sqrt{\pi a} \tag{2.14}$$

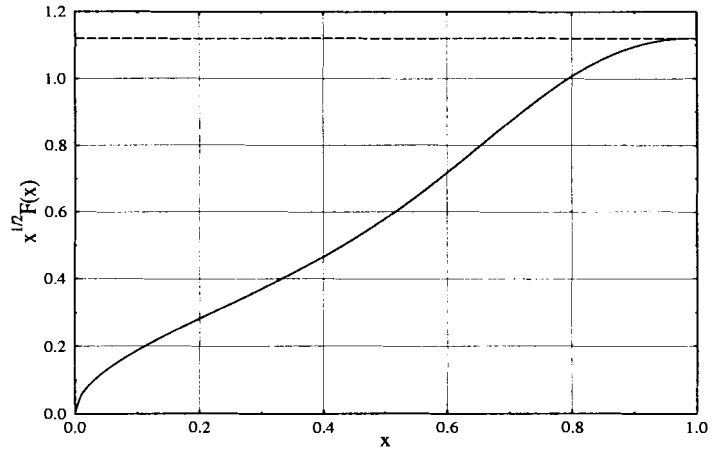

Figure 2.6: Factor $\sqrt{(b/s)}F(b/s)$ (Eq. 2.13b) for the case of a field of evenly spaced crevasses. For spacing $2b$ much greater than crevasse depth a ($s \to b$), the function approaches the first order solution for a single crack in an infinite solid, equal to 1.12, represented by the dashed line.

Of more practical interest is a second case where the load increases in some way other than linearly (Fig. 2.7). Consider a system with a sample of thickness H, a single edge crack of depth a, and a force P acting at a depth $z < a$. The differential force, $\mathrm{d}P$, is $\sigma(z)\,\mathrm{d}z$, which allows a differential form of the SIF to be written as

$$\mathrm{d}K_I = \frac{2\sigma(z)\,\mathrm{d}z}{\sqrt{\pi a}} F\left(\frac{z}{a}, \frac{a}{H}\right) \tag{2.15a}$$

with the function $F(z/a, a/H)$ given by

$$\begin{aligned} F\left(\frac{z}{a}, \frac{a}{H}\right) \;=\; & \frac{3.52\,(1 - z/a)}{(1 - a/H)^{3/2}} - \frac{4.35 - 5.28 z/a}{(1 - a/H)^{3/2}} \\ & \left(\frac{1.30 - 0.30\,(z/a)^{3/2}}{\sqrt{1 - (z/a)^2}} + 0.83 - 1.76\frac{z}{a}\right)\left(1 - \frac{a}{H}\left(1 - \frac{z}{a}\right)\right) \end{aligned} \tag{2.15b}$$

This result can now be integrated numerically to determine the SIF for any arbitrary load acting on the faces of a crack. This will be especially useful when considering the SIF due to ice overburden pressure, since the density of ice is not necessarily constant

throughout the thickness of the ice due to effects of firn (loosely packed surface snow), water, etc. which in turn causes a stress that increases in a non-linear fashion.

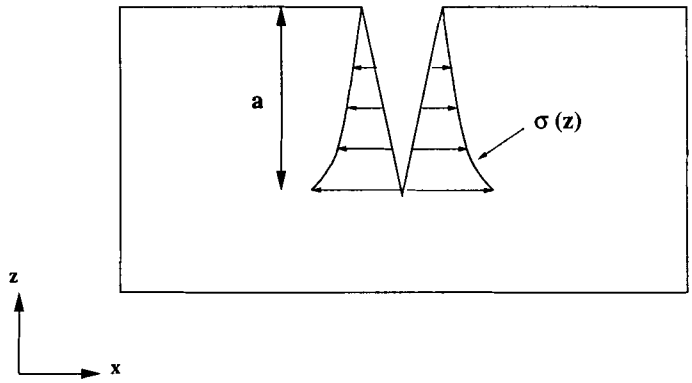

Figure 2.7: Geometry for the SIF of a single edge crack subjected to a load that increases non-linearly with depth.

2.4 Practical Applications of Fracture Mechanics

Since most of the work of deriving the various stress intensity factors for the most common geometries has been done, the task of putting these results to work becomes more tractable. To start, the depths to which surface crevasses will penetrate in floating ice can be determined and this can be compared to work already done in this regard (Weertman, 1973; van der Veen, 1998b). Floating ice is chosen since this eliminates any basal shear stresses. It is also assumed that side shear stresses are located far from the crevasse position, where their effects will be minimal. The inclusion of shear stresses would result in a mixed-mode cracking analysis, which is a far more difficult problem. Mixed-mode cracking will be addressed in §6.4.1. A less rigorous but equally important examination of closely spaced crevasses (Smith, 1976; Nemat-Nasser et al., 1979) will also be presented and compared to the results of similar work done by Weertman (1977).

2.4.1 Single Crack in an Ice Field

In practical terms, the crevasses in an ice field are edge cracks so the results given by Eqs. (2.12) and (2.13) would seem appropriate starting points. To simplify matters, only single cracks in an "infinite" glacier will be considered. The term infinite will be taken to mean an infinitely long structure, with a tensile stress acting at the termini. The stresses acting on a crack in a typical glacier would be a pulling stress as well as the overburden pressure of the ice as the crack penetrates more deeply. For this reason the SIFs given by Eqs. (2.14) and (2.15) must be considered. It would be nice to keep things as simple as possible and use Eq. 2.14, but this is not a realistic condition for ice fields. The density of ice is not constant and has been given as a polynomial relation with depth (Rist et al., 1996). An empirical relation has also been given by Paterson (1994) as

$$\rho(z) = \rho_i - (\rho_i - \rho_s)\, e^{-Cz} \tag{2.16}$$

with the constant C determined by observation at various locations. The densities ρ_i and ρ_s represent the density of ice and of surface snow respectively. The next difficulty to address is which SIF should be used to describe the overall problem. For a single crack, should the SIF for the far field tensile stress as described by Eq. 2.12 be used, the SIF that is determined by Eq. 2.15, or some combination of the two? Fortunately the answer is quite simple since stress intensity factors obey the principal of superposition (Kanninen and Popelar, 1985). Any number of SIFs applicable to a system, provided they are all describing equivalent modes of cracking, can simply be added together to get a net SIF that completely describes the system. In this case the result would be

$$\begin{aligned} K_{\text{total}} &= \sum_i K_i \\ &= K_{\text{tensile}} + K_{\text{overburden}} \end{aligned} \tag{2.17}$$

It is important to note here that while the total SIF must be greater than zero to have a physical meaning when discussing fracture, individual components of the sum described by Eq. 2.17 can be negative. In this case, the SIF given by K_{tensile} will always be greater than zero, since the tensile stress is acting to pull the crack faces apart, but the SIF given by $K_{\text{overburden}}$ will be negative due to compressive ice overburden stress, and as the crack penetrates deeper into the ice, where this stress dominates, the growth of the crack will be halted. This behavior is illustrated in Figure 2.8. It is this very fact that allows for a calculation of the depth to which a crack will advance.

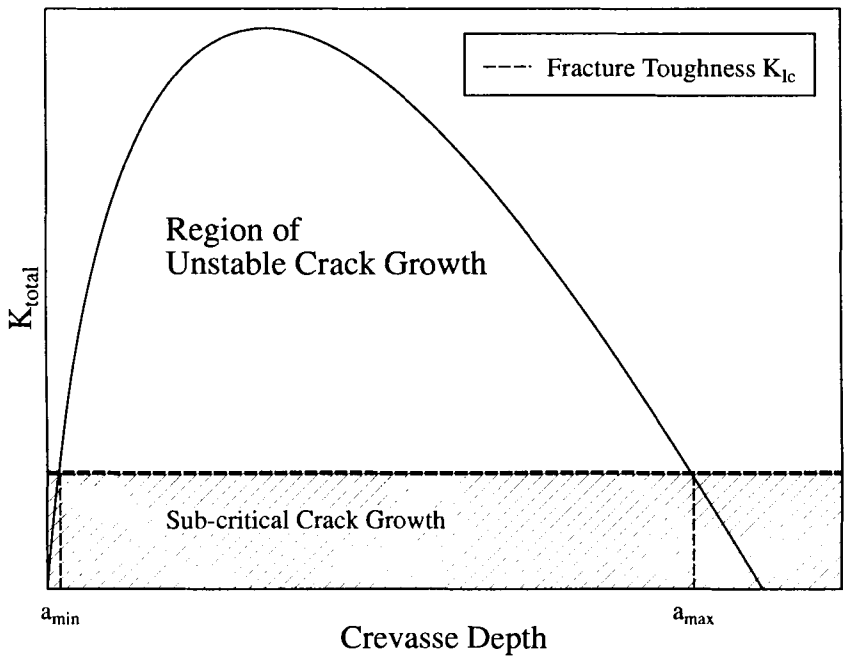

Figure 2.8: General behavior of the stress intensity function for a material subjected to constant tensile stress and increasing compressive stress with depth. Regions above the fracture toughness, denoted by the horizontal dashed line, correspond to unstable fracture regimes, while those below are stable. Cracks of a minimum, or critical, depth a_{min} will penetrate entirely through the unstable region, ceasing propagation when the maximum crevasse depth a_{max} is achieved.

The second point of intersection that is found when solving

$$K_{\text{total}} = K_{Ic} \tag{2.18}$$

will be the maximum depth $a_{\max}$. When the left hand side of Eq. 2.18 becomes less than K_{Ic}, the fracture criteria stated in §2.2 is no longer met and the crack will cease its propagation. Fracture mechanics allows one to quantify this intuitive idea.

The matter of actually solving Eq. 2.18 is straightforward once a functional relation for Eq. 2.15 has been found. The relation is determined by the stresses acting on the crack faces. The stress that arises due to ice overburden can be found using

$$\begin{aligned} \sigma_i(z) &= -\int_0^z \rho(z')g\,\mathrm{d}z' \\ &= -\rho_i g z + \frac{\rho_i - \rho_s}{C} g\left(1 - e^{-Cz}\right) \end{aligned} \tag{2.19}$$

where the density relation given by Eq. 2.16 has been used. Substituting this result into Eq. 2.15 and integrating gives the final form for $K_{\text{overburden}}$. The SIF arising from the tensile stress is much more straightforward, requiring only Eq. 2.12 and an appropriate value for the tensile pulling stress σ.

Ultimately, the solution obtained is a function of crack depth a, ice thickness H and fracture toughness of ice, K_{Ic}. Rist et al. (1996) determine a range of fracture toughness values from 0.1 MPa·m$^{1/2}$ to 0.4 MPa·m$^{1/2}$, and later work (Rist et al., 1999) amends those results to a smaller range of 0.05 MPa·m$^{1/2}$ to 0.15 MPa·m$^{1/2}$. Maximum crack depths will be examined for these recent end-member values as well as for the average value of 0.1 MPa·m$^{1/2}$. The typical pulling stress in glaciers is on the order of 1 bar (0.1 MPa) and other constant values used in the calculation are $\rho_i = 917\,\text{kg/m}^3$, $\rho_s = 350\,\text{kg/m}^3$, $g = 9.8\,\text{m/s}^2$ and $C = 0.02\,\text{m}^{-1}$ (Paterson, 1994). Crack depths calculated with these parameter values are summarized in Table 2.1 and complete results are shown in Figure 2.9.

The values chosen for ice thickness in this analysis are primarily for comparative purposes, as floating ice generally does not get as thick as 3000 m, yet these limited

K_{Ic} (MPa·m$^{1/2}$)	H (m)	a (m)
0.05	1000	33.26
	2000	33.34
	3000	33.39
0.1	1000	31.95
	2000	32.03
	3000	32.09
0.15	1000	30.58
	2000	30.66
	3000	30.70

Table 2.1: Summary of results for maximum crack depths. Complete results are plotted in Figure 2.9.

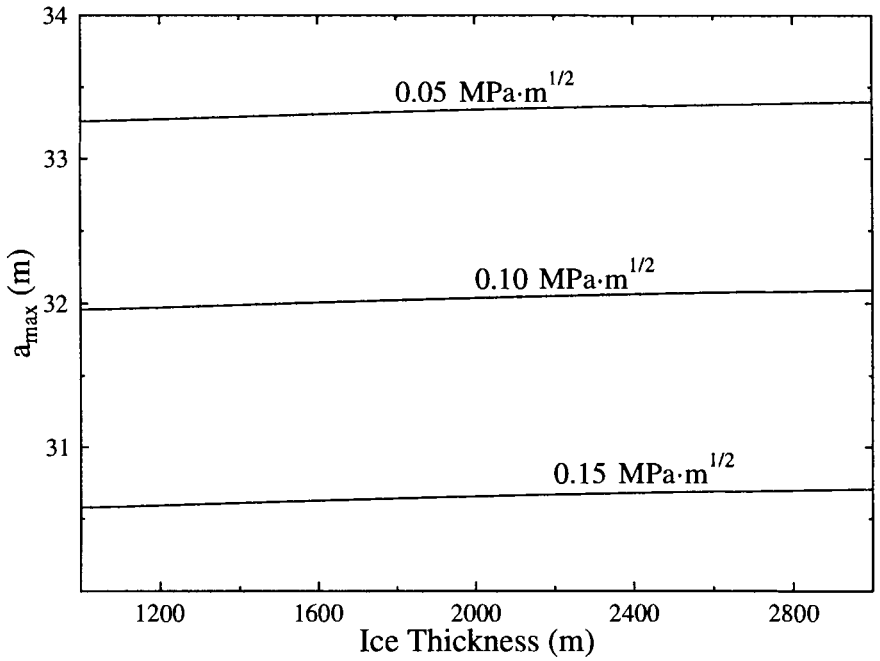

Figure 2.9: Maximum crack depths for various ice thicknesses H and end-member and average values of fracture toughness K_{Ic}.

results seem to imply that the overall thickness of the ice does not seem to make a significant difference in the maximum depth to which a crevasse will penetrate for a specific fracture toughness in the framework of this formulation. Analysis of representative "real-world" ice thicknesses will be done later in Chapter 4, and this work will demonstrate that the thickness *is* important when a more accurate expression is derived for the longitudinal pulling stress in floating ice. (Also, there seems to be limitations in using this approach for ice that is much less than 1000 m thick. This is addressed in §2.6.2.) For the calculation done here, as the total thickness of the ice increases by a factor of three, the change in maximum crevasse depth is less than 1%. It is the differences that arise when comparing the fracture toughness and its effect on crevasse depth for a given ice thickness which are significant. The maximum crevasse depth decreases by almost 10% for the extreme values of K_{Ic}. However, getting an accurate measurement of the fracture toughness is difficult, given the nature of glacial ice. At the surface in most locations there is a layer of metamorphosed snow, called firn, of varying thickness. Below the firn is denser ice, but the density can vary significantly due to fluctuations in temperature, pressure, and bubble content. Since this is a fracture mechanics analysis in an elastic material, while ice is visco-plastic, the results are idealized, but they can still be considered appropriate. As a crevasse opens, the faces are exposed to the often frigid air that is common in glacial environments. This cold air cools the exposed ice, creating a more brittle material, which allows for the assumption that, at least locally, the ice around a crevasse can behave in a nearly elastic manner.

2.4.2 Water Filled Crevasses

The situation described in the previous section dealt with a crevasse that simply opened up due to the tensile pulling stress acting on the glacier and remained air-filled. In reality, there will be blowing and/or precipitating snow as well as possible

seasonal melting, depending on the location in question. In the latter case meltwater could fill these crevasses, creating a situation where the ice overburden pressure is no longer sufficient to prevent further penetration of the crevasse since the density of the water is greater than the density of the ice. These crevasses could possibly propagate all the way to the base of the glacier. More extensive treatment of this topic has been covered in papers, including Weertman (1973) and van der Veen (1998b), as well as more recent results describing the catastrophic breakup of shelf ice due to water filled crevasses (Scambos et al., 2000). Perhaps the most obvious example of a water filled crevasse is a basal crevasse in a floating ice shelf. Seawater that fills the crevasse will add to the tensile stress acting on the crevasse walls, allowing for greater penetration depths and the possibility that the crevasse will propagate to regions close to the surface of the glacier, resulting in a large point of weakness in the ice.

The treatment for water filled crevasses is the same as earlier, except that a stress due to the water pooling in the crevasse is also included. If the crevasse is filled with water to a depth d_w below the ice surface, there will be an induced outward stress on the crevasse walls given by

$$\sigma_w = \rho_w g \left(z - d_w\right), \quad z > d_w \tag{2.20}$$

similar to Eq. 2.19. This relation would then be substituted into Eq. 2.15 yielding

$$K = \frac{2\rho_w g}{\sqrt{\pi a}} \int_{d_w}^{a} \left(z - d_w\right) F\left(\frac{z}{a}, \frac{a}{H}\right) \mathrm{d}z \tag{2.21}$$

The analog to Eq. 2.18 would be

$$K_{\text{total}} = K_{\text{tensile}} + K_{\text{ice overburden}} + K_{\text{water overburden}} = K_{Ic} \tag{2.22}$$

Given the proper initial conditions for water depth, it can be shown that the left hand side of Eq. 2.22 will always be greater than the fracture toughness of ice, indicating that the crevasse can indeed penetrate all the way through the thickness of the glacier (Weertman, 1973; van der Veen, 1998b).

2.4.3 A Field of Evenly Spaced Crevasses

A reality of studying crevasses in a glacial environment is that they rarely appear alone. Crevasse fields form as crevasses are nucleated in certain areas and carried forward with the ice flow. This makes it more appropriate to study how crevasses behave when contained in a crevasse field of this sort. The analysis is less rigorous but it is an aspect of crevassing that it is necessary to examine.

Recall the equation describing the SIF for a field of evenly spaced, equal depth crevasses given by Eq. 2.13:

$$K_I = \sigma\sqrt{\pi a}\sqrt{b/s}F(b/s) \tag{2.23a}$$

where $s = b + a$ and the polynomial $F(b/s)$ is

$$\begin{aligned} F(b/s) \;=\; & \frac{1}{\sqrt{\pi}}\left[1 + \frac{1}{2}\left(\frac{b}{s}\right) + \frac{3}{8}\left(\frac{b}{s}\right)^2 + \frac{5}{16}\left(\frac{b}{s}\right)^3\right. \\ & \left. + \frac{35}{128}\left(\frac{b}{s}\right)^4 + \frac{63}{256}\left(\frac{b}{s}\right)^5 + \frac{231}{1024}\left(\frac{b}{s}\right)^6\right] + 22.501\left(\frac{b}{s}\right)^7 \\ & - 63.502\left(\frac{b}{s}\right)^8 + 58.045\left(\frac{b}{s}\right)^9 - 17.577\left(\frac{b}{s}\right)^{10} \end{aligned} \tag{2.23b}$$

Also, recall the equation governing the SIF for a single edge crack

$$K_I = \sigma\sqrt{\pi a}F(a/H) \tag{2.24a}$$

where $F(a/H)$ is

$$F(a/H) = 1.12 - 0.231\left(\frac{a}{H}\right) + 10.55\left(\frac{a}{H}\right)^2 - 21.72\left(\frac{a}{H}\right)^3 + 30.39\left(\frac{a}{H}\right)^4 \tag{2.24b}$$

Because Eq. 2.23a is derived for a sample of infinite thickness, there is no procedure to determine the depth to which a crevasse will penetrate similar to that of §2.4.1. It would be nice to have a formula for the SIF of a crevasse within a crevasse field that explicitly included the thickness of the ice. Note that from Figure 2.13b

$$\lim_{b \gg a} \sqrt{\frac{b}{s}} F\left(\frac{b}{s}\right) \rightarrow 1.12$$

which simply means as the spacing becomes very large, the SIF given by Eq. 2.23a approaches that for a single edge crack in an infinitely long specimen. As an ad-hoc hypothesis, $\sqrt{b/s}F\,(b/s)$ is substituted for the first term on the right hand side of Eq. 2.24b. In the limit of large spacing relative to crevasse depth, it is known that this form of the stress intensity factor will converge to the proper result so it may be worthwhile to examine the results for the smaller spacings where the effects of other crevasses are important.

The same method was employed as in the previous sections to determine the maximum depth of crevasse penetration, with the only case studied being for air-filled crevasses. A number of different solutions were found for a variety of ice thicknesses, crevasse spacings w (=$2b$), and the two end-members of fracture toughness. These results were all calculated for a tensile pulling stress of 1 bar (0.1 MPa) and are summarized in Table 2.2.

H (m)	K_{Ic} (MPa·m$^{1/2}$)	w (m)	$a_{\max}$ (m)
1000	0.05	100	29.35
	0.05	1000	32.21
	0.15	100	26.89
	0.15	1000	30.53
3000	0.05	100	29.45
	0.05	1000	33.35
	0.15	100	26.98
	0.15	1000	30.66

Table 2.2: Maximum crevasse depths for various ice thicknesses H and crevasse spacings $w = 2b$. Depths are calculated for the end-member values of fracture toughness.

These results are intriguing because they display the same behavior contained in the solutions for the single edge crack:

- As the fracture toughness increases, the maximum depth to which a crevasse will penetrate decreases.

- As the thickness of the ice increases the maximum crevasse depth increases.
- Crevasses that are more closely spaced have shallower maximum penetration depths.

Maximum crevasse depths for a range of spacings are shown in Figure 2.10. This picture shows that when crevasses are separated by less than 300 m, there is a large influence on the depth to which a crevasse can penetrate. Above $w = 300$ m the spacing of the crevasses has some noticeable effect on the depth, but as w approaches 500 m, this effect becomes very small, and depths approach the values discussed earlier for a single crevasse.

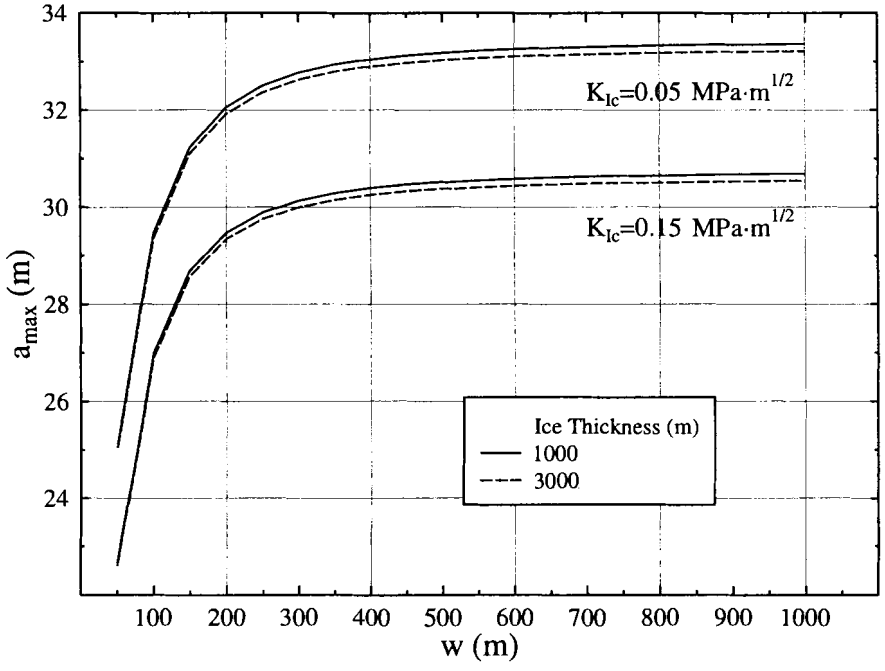

Figure 2.10: Maximum crevasse depth as a function of inter-crevasse spacing w for ice thickness H equal to 1000 m and 3000 m and the end-members of fracture toughness.

Calculations made by Smith (1976) also demonstrate that crevasses in a crevasse field should not penetrate as deeply as a single crevasse. This is also consistent with

later work done by Weertman (1977), who proved that there is a minimum spacing for crevasse growth in a crevasse field. Any spacing less than this minimum, which is given as

$$w_{min} = \frac{3}{2}\left(\frac{K_c}{\sigma}\right)^2 \tag{2.25}$$

will not allow crevasse propagation. In this case, a calculation of this minimum spacing gives values ranging from 0.38 m (for $K_c = 0.05\,\mathrm{MPa{\cdot}m^{1/2}}$) to 3.38 m (for $K_c = 0.15\,\mathrm{MPa{\cdot}m^{1/2}}$). The calculations presented here are well above these minima.

The stress intensity factor for a range of crevasse spacings can be seen in Figure 2.11. Both panels show how the SIF changes for a variety of crevasse spacings w. The stress intensity factors for the simple model presented here suggest that crack growth will not occur if the spacing w is less than 2.25 m for $K_{Ic} = 0.15\,\mathrm{MPa{\cdot}m^{1/2}}$ or w less than 0.25 m for $K_{Ic} = 0.05\,\mathrm{MPa{\cdot}m^{1/2}}$. This is shown in Figure 2.11(a). Figure 2.11(b) shows the SIF for spacings calculated using the Weertman criteria of Eq. 2.25. Since the SIF functions here penetrate into the region of unstable crack growth, the Weertman criteria is an overestimate for this model.

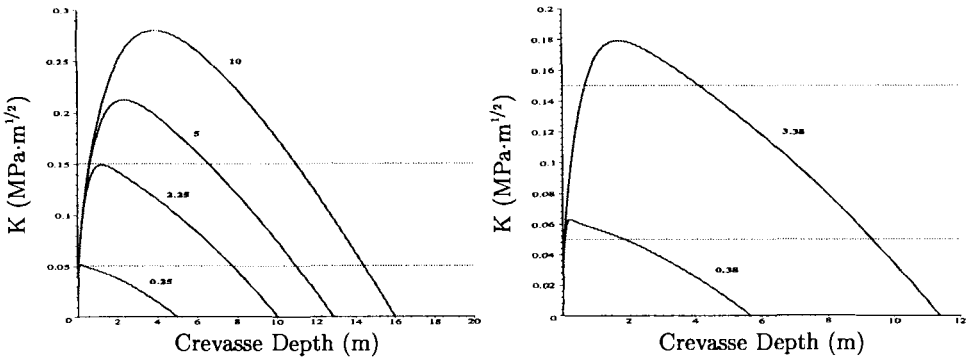

(a) **(b)**

Figure 2.11: Stress intensity factors for a range of crevasse spacings w. The dashed lines represent the range of fracture toughness. The calculated stress intensity factors using the minimum crevasse spacings derived from the Weertman model (Eq. 2.25 and **(b)** above) are an over-estimate in the present formulation.

The model presented here is less than rigorously derived, but it describes crevasse growth in a manner consistent with the more rigorous solutions given by Eqs. (2.12) and (2.15). In this way it can be a valuable tool for describing the qualitative behavior of crevasses in a crevasse field, as well as possibly providing quantitative results.

2.5 The Rate of Crack Growth

The previous sections have dealt with the geometry of cracks in ice but have not addressed the time scale associated with the formation of these cracks. In order to determine calving rates, a reasonable quantification of the rate at which these deep ice crevasses penetrate would be a great benefit. Work has been done in the past using linear elastic fracture mechanics to try and obtain reasonable results that fully describe the rate of crack growth in terms of material properties and system variables. These results will be discussed here, as well their appropriateness to the overall problem at hand.

2.5.1 The Mott Formulation

Perhaps the first attempt at modeling crack growth rates was that by Mott (1948). Mott expanded upon the work of Griffith to include a kinetic energy term in the description of crack formation. On dimensional grounds, Mott was able to assume that the kinetic energy in a cracked body could be written as

$$KE = \frac{1}{2} k \rho V^2 \left(\frac{a\sigma}{E}\right)^2 \tag{2.26}$$

where k is a numerical constant left to be determined and V is the velocity of the crack through the material. This term is then added to the potential energy expression of Griffith and, providing no external work is done, conservation of energy requires that

$$\frac{1}{2} k \rho a^2 V^2 \left(\frac{\sigma}{E}\right)^2 - \frac{\pi \sigma^2 a^2}{E} + 4\gamma a = \text{constant} \tag{2.27}$$

Mott assumed that since the total energy must be constant, its derivative with respect to crack length will be zero. From this assumption, he set $dV/da = 0$ and solved for the velocity to obtain

$$V = \sqrt{\left(\frac{2\pi}{k}\right)\left(\frac{E}{\rho}\right)\left(1 - \frac{a_o}{a}\right)} \tag{2.28}$$

where $a_o = (2/\pi)(E\gamma/\sigma^2)$, the critical crack length in the Griffith theory, is taken as the initial crack length. The limiting speed of crack growth predicted by Eq. 2.28 is

$$V_l = \sqrt{\left(\frac{2\pi}{k}\right)\left(\frac{E}{\rho}\right)} \tag{2.29}$$

which, depending on the values of k, is near the speed of sound in a solid body, $C_o = (E/\rho)^{1/2}$. It is important to note that the kinetic energy term as written in Eq. 2.26 was a result of an assumption made by Mott that the crack velocity was much less than the speed of sound in the body. Clearly, the final result invalidates this initial assumption.

2.5.2 The Dulaney and Brace Formulation

The shortcomings in the formulation of Mott were later examined by both Berry (1960) and Dulaney and Brace (1960). The approach of Dulaney and Brace also considers a kinetic energy term that must be added to the potential energy of the system as in Eq. 2.27. An initial condition that $V = 0$ when $a = a_o$ is imposed and the surface energy γ is re-written to get

$$-\frac{1}{2}k\rho a^2 V^2 \left(\frac{\sigma}{E}\right)^2 - \frac{\pi\sigma a^2}{E} + \frac{2\pi\sigma^2 a a_o}{E} = \frac{\pi\sigma^2 a_o^2}{E} \tag{2.30}$$

Solving this equation for the velocity gives

$$V = \sqrt{\left(\frac{2\pi}{k}\right)\left(\frac{E}{\rho}\right)}\left(1 - \frac{a}{a_o}\right) \tag{2.31}$$

There is no assumption regarding the derivative of velocity with respect to crack length as in Mott's approach, which was considered questionable when it was first

done. By this time, the value of k had also been examined (Roberts and Wells, 1954) giving a lower bound on $\sqrt{(2\pi/k)}$ equal to 0.38 for a Poisson's ratio $\nu = 0.25$. Using this result, Eq. 2.31 can be written as

$$V = 0.38C_o\left(1 - \frac{a}{a_o}\right) \tag{2.32}$$

with C_o defined as before.

2.5.3 Discussion

The crack propagation velocities given by Eqs. (2.29) and (2.32) both give results indicating that a crack will form in a solid in very little time. Anyone who has ever walked on a frozen pond in winter, heard a sudden "pop," and looked down to see a newly formed fracture in the ice knows that these results seem very reasonable. Cracks in ice will seem as if they just appear rather than steadily creep along through the ice with a distinct start and stop point in time. It would then seem that these results are not of too much use in a practical application of crack growth in glacial ice. While the high rate at which the cracks form is impressive, it does not seem to be of much use to describe calving. Later in this thesis, a crack propagation model will be derived based on elastic-ductile deformation that itself works on a more "glacial" time scale. In combination with creep deformation pulling the crevasse faces apart, this law will yield a more realistic law for crevasse growth. To finish this discussion on the rate at which cracks form, consider this account from Swithinbank (1999, pg. 96) reporting on the formation of a new crevasse:

> "As I was hammering in a tent peg, there was an alarming splitting sound that lasted seconds, rose in a crescendo, and ended with a crack like a rifle shot. I leapt away thinking that I had broken the snow bridge over a crevasse. I must have initiated a crack which then propagated because the surface was under tension. Next morning I found a 2-millimetre wide crack extending 35 metres from the tent peg that had given me a moment of terror."

2.6 Limitations

2.6.1 The Plastic Zone

There are limitations to the use of fracture mechanics in describing actual processes. The name alone implies that the material must behave in an elastic manner. Thus, a consideration must be made of how accurately elastic behavior describes the system. The stress field described by (2.9) displays infinite stress behavior at the crack tip, where r approaches zero, but, in reality, this is not true. Around the crack tip there are various mechanisms that keep the stresses finite. These include the following:

- bridging across the crack faces
- micro-cracking
- plastic deformation at the crack tip.

The last of these is of interest here since there is an analytic solution one can derive to determine the size of the plastic zone, and by extension, how accurate the elastic assumption is.

It is noted from observation that the fracture process zone (FPZ), the area around the crack tip where the mechanisms noted above are at work, is roughly a constant size independent of the specimen geometry (Kanninen and Popelar (1985), pers. comm. Eric Landis, University of Maine). It is also noted that larger structures are more brittle and toughening mechanisms have progressively less effect. From these observations, it is assumed that if one can show the zone of plastic deformation to be small relative to the size of the structure, then one can apply fracture mechanics with a high degree of confidence.

A determination of the size of the plastic zone must begin with some sort of yield criteria being defined. The von Mises yield criteria states that for a specimen under uniaxial tension, yielding will occur when the yield stress σ_Y is surpassed by some

combination of the principal stresses, or mathematically

$$\sigma_Y = \frac{1}{\sqrt{2}}\left[(\sigma_1 - \sigma_2)^2 + (\sigma_2 - \sigma_3)^2 + (\sigma_1 - \sigma_3)^2\right]^{1/2} \tag{2.33}$$

The σ_i are the principal stresses of the system, which can be determined through the use of a Mohrs circle (Parry, 1995) from the stress states given by Eq. 2.9. There are two cases to consider when determining the principal stresses: plane stress and plane strain. Since the systems under consideration here are very thick, any out-of-plane deformation will be assumed small compared to the overall thickness and taken as zero. The principal stresses are (with $\sigma_3 = \nu(\sigma_1 + \sigma_2)$ for plane strain and ν the Poisson ratio):

$$\sigma_1 = \frac{K_I}{\sqrt{2\pi r}} \cos\frac{\theta}{2}\left(1 + \sin\frac{\theta}{2}\right) \tag{2.34a}$$

$$\sigma_2 = \frac{K_I}{\sqrt{2\pi r}} \cos\frac{\theta}{2}\left(1 - \sin\frac{\theta}{2}\right) \tag{2.34b}$$

$$\sigma_3 = 2\nu\frac{K_I}{\sqrt{2\pi r}} \cos\frac{\theta}{2} \tag{2.34c}$$

These results can then be substituted into Eq. 2.33 and the extent of the plastic zone can be determined by solving for r. The final result gives an estimate on the extent of the plastic zone as

$$r_p = \frac{1}{4\pi}\left(\frac{K_I}{\sigma_Y}\right)^2 \left[\frac{3}{2}\sin^2\theta + (1 - 2\nu)^2(1 + \cos\theta)\right] \tag{2.35}$$

with the coordinate system origin at the crack tip.

Equation 2.35 contains the stress intensity factor for the system being studied. Because of this, it is difficult to make an *a priori* estimate of the plastic zone because of the dependence the SIF will have on factors like specimen thickness and crack length. It was therefore tacitly assumed that the plastic zone was small. The results that were found can now be used to validate that assumption.

A plot of Eq. 2.35 is shown in Figure 2.12 with a yield stress $\sigma_Y = 1$ bar, for ice of thickness $H = 3000$ m and crack depth $a = 32$ m, which is typical of the crack depths

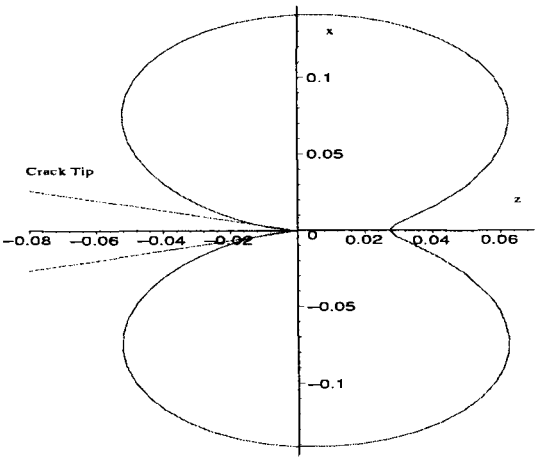

Figure 2.12: Polar plot of the plastic zone r_p, measured in meters, for plane strain conditions. The crack extends from the negative y direction to the origin, with its tip located at the origin.

shown in Table 2.1. The stress intensity factor is taken as the sum of Eqs. (2.12) and (2.15). This picture shows that the assumption that the plastic zone is small, relative to the overall dimensions of the system, is justified under a von Mises yield criteria.

Differentiating Eq. 2.35 with respect to θ gives the angle which maximizes the radial value defining the plastic zone, in this case

$$\theta_{max} \approx 1.512\,\text{rad}$$

When this value is combined with the maximum value of the stress intensity factor K_I, found by differentiating and solving for the crevasse depth (see the convex profile of the stress intensity function in Figure 2.8) the maximum extent of the plastic zone can be ascertained. The results are displayed in Table 2.3. These maximum values also reinforce the assertion that the plastic zone is small in relation to the system's size.

H (m)	$a_{\{K=K_{\max}\}}$ (m)	$r_{p,\max}$ (m)	ratio
1000	12.63	3.156	0.003
1500	12.65	3.162	0.002
2000	12.66	3.165	0.001
2500	12.67	3.168	0.001
3000	12.68	3.170	0.001

Table 2.3: Maximum extent of the plastic zone for various ice thicknesses H. The column "ratio" is defined as $r_{p,\max}/H$.

2.6.2 Numerical Limitations

The limitations discussed in the previous section dealt with real aspects of the process of fracture in a solid. There are also some limitations that arise as a result of numerical approximations in the solution to the equations shown earlier.

Figure 2.13 shows maximum crevasse penetrations as a function of ice thickness for a constant tensile pulling stress of $\sigma = 1$ bar (0.1 MPa). When the results for maximum crevasse depth were first presented in §2.4, it was stated that the unrealistic value of

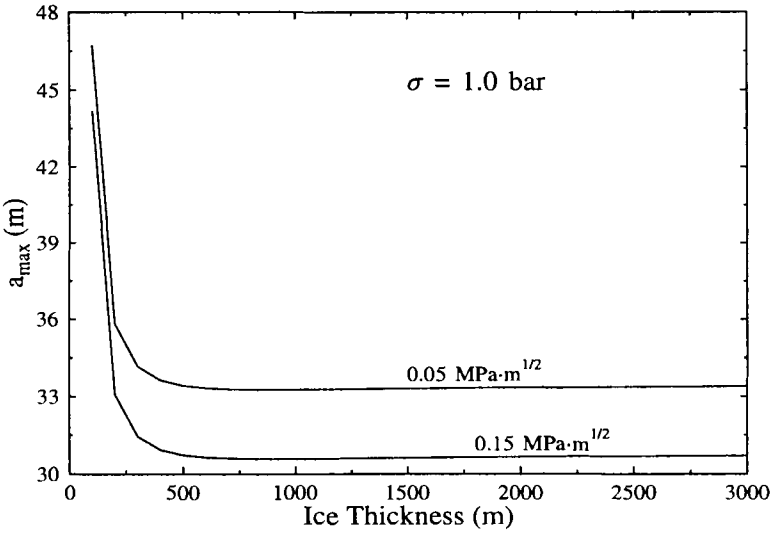

Figure 2.13: Maximum crevasse depths for $100 \leq H \leq 3000$ m and tensile pulling stress $\sigma = 1$ bar.

3000 m was chosen for the ice thickness for comparison with the more common value of 1000 m. This allowed a discussion on the general behavior of the stress intensity function over a large range of ice thicknesses, and it was seen that this range showed little effect on the values of $a_{\max}$. Figure 2.13 contains results at the other end of the spectrum, where the ice thickness is more realistic: $H < 1000$ m. However, the results seem counter-intuitive. As the ice thickness *decreases*, the maximum crevasse depth *increases*. The results are even more dramatic when the tensile stress is increased by a factor of 2.5, to 2.5 bar (0.25 MPa), shown in Figure 2.14. The maximum crevasse depth occurs at a thickness of about 200 m, independent of the value of the fracture toughness, and is nearly 50% of the entire thickness. In both Figures 2.13 and 2.14 the depth stabilizes for $H > 1000$ m.

The exact reason for the behavior in these figures is unclear, but no physical assumptions have been made that might plausibly lead to such a result. It is most likely a consequence of numerical approximations that are made when integrating

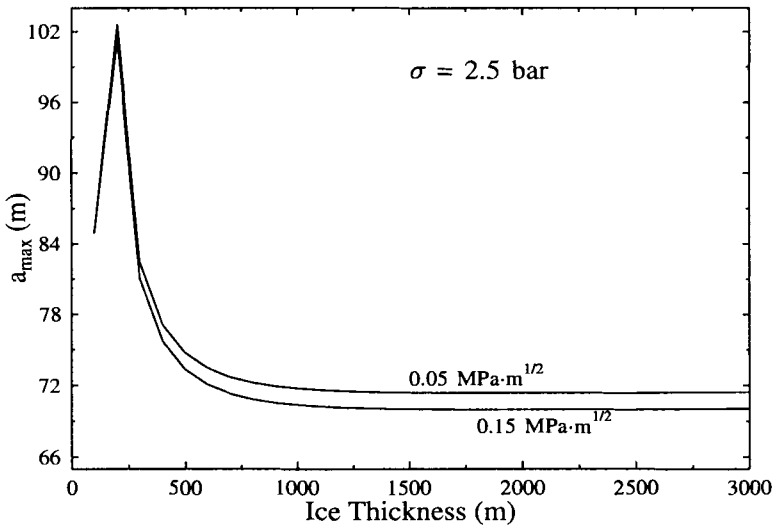

Figure 2.14: Maximum crevasse depths for $100 \leq H \leq 3000$ m and tensile pulling stress $\sigma = 2.5$ bar.

the complicated form of the stress intensity factor that arises when using Eq. 2.15 and then solving $K_{\text{total}} = K_{Ic}$. The previous work done by van der Veen (1998b) examined penetrations for ice that was only 250 m thick using this formulation, but the conclusions drawn here seem to invalidate using this approach for ice that is less than 1000 m thick.

2.7 An Alternate Approach: Dislocation Theory

An alternate yet equivalent formulation of the problem of crack formation in a solid is dislocation theory. The problem is now analyzed by considering a build-up of dislocations in a system. Where fracture mechanics considers that the stresses at a crack tip become infinite, dislocation theory treats the infinite stress build-up as a collection of discrete dislocations at the crack tip and along the crack surface. Using this formulation allows calculation of the overall geometry of a crack. When used in conjunction with linear elastic fracture mechanics, where the depths of crevasses in ice were determined, a more complete picture of crevasse formation is obtained. The final results will show that newly formed crevasses in ice are actually quite benign, and only after deformation of the ice due to creep processes do dangerous crevasse fields appear.

2.8 Dislocation Density

In order to start a discussion of dislocation theory, it is necessary to discuss what exactly is meant by a dislocation. A dislocation can be defined mathematically by the *Burgers vector* $\mathbf{b}$, which is a discrete dislocation contained within the solid, as illustrated in Figure 2.15. The dislocation within the solid can take on a number of different forms. For the Griffith-Inglis crack discussed earlier, there are both edge and screw dislocations. In this treatment, where cracks are opening transverse to the applied stress, the edge dislocation is the only one considered. When a large number

Equations (2.38) and (2.39) are Hilbert transforms of one another. An explicit form for the dislocation distribution is given by (Muskhelishvili, 1953)

$$B(x_i) = -\frac{2\alpha_j\sqrt{c^2 - x_i^2}}{\pi G}\int_{-c}^{c}\frac{\sigma(x_i')\,\mathrm{d}x_i'}{(x_i - x_i')\sqrt{c^2 - x_i'^2}} \tag{2.40}$$

where the distribution is defined to exist between the points $-c < x_i < c$ and is zero at all other points. The stress in regions where $|x_i| > c$ is given as

$$\sigma(x_i) = \frac{\sqrt{x_i^2 - c^2}}{\pi}\frac{x_i}{|x_i|}\int_{-c}^{c}\frac{\sigma(x_i')\,\mathrm{d}x_i'}{(x_i - x_i')\sqrt{c^2 - x_i'^2}} \tag{2.41}$$

With these expressions, the dislocation density and stress are known everywhere along the crack plane. The term c must satisfy the following relations (Weertman, 1996, pg. 107):

$$\int_{-c}^{c}\frac{\sigma(x_i)\,\mathrm{d}x_i}{\sqrt{c^2 - x_i^2}} = 0 \tag{2.42a}$$

$$\int_{-c}^{c}\frac{x_i\sigma(x_i)\,\mathrm{d}x_i}{\sqrt{c^2 - x_i^2}} = \frac{G\mathbf{b}_T}{2\alpha_j} \tag{2.42b}$$

$$\int_{-c}^{c}\frac{|x_i|\sigma(x_i)\,\mathrm{d}x}{\sqrt{c^2 - x_i^2}} = \frac{G(\mathbf{b}_R - \mathbf{b}_L)}{2\alpha_j} \tag{2.42c}$$

In these relations, $\mathbf{b}_T = \mathbf{b}_R + \mathbf{b}_L$ is the net Burgers vector of all dislocations, $\mathbf{b}_R$ is the net Burgers vector in the region $0 < x_i < \infty$ and $\mathbf{b}_L$ is the net Burgers vector in the region $-\infty < x_i < 0$.

2.9 Stress and Dislocation Density Solutions

Explicit forms for the solutions to Eqs. (2.40) and (2.41) are given by Weertman for the case of an infinite stress at the crack tip. Using his convention, the following relations for a "mean stress" are defined for notational convenience (in the limit $c \to a$, the crack length)

$$\bar{\sigma}_A = -\frac{1}{\pi}\int_{-a}^{a}\frac{\sigma(x_i)\,\mathrm{d}x_i}{\sqrt{a^2 - x_i^2}} \tag{2.43a}$$

$$\bar{\sigma}_B = -\frac{1}{\pi a}\int_{-a}^{a}\frac{x_i\sigma(x_i)\,\mathrm{d}x_i}{\sqrt{a^2 - x_i^2}} \tag{2.43b}$$

With these definitions, Eqs. (2.40) and (2.41) can be written as

$$B(x_i) = -\frac{2\alpha_j\sqrt{a^2-x_i^2}}{\pi G}\int_{-a}^{a}\frac{\sigma(x_i')\,\mathrm{d}x_i'}{(x_i-x_i')\sqrt{a^2-x_i'^2}} + \frac{2\alpha_j}{G}\left[\bar{\sigma}_A\frac{x_i}{\sqrt{a^2-x_i^2}} + \left(\bar{\sigma}_B + \frac{G\mathbf{b}_T}{2\alpha_j\pi a}\right)\frac{a}{\sqrt{a^2-x_i^2}}\right] \tag{2.44}$$

and

$$\sigma(x_i) = \frac{\sqrt{x_i^2-a^2}}{\pi}\frac{x_i}{|x_i|}\int_{-a}^{a}\frac{\sigma(x_i')\,\mathrm{d}x_i'}{(x_i-x_i')\sqrt{a^2-x_i^2}} + \frac{x_i}{|x_i|}\left[\bar{\sigma}_A\frac{x_i}{\sqrt{x_i^2-a^2}} - \bar{\sigma}_A + \left(\bar{\sigma}_B + \frac{G\mathbf{b}_T}{2\alpha_j\pi a}\right)\frac{a}{\sqrt{x_i^2-a^2}}\right] \tag{2.45}$$

2.10 Applications

Using these definitions for stress and dislocation density, it is relatively simple to obtain crack profiles. These crack profiles will then give a quantitative value to the maximum opening displacement of a crevasse, which will be at the surface of the material, as well as a functional relationship for the variation of width with depth. Using the relation given by Eq. 2.36, the displacement can be solved for as a function of depth into the material up to a maximum dictated by the overall depth of the crevasse. All that remains is to determine the functional forms for the equations in 2.43 and plug these into Eq. 2.44 so that the integral in Eq. 2.36 can be evaluated.

2.10.1 The Weertman Constant Density Model

The goal is to apply the relations stated earlier to a typical glacier and determine the physical characteristics of a crevasse. In order to utilize the previous equations, which were derived for a crack of length $2a$ within a solid, for the case of an edge crevasse of depth L in a glacier, a little trickery is required. As illustrated in Figure 2.16, Weertman defines an "image" crack of height L located exactly above a real crack penetrating a depth L into the ice (see Weertman, 1996, pg. 373). The real and

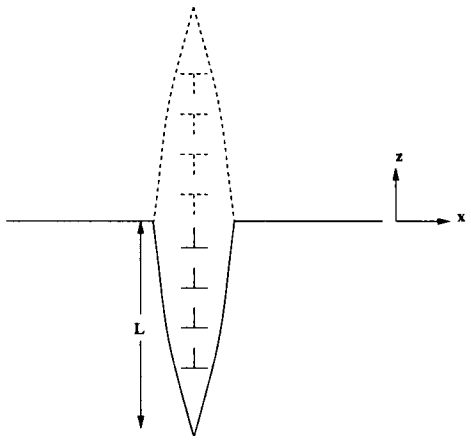

Figure 2.16: Illustration of an image crevasse, defined by the dashed lines, situated directly above a real crevasse of depth L. The image crevasse also contains image dislocations, which are equal in number and opposite in orientation to the real dislocations, $\perp$.

imaginary crevasse are then subjected to an applied stress

$$\sigma_{\text{app}}(z) = \sigma - \rho_i g|z| \tag{2.46}$$

where σ is the tensile pulling stress in the glacier and $\rho_i g|z|$ represents the ice overburden pressure (here taken as linearly increasing with depth, which will be amended later to take into account variations of the ice density with depth). The absolute value is necessary to insure proper symmetry. This applied stress is inserted into Eq. 2.44 (with a change of variables so the negative z-axis is in the direction of crack growth) yielding

$$\begin{aligned} B_x(z) &= -\frac{2\alpha}{G}\frac{\bar{\sigma}_A z}{\sqrt{L^2-z^2}} - \frac{2\alpha}{G}\frac{\bar{\sigma}_B L}{\sqrt{L^2-z^2}} - \frac{\mathbf{b}_T L}{\pi\sqrt{L^2-z^2}} \\ &\quad + \frac{2\alpha\sqrt{L^2-z^2}}{\pi G}\int_{-L}^{L}\frac{\sigma(z')\,\mathrm{d}z'}{(z-z')\sqrt{L^2-z'^2}} \end{aligned} \tag{2.47}$$

In this expression, $\sigma(z') = -\sigma_{\text{app}}(z')$, the net Burgers vector $\mathbf{b}_T = 0$ (the image crevasse cancels all contributions from the real crevasse), $\alpha_j = \alpha_e = 1 - \nu$ for edge dislocations

illustrated in Figure 2.15 (where ν is Poisson's ratio) and $\bar{\sigma}_A$ and $\bar{\sigma}_B$ are

$$\bar{\sigma}_A = -\frac{1}{\pi}\int_{-L}^{L}\frac{\sigma(z)\,\mathrm{d}z}{\sqrt{L^2-z^2}} \tag{2.48a}$$

$$\bar{\sigma}_B = -\frac{1}{\pi L}\int_{-L}^{L}\frac{z\sigma(z)\,\mathrm{d}z}{\sqrt{L^2-z^2}} \tag{2.48b}$$

2.10.2 Opening Displacements

The dislocation distribution is obtained by inserting Eq. 2.46 into Eq. 2.47 and the displacement of the crevasse is found by then inserting $B_x(z)$ into Eq. 2.36 and integrating. The dislocation distribution as a function of z is found to be

$$B_x(z) = -\frac{2\alpha}{G}\bar{\sigma}_A\frac{z}{\sqrt{L^2-z^2}} - \frac{2\alpha\rho_i g z}{\pi G}\ln\left(\frac{L+\sqrt{L^2-z^2}}{L-\sqrt{L^2-z^2}}\right) \tag{2.49}$$

The displacement is then

$$\begin{aligned} D_x(z) &= \int_z^L B_x(z')\,\mathrm{d}z' \\ &= \frac{2\alpha}{G}\bar{\sigma}_A\sqrt{L^2-z^2} + \frac{2\alpha\rho_i g}{\pi G}L\sqrt{L^2-z^2} \\ &\quad -\frac{2\alpha\rho_i g z^2}{2\pi G}\ln\left(\frac{L+\sqrt{L^2-z^2}}{L-\sqrt{L^2-z^2}}\right) \end{aligned} \tag{2.50}$$

where $\bar{\sigma}_A = \sigma - 2\rho_i g L/\pi$ and $\bar{\sigma}_B = 0$.

In this constant density model, the total depth to which the crevasse penetrates is found by solving for L in the relation given by Eq. 2.48a:

$$L = \frac{\pi\,(\sigma - \bar{\sigma}_A)}{2\rho_i g} \tag{2.51}$$

The typical value for the pulling stress $\sigma = 1\,\mathrm{bar}$ is used and the density of ice is $\rho_i = 917\,\mathrm{kg/m^3}$. A value of 0.3 is taken for Poisson's ratio ν, and the shear modulus G is 3.6 GPa (Simmons and Wang, 1971). The stress intensity factor at the tip of the crevasse is $K_I = \bar{\sigma}_A\sqrt{\pi L}$, (Eq. 2.11), the SIF for the simple case of a crack with length $2L$ contained in a solid. Writing this relation in terms of the critical stress intensity

factor K_c (taken here as $0.1\,\mathrm{MPa{\cdot}m^{1/2}}$) and inserting it into Eq. 2.51 yields a value of $L \approx 15\mathrm{m}$. When this total depth is inserted into Eq. 2.50 it yields a maximum opening width $D_x(0)$ of only 0.33 mm! The displacement as a function of depth is shown in Figure 2.17.

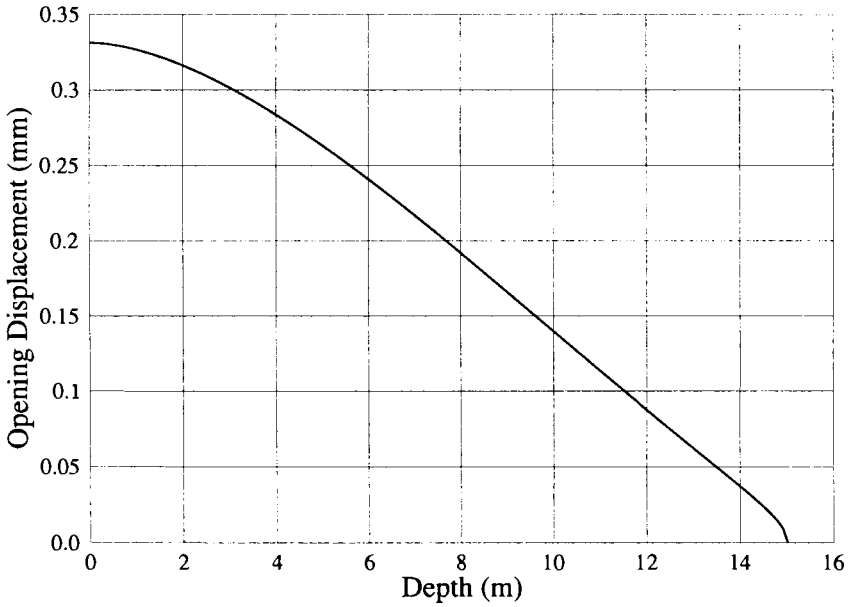

Figure 2.17: The width of a crevasse as a function of depth according to the Weertman constant density model.

2.10.3 Improvements to the Weertman Model

A major simplification of the previous discussion is the use of a constant ice density in the calculation of the stress acting on the crevasse. This is not the case for a real glacier, where the effects of surface snow and firn need to be considered. The formulation given earlier by Eq. 2.16 for the density of snow, firn and ice in terms of an exponential function with depth is

$$\rho(z) = \rho_i - (\rho_i - \rho_s)\, e^{-Cz} \tag{2.52}$$

The value of C is again taken as $0.02\,\mathrm{m}^{-1}$ and $\rho_s = 350\,\mathrm{kg/m^3}$ The applied stress at a depth z will now be (with absolute values still required to preserve symmetry between the real and imaginary crevasse)

$$\sigma(z) = -\sigma_{\mathrm{app}} = -\sigma + \rho_i g|z| - \frac{(\rho_i - \rho_s)\,g}{C}\left(1 - e^{-C|z|}\right) \tag{2.53}$$

This new stress needs to be inserted into the relations given by Eqs. (2.43) and (2.44) which can then be integrated to yield a new displacement function $D_x(z)$.

By inspection it can be seen that Eq. 2.43b will be zero, since the integration is done for an odd function over a symmetric range. The mean stress $\bar{\sigma}_A$ still needs to be calculated. Integration of the first two terms on the right hand side of Eq. 2.53 is trivial, but the third term presents more difficulty. In its current form, the integral

$$I = \int_{-L}^{L} \frac{e^{-C|z'|}\,\mathrm{d}z'}{\sqrt{L^2 - z'^2}}$$

cannot be analytically determined. However, some knowledge exists regarding the behavior of the function, due to earlier work (§2.4.1) and assumptions made about the value for the constant C. It is known that maximum penetration depths of crevasses is on the order of tens of meters. It is also known that the value of C in the calculation is on the order of 0.02. This means the argument of the exponential will be on the order of 0.2, which is small enough that a series expansion of only a few terms is a valid approximation (see Fig. 2.18). The series expansion of the exponential term is

$$e^{-C|z|} = \sum_{n=0}^{\infty}(-1)^n \frac{(C|z|)^n}{n!} \approx 1 - C|z| + \frac{C^2}{2}|z|^2 \tag{2.54}$$

with all terms greater than $O(z^2)$ ignored. The explicit form for the mean stress $\bar{\sigma}_A$ is then

$$\bar{\sigma}_A \approx \sigma - \frac{2\rho_i g L}{\pi} + \frac{(\rho_i - \rho_s)g}{\pi}\left(2L - \frac{\pi C L^2}{4}\right) \tag{2.55}$$

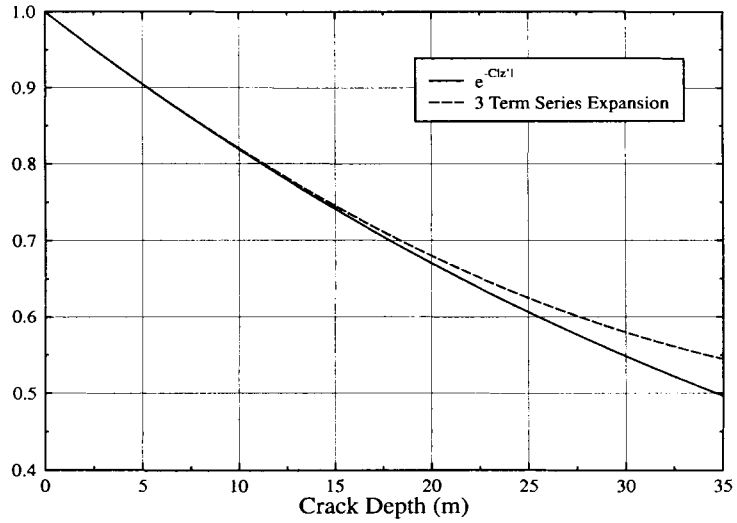

Figure 2.18: Comparison of the function $\exp(-C|z'|)$ to the first three terms of its series expansion. The expansion is valid to within 15% up to crevasse depth $L = z = 35$ m.

The new stress given by Eq. 2.53 is inserted into Eq. 2.44 to yield

$$B_x(z) = -\frac{2\alpha}{G}\bar{\sigma}_A \frac{z}{\sqrt{L^2 - z^2}} - \frac{2\alpha\rho_s g}{\pi G} z \ln\left(\frac{L + \sqrt{L^2 - z^2}}{L - \sqrt{L^2 - z^2}}\right) - \frac{\alpha(\rho_i - \rho_s)gC}{G} z\sqrt{L^2 - z^2} \tag{2.56}$$

It should be noted that the first two terms on the right hand side of Eq. 2.56 are the same as the terms in the distribution for the Weertman constant density model (Eq. 2.49), with the only difference being ρ_i becomes ρ_s in the second term. The last term is a correction to take into account the variation of density with depth. Recall that this is only an approximation (see Eq. 2.54) and higher order terms have been neglected. Finally, to get the lateral width of the crevasse as a function of depth z, Eq. 2.36 is utilized:

$$D_x(z) = \int_z^L B_x(z')\,dz' \tag{2.57}$$

The final form for $D_x(z)$ is

$$D_x(z) = \frac{2\alpha}{G}\bar{\sigma}_A\sqrt{L^2-z^2} + \frac{\alpha(\rho_i-\rho_s)gC}{3G}\sqrt{(L^2-z^2)^3} + \frac{2\alpha\rho_s g}{\pi G}\left[\sqrt{L^2-z^2} - \frac{z^2}{2}\ln\left(\frac{L+\sqrt{L^2-z^2}}{L-\sqrt{L^2-z^2}}\right)\right] \quad (2.58)$$

which will be considered a valid approximation for crevasse depths $L \leq 35\,\mathrm{m}$. The maximum depth L is taken from calculations using linear elastic fracture mechanics.

Figure 2.19 shows how the profile of the crevasse changes with the inclusion of an ice density that is no longer constant. Again, the maximum width of the crevasse $D_{x,\max} = D_x(0)$ is quite small; a crevasse of depth 25 m only opens to 0.38 mm at the surface. (Thus *newly* formed crevasses do not seem all that dangerous.) The behavior of crevasses with total depths of 30 m and 35 m is peculiar. As the crevasse penetration increases, the opening displacement at the surface becomes smaller, with displacements for a crevasse of depth 35 m actually becoming negative. In this case, the two sides of the crevasse wall "interpenetrate" each other (see Weertman, 1996,

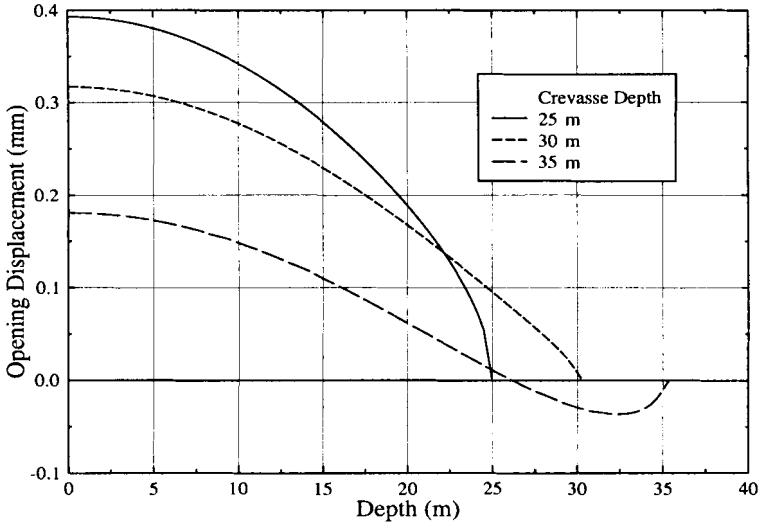

Figure 2.19: Crack profiles using an exponentially changing density with depth for maximum crevasse depths of 25, 30, and 35 m. Maximum crevasse openings are on the order of only 0.3 mm.

pg. 377). There is no physical explanation of this process, but mathematically, as the crevasse depth increases, Eq. 2.55 becomes smaller until it actually becomes negative. This will act to lessen the magnitude of the displacement given by Eq. 2.58, eventually causing a negative displacement in some cases. This may be an indication of the viability of the model as it is currently formulated. The relationship between the maximum crevasse opening at the surface and the depth of the crevasse is shown in Figure 2.20.

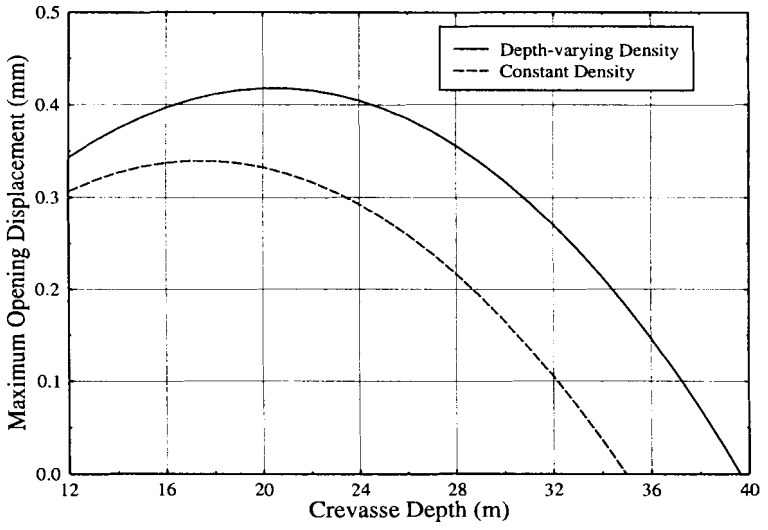

Figure 2.20: Comparison of the two solutions describing maximum crevasse displacement with depth.

In §2.5.3 a first person account on the formation of a crevasse was cited. The width of the crevasse that was measured by Swithinbank, soon after he caused its formation, was on the order of 2 mm. The model derived in this section using dislocation theory may have shortcomings, but it seems to be validated by this field evidence.

2.11 Discussion

This chapter has illustrated how the processes of fracture in ice can be quantified using the results of linear elastic fracture mechanics and dislocation theory. The resulting crevasse depths that were found using an LEFM analysis were considerable and in the range of depths that are observed to exist in glacial ice. Though this analysis was a simple application using constant tensile stresses with depth, the results are encouraging. Later in this thesis, a more accurate model of the stresses in floating ice will be developed, and this will be used to improve upon the results calculated here.

Dislocation theory provides valuable insights into the geometries of newly formed crevasses. These results are also corroborated by field evidence, seen in the reports of Swithinbank (1999). The small sizes of the crevasses that are created is an important discovery because it implies that other, slower acting processes are at work in opening up and lengthening the crevasses over time. These ideas will be explored further in the following chapter, where a model of crevasse growth for a material experiencing creep will be developed and applied to floating ice.

CHAPTER 3

DUCTILE CRACK GROWTH

3.1 Overview

The analysis of crack growth in ice using linear elastic fracture mechanics (LEFM) provides a valuable tool for predicting the necessary conditions for unstable crack growth. It is not a useful approach when considering the ductile properties of ice and slower crack propagation speeds. Results presented in the previous chapter (see §2.5) demonstrated that crack formation in the LEFM framework was on the order of the speed of sound in the material. This does not allow an examination of more constrained crack growth in a material undergoing creep deformation. In this chapter, developments will be examined for crack growth in elastic-ductile materials, with the final result being a model describing crack growth rates more appropriate for glaciology.

The approach will make use of the fracture mechanics development shown previously, coupled with theories put forth to describe the stresses in a ductile medium. The final result will be a functional relationship describing crack growth rates in terms of both elastic and ductile parameters inherent to the material.

3.2 Stresses in a Material

Consider the standard definition of the stress field around a crack tip. Recall the form of the stresses with respect to the geometry and coordinate system shown in

Figure 3.1 (Kanninen and Popelar, 1985)

$$\sigma_1 = \frac{K_I}{\sqrt{2\pi r}} \cos\frac{\theta}{2}\left[1 + \sin\frac{\theta}{2}\sin\frac{3\theta}{2}\right] \tag{3.1a}$$

$$\sigma_2 = \frac{K_I}{\sqrt{2\pi r}} \cos\frac{\theta}{2}\left[1 - \sin\frac{\theta}{2}\sin\frac{3\theta}{2}\right] \tag{3.1b}$$

$$\sigma_{12} = \frac{K_I}{\sqrt{2\pi r}} \sin\frac{\theta}{2}\cos\frac{\theta}{2}\cos\frac{3\theta}{2} \tag{3.1c}$$

The problem to be considered is still mode I cracking, or tensile opening, where the

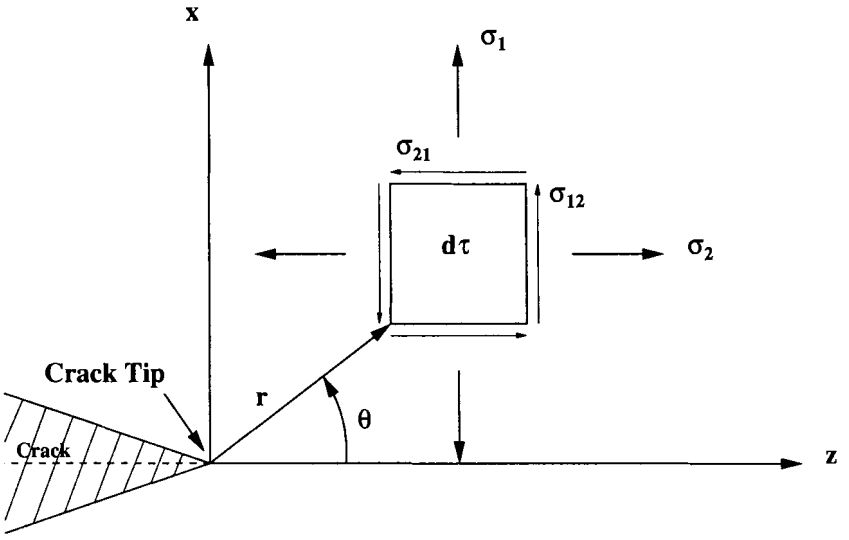

Figure 3.1: Geometry describing the stresses given in Eq. 3.1.

load is applied perpendicular to the crack faces. The simple form (Eq. 2.11)

$$K_I = \sigma\sqrt{\pi a}$$

describes the mode I stress intensity factor for a single crack, wholly contained in a medium, subjected to a far field tensile stress σ.

Now that a fracture mechanics background has been restated, an examination of the stress and strain in a material experiencing creep is necessary. Consider the case of plane stress in a material ($\sigma_3 = \sigma_{23} = \sigma_{13} = 0$), and apply Eq. 3.1 with $\theta = 0$ and $r = z$ (the axis along which the crack is propagating) and write

$$\sigma_1 = \frac{K_I}{\sqrt{2\pi z}} \tag{3.2}$$

The equation for power law creep is given by (Hughes, 1998)

$$\dot{\varepsilon}_{11} = \frac{B}{2^{(n+1)/2}}\left[(\sigma_1-\sigma_2)^2+(\sigma_2-\sigma_3)^2 + (\sigma_3-\sigma_1)^2\right]^{(n-1)/2}\left[(\sigma_1-\sigma_2)-(\sigma_3-\sigma_1)\right] \tag{3.3}$$

which, with the simplifications given above, can be written as

$$\dot{\varepsilon}_{11} = \frac{B}{2}\sigma_1^n = \frac{B}{2}\sigma_N^n \tag{3.4}$$

with subscript N denoting stress perpendicular, or normal, to the cracking plane. For elastic deformation, the stress σ_N can then be written as (Barnby and Nicholson, 1977)

$$\sigma_N = \frac{K_I}{\sqrt{2\pi z}} \tag{3.5}$$

and this is considered to be a transient stress at a fixed total strain. This elastic stress relation, as it converts to ductile strain, results in a steady state stress distribution that is given by (Barnby and Nicholson, 1977, Eq. 7)

$$\sigma_{ss} \propto z^{-1/2m} \tag{3.6}$$

It will be shown that this proportionality is incorrect, and that in fact the steady state stress is related to distance z in a slightly modified manner.

For ductile deformation, the relation between the steady state stress and distance from the crack tip can be found by considering the strain hardening and creep rate power laws:

$$\varepsilon = A\sigma^m \tag{3.7}$$

which is for strain hardening (Hughes, 1998, pg. 119), and

$$\dot{\varepsilon} = B\sigma^n \tag{3.8}$$

which is for steady state creep (Glen, 1955), where temperature is constant and A, B, m, and n are constants. The integrated form of Eq. 3.8 incorporates time into

constant B, making it equivalent to A. Then Eq. 3.8 takes the same form as Eq. 3.7, in which A is time dependent, assuming that $m=n$ (Evans, 1984, pg. 232). This is a reasonable assumption for ice, where $m=2$ and $1 \leq n \leq 3$ are commonly observed.

The complementary energy U per unit volume for an element ahead of the crack tip, using Eq. 3.7 for constant total strain ε at the crack tip, is written as

$$U = \int \varepsilon \, \mathrm{d}\sigma = \int A\sigma^m \, \mathrm{d}\sigma = \frac{A}{m+1}\sigma^{m+1} \tag{3.9}$$

(plus a constant of integration, which is ignored). Here it is claimed that all products of the form $\varepsilon\sigma$ must have a $1/z$ singularity at the crack tip, no matter what stress law is operating (Hutchinson, 1968; Rice and Rosengren, 1968). If this is the case, then the argument is made that U must also have such a singularity. Integrating Eq. 3.9 throughout the entire volume V to get the total energy U_T results in

$$U_T = \int \frac{A}{m+1}\sigma_{ij}^{m+1} \, \mathrm{d}V. \tag{3.10}$$

The steady state values σ_{ss} of σ_{ij} can be determined by considering a variational theorem such that

$$\frac{\mathrm{d}U_T}{\mathrm{d}\sigma_{ss}} = \frac{\mathrm{d}\left(\int \left[\frac{A}{m+1}\sigma_{ij}^{m+1} \, \mathrm{d}V\right]\right)}{\mathrm{d}\sigma_{ss}} = 0. \tag{3.11}$$

Since $\varepsilon\sigma$ varies as $1/z$ and $\int \varepsilon \, \mathrm{d}\sigma \propto \sigma_{ij}^{m+1}$ for constant ε according to Eq. 3.9, and only σ_{ij} depends on z in Eq. 3.10, solving Eq. 3.11 for σ_{ss} and setting $\sigma_{ij} \propto 1/z$ gives

$$\sigma_{ss} \propto z^{-1/(m+1)} \tag{3.12}$$

This result should be compared to the initial steady state stress relation stated in Eq. 3.6. Furthermore, since the local strains are determined by Eq. 3.7, they must display a dependence on $z^{-m/(m+1)}$:

$$\varepsilon = A\sigma^m \propto \left(z^{-1/(m+1)}\right)^m = z^{-m/(m+1)}$$

Thus far, the analysis has dealt with the creep induced stresses in the material. To connect the steady state plastic solution with the elastic solution, the assumption

is made (Barnby and Nicholson, 1977) that stresses along all points ahead of the crack tip relax via the relation $\varepsilon\sigma = Q^2$, where Q is some constant (see Fig. 3.2). The value of Q is squared to prevent negative values of the strain energy $\varepsilon\sigma$. This assumption results in a mathematical connection between the elastic stress-strain curve and the steady state plastic curve

$$\sigma_E \varepsilon_E = \sigma_{ss} \varepsilon_{ss} \tag{3.13}$$

where the subscript E denotes elastic strain and ss denotes steady state ductile strain. This relation is an equivalent way of saying the energies are equal at the intersections of the stress-strain curves and this hyperbola. The form of the elastic stress along this path is known through Eq. 3.5. Recasting Eq. 3.7 as $\varepsilon = A\sigma_{ss}^n$ for $m = n$ and

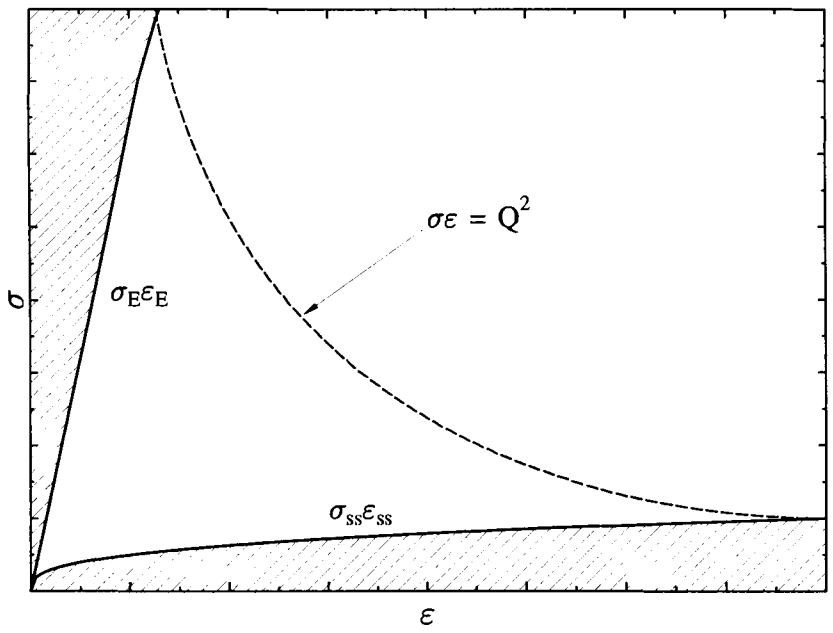

Figure 3.2: Illustration of the relaxation relation. The elastic stress strain curve (straight solid line) relaxes down to the power law stress strain curve (curved solid line) along points on the hyperbola (dashed line) such that the shaded areas representing strain energy are equal.

employing Eq. 3.13 results in

$$\begin{aligned} \sigma_{ss} &= \frac{\sigma_E \varepsilon_E}{\varepsilon_{ss}} \\ &= \frac{\sigma_E \varepsilon_E}{A \sigma_{ss}^n} \end{aligned} \tag{3.14}$$

Since $\sigma_E = E\varepsilon_E$ (Hooke's Law for an elastic material)

$$\sigma_{ss}^{n+1} = \frac{\sigma_E^2}{AE} \tag{3.15}$$

Substituting in the elastic normal stress from Eq. 3.5 for σ_E gives

$$\sigma_{ss}^{n+1} = \frac{K_I^2}{2\pi z AE} \tag{3.16}$$

which when simplified results in the final form

$$\sigma_{ss} = \left[\frac{K_I^2}{2\pi AE}\right]^{1/(n+1)} z^{-1/(n+1)} \tag{3.17}$$

This relation describes the steady state distribution of the stresses ahead of a crack tip, displaying the correct $z^{-1/(n+1)}$ behavior as predicted by Eq. 3.12 and including parameters for both the elastic (E, K) and ductile (A, n) properties of the material.

3.3 Crack Growth Law

Now that there is a functional relationship describing the stress ahead of a crack tip, it would be worthwhile to apply it to the problem of attempting to determine a crack growth model. The physical problem at hand is to determine how fast an edge crack will grow in a specimen with an applied tensile stress, subject to the material conditions described earlier. The original treatment of this problem was considered by Barnby and Nicholson (1977) with a correction and modification covered in Evans (1984).

To begin, consider the HRR (Hutchinson, Rice and Rosengren) stress fields of a power law hardening ductile material (Hutchinson, 1968; Rice and Rosengren, 1968).

The results derived in these papers give the normal stress fields (normal in relation to the plane along which the crack is propagating) as

$$\sigma = C^* r^{-1/(n+1)} \tag{3.18}$$

where C^* is related to the energies contained in the stress fields. For a pre-existing crack of depth l in a solid of thickness H, width W, and infinite length, the net load F that acts on the *uncracked* portion of the solid (Fig. 3.3) can be written as

$$F = W \int_0^{H-l} \sigma(r)\, \mathrm{d}r \tag{3.19}$$

where the normal stress $\sigma(r)$ is taken to be Eq. 3.17. Substituting and carrying out the integration (with r replaced by z), the force is found to be

$$F = W \left(\frac{K_I^2}{2\pi AE} \right)^{1/(n+1)} \left(\frac{n+1}{n} \right) (H-l)^{n/(n+1)}$$

Recognizing the first term in parentheses as $\sigma_{ss} z^{1/(n+1)}$ allows for the form

$$\sigma_{ss} = \frac{F}{W} z^{-1/(n+1)} \left(\frac{n}{n+1} \right) (H-l)^{-n/(n+1)}$$

Also recognizing the fact that the net stress on the uncracked portion can be written as

$$\sigma_{\text{net}} = \frac{F}{(H-l)W}$$

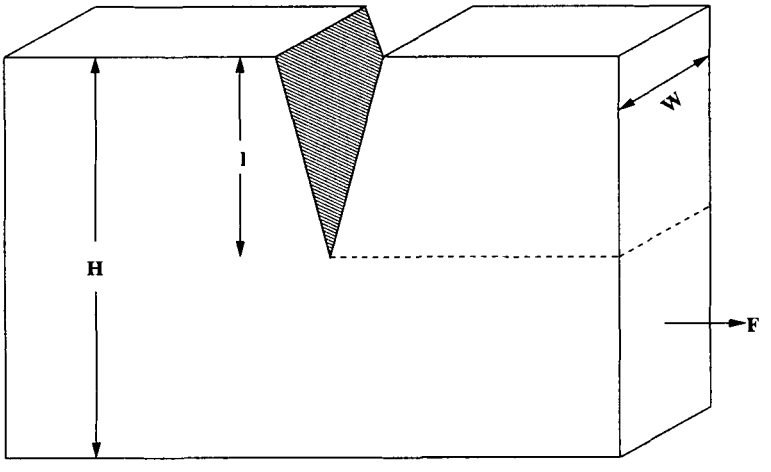

Figure 3.3: Geometry of the system for Eq. 3.19.

a factor of $1/(H-l)$ can be factored and σ_{ss} can be written as

$$\sigma_{ss} = \frac{n}{n+1}\sigma_{\text{net}}\left(\frac{x}{H-l}\right)^{-1/(n+1)} \tag{3.20}$$

which relates the normal stress field ahead of the crack tip to geometric properties of the system and the strain hardening exponent, values for which are readily available.

For practical applications of this formula, consider the case of a single "blunted" edge crack in the solid (Evans, 1984, pg. 213). A blunted crack is defined as a crack where the two faces do not meet in a sharp point. Rather, they are joined by a ligament of some length (Fig. 3.4). This convention allows an explicit form for the crack growth rate to be determined. If the length of the ligament is ϕ, the critical ligament length for growth is given by (Evans, 1984, pg. 213)

$$\phi_c = \varepsilon_f \phi \tag{3.21}$$

where ε_f is the failure strain of the ligament. The displacement rate of the ligament a distance d_c from the crack tip can be written as

$$\dot{\phi} = (\dot{\varepsilon}\phi)_{z=d_c} \tag{3.22}$$

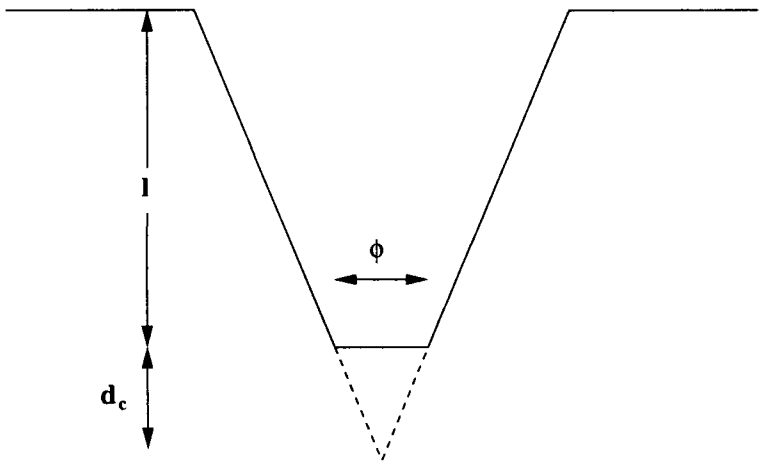

Figure 3.4: Blunted crack tip and variables to describe the geometry as defined by Evans.

with $\dot{\varepsilon} = A\sigma^n$, the flow law for ice. Letting $\sigma = \sigma_{ss}$ in Eq. 3.20 allows one to write

$$\dot{\phi} = \phi A \left(\frac{n\sigma_{\text{net}}}{n+1} \right)^n \left(\frac{H-l}{d_c} \right)^{n/(n+1)} \tag{3.23}$$

The important assumption for crack growth is allowing the crack to move forward a distance d_c when the displacement acquires the critical value ϕ_c. This can be written in terms of the overall crack growth rate as (Evans, 1984, pg. 233)

$$\dot{l} = \frac{\dot{\phi}}{\phi_c} d_c \tag{3.24}$$

The definition of ϕ_c is given by Eq. 3.21 and this can be substituted into Eq. 3.23 for the crack growth rate

$$\dot{l} = \frac{A}{\varepsilon_f} \left(\frac{n\sigma_{\text{net}}}{n+1} \right)^n (H-l)^{n/(n+1)} d_c^{1/(n+1)} \tag{3.25}$$

An explicit form for crack length as a function of time can be obtained by rewriting Eq. 3.25 in the form

$$\dot{l} = k\,(H-l)^{n/(n+1)} \tag{3.26}$$

In this expression, the variable k has been introduced as

$$k = \frac{A}{\varepsilon_f} \left(\frac{n\sigma_{\text{net}}}{n+1} \right)^n d_c^{1/(n+1)}$$

It is necessary for the crack to have some initial depth l_o at time $t = 0$ in this model formulation. Therefore, the integration of Eq. 3.26 with these explicit limits is

$$\int_{l_o}^{l} \frac{\mathrm{d}l}{(H-l)^{n/(n+1)}} = \int_0^t k\,\mathrm{d}t' \tag{3.27}$$

which yields the solution

$$l(t) = H - \left[(H-l_o)^{1/(n+1)} - (n+1)\,kt \right]^{n+1} \tag{3.28}$$

which is valuable if only for its simplicity, considering the analysis that was employed to obtain it.

Simplicity aside, there are issues that arise when applying Eq. 3.28 to real problems involving ice. The assumptions that were made regarding the blunted vs. sharp crack tip were necessary so that a model solution could be found. Parameters that are introduced with these assumptions are problematic. The failure strain ε_f of ice is not well understood, but some approximations can be made, and these will be discussed later. The biggest shortcoming of this model is the parameter d_c. It has some basis in fact for ductile fracture, but its main purpose was to allow a feasible crack growth mechanism that could be explicitly solved. The question remains as to what is a viable range of values for this parameter. Later applications of Eq. 3.28 will be done for a range of values in order to investigate the sensitivity of the model to this parameter.

3.4 Applications to Ice Shelves

Now that a workable model describing the rate of crack growth in a solid has been found, attention is given to modeling situations typical in glaciology. The problem to be studied will be basal cracks propagating in floating ice shelves. This situation is chosen as a possible explanation in the formation of large, or tabular, icebergs. This analysis should not be considered definitive, since the unrealistic assumption of a constant stress with depth will be used. For purposes of analysis here, this assumption may be considered appropriate for basal crevasses, which will fill with water, thus experiencing a tensile stress throughout a large portion of the ice thickness. An analysis of this type is not applicable to air filled surface crevasses, since ice overburden pressure will surpass induced tensile stresses after several tens of meters of crevasse penetration. (A more detailed discussion using fracture mechanics is given in the next chapter where explicit forms for stress and other parameters with depth in the ice will be derived.) This section is only meant as an illustration of the derived model and results will hopefully show that the solutions are on the order of what may be expected in glaciological studies.

To start, some background on the profiles of ice shelves will be necessary, as the thickness of the ice shelf as a function of time and/or space is needed. This information will allow for the use of the crack growth model given by Eq. 3.25 with explicit values for total ice thickness included. The analysis will be done on an ice shelf that is spreading in only one direction, and the direction of spreading, x, will be the same as the direction of flow. Another simplification that will be included is a near zero side shear stress. With these two conditions the mass balance for ice can be written as (van der Veen, 1999)

$$CH^{n+1} + U\frac{\mathrm{d}H}{\mathrm{d}x} = M \tag{3.29}$$

where H is the ice shelf thickness, U is a velocity averaged over the thickness of the ice, n is the exponent in the flow law for ice, and M is the accumulation rate (positive or negative). The parameter C is given by

$$C = A\left[\frac{\rho_i g\left(\rho_w - \rho_i\right)}{4\rho_w}\right]^n \tag{3.30}$$

with A the ice hardness parameter in the flow law and ρ_i, ρ_w the densities of ice and water respectively. The solutions to Eq. 3.29 are readily found if the problem is considered for three different cases of accumulation rate: $M = 0$, $M < 0$, and $M > 0$.

An accumulation rate of zero is the simplest case mathematically, but it is also the most unrealistic. For $M = 0$, Eq. 3.29 reduces to

$$CH^{n+1} + U\frac{\mathrm{d}H}{\mathrm{d}x} = 0$$

which can be solved by integrating

$$\int_{H_o}^{H} \frac{\mathrm{d}H}{H^{n+1}} = -\int_0^x \frac{C}{U}\,\mathrm{d}x'$$

The solution to this equation is

$$H(x) = \left[\frac{(n+1)C}{H_o U_o}x - H_o^{-1/(n+1)}\right]^{-1/(n+1)} \tag{3.31}$$

where the initial conditions on thickness $H = H_o$ and velocity $U = U_o$ are taken across the grounding line $x = 0$ of the ice shelf.

In the second case, a net accumulation rate greater than zero is considered. This means that while some portion of the ice shelf can lose material, through basal melting, surface wind ablation or other mechanisms, the overall mass balance of the ice shelf is positive. A solution to Eq. 3.29 in its full form must be determined. With the aid of a table of integrals (Beyer, 1991), the solution is found to be

$$H(x) = \left[\frac{C}{M} - \frac{U_o^{n+1} \left(\frac{C}{M} H_o^{n+1} - 1 \right)}{(Mx + H_o U_o)^{n+1}} \right]^{-1/(n+1)} \tag{3.32}$$

For the final case of a net accumulation rate less than zero, the same physical reasoning applies as in the previous case. The ice shelf may be experiencing local positive accumulation but overall the mass balance is negative. To solve, let $\hat{M}$ replace $-M$ in Eq. 3.29 and follow the same procedure that yielded Eq. 3.32 to get (with an appropriate change of variables back to M)

$$H(x) = \left[\frac{U_o^{n+1} \left(1 + \frac{C}{M} H_o^{n+1} \right)}{(H_o U_o - Mx)^{n+1}} - \frac{C}{M} \right]^{-1/(n+1)} \tag{3.33}$$

Now that the profiles are available in mathematical form, an attempt can be made to use Eq. 3.25 in a physical system. The goal is to try to obtain a quantitative estimate of how long it will take a basal crack to propagate entirely through the thickness of an ice shelf.

The thickness profiles determined in Eqs. (3.31), (3.32), and (3.33) are utilized and substituted into Eq. 3.28. This results in a crack growth model that is dependent on time and distance along the flowline, i.e.

$$l(t; H) \rightarrow l(t, H(x))$$

A relation of this form is still not entirely useful since the desired result is a model that is dependent only on time. However, the equations describing the ice shelf profiles

are functions of longitudinal distance from the grounding line, so a simple solution exists. If it is assumed that the ice shelf is moving forward at a constant velocity u_x throughout its entire thickness (a realistic assumption since the ice is floating), the distance along the flow can be related to time by letting

$$x = u_x t$$

in the profile equations. (However, both the velocity u_x and accumulation rate M *are* functions of longitudinal distance x.) This changes the spatial dependency of the profile to a temporal dependency with velocity as a parameter, thus

$$H(x) \rightarrow H(x(t)) \rightarrow H(t; u_x)$$

where it is understood that a constant velocity throughout the length is never found in nature. (Due to mass balance considerations, the ice shelf can change its speed along the flow direction if it is thinning or thickening.) Assuming constant ice velocity will not be a concern because the model assumes that a crevasse has formed (by some means of no real concern here) and is now being carried along in the direction of flow, while at the same time propagating through the thickness of the ice shelf. These facts allow a determination of not only the time when a crevasse will penetrate through the thickness but also the downstream location. When used in conjunction with a model that predicts the spacings of crevasses, this can become a powerful tool for determining the size and frequency with which tabular icebergs form.

3.4.1 Modeling a Typical Glacier

The relation given by Eq. 3.28 is modeled for a typical ice shelf. It is imagined that a basal crack of some height l_o nucleates at the grounding line, where longitudinal strain $\partial u/\partial x$ is greatest, at time $t = 0$. The crack will grow in the vertical direction as it propagates horizontally with velocity u_x, the velocity of the ice shelf. In the model, the thickness at the grounding line, H_o, is taken to be 1000 m and velocity there, $U_o = u_x$,

to be 250 $^{m}/_{yr}$. The ice hardness parameter A is taken to be $6.8 \times 10^{-24}\,Pa^{-3}\,s^{-1}$ for $T = 0\,°C$ (Paterson, 1994), the approximate temperature of the sea water that is in contact with the crevasse walls. A failure strain $\varepsilon_f = 0.4$, the recrystallization strain of ice, is chosen (Hughes, 1998) and a net stress of 1 bar is used in the calculations. It is also imagined that a surface crevasse of depth a forms directly above the basal crevasse. From fracture mechanics arguments, the initial height of the basal crack is taken to be 21 m and the depth of the surface crevasse is 32 m. The difference arises from using a lower value for the fracture toughness of ice at the surface versus the base (see Rist et al., 1996, 1999). The quantity δH is defined to be $H - l(t) - a$ and the time t_{meet} is achieved when $\delta H = 0$. It is at this point in time that the two crevasses have joined together, penetrating completely through the ice shelf.

3.4.2 Results

Profiles for each case of accumulation rate are considered ($M = 0$, $M > 0$, $M < 0$) as are results for a range of values of d_c (the measure of the bluntness of the crack tip). The time t_{meet} and distance L_{meet} from the grounding line to the point where the crevasses join are calculated. Table 3.1 summarizes the results.

d_c (m)	M ($^{m}/_{yr}$)	t_{meet} (yrs)	L_{meet} (km)
0.1	-1	46.5	11.6
	0	47.6	11.9
	1	48.2	12.0
1	-1	28.6	7.2
	0	29.1	7.3
	1	29.2	7.3
5	-1	20.3	5.1
	0	20.1	5.1
	1	20.6	5.1

Table 3.1: Summary of results for three different ice sheet profiles and a range of values d_c.

It can be seen from these results that as d_c increases, the accumulation rate (and therefore the ice-shelf profile) becomes less important in determining the time it takes for the cracks to meet. However, it is interesting to note that even though d_c increases by a factor of 50, the time to meet only decreases by a factor of two. The effect of the parameter d_c in determining the rate at which cracks grow is minimal, which is encouraging since determining an actual value for this parameter is difficult at best.

3.5 Discussion

It was mentioned at the conclusion of Chapter 2 that the results of a linear elastic fracture mechanics analysis were encouraging in their scale, because it implied that other processes needed to be considered to explain the observed crevasse geometries and crevasse growth rates in glacial ice. Opening widths were derived and found to be only in the range of millimeters. Crevasse fields show opening widths orders of magnitude greater, anywhere from centimeters to many meters. The time for crevasses to crack through the ice entirely is also much slower than the results of §2.5 demonstrate. Clearly, another process was necessary to explain how a crevasse that started so small could increase its width by such a great amount, but on a time scale that is relevant to a discussion of crevassing and calving of glacial ice. This chapter made use of the creep properties of ice to quantify these observations. A model of crevasse growth was derived that used creep deformation to explain the widening and lengthening of the crevasses over time. Calculated results using this model have time scales on the order of decades and a length scale on the order of 10's of kilometers before crevasses will entirely penetrate the ice, which are clearly more "glacial."

CHAPTER 4

FRACTURE AND BACK STRESS

4.1 Overview

Using the tools developed by a linear elastic fracture mechanics analysis one can make predictions about intrinsic properties of flowing ice. It has been posited that there exists a back stress in flowing ice which, as the name suggests, impedes the flow of the ice. This back stress is defined qualitatively as anything that does not aid in the forward motion of the ice. Some examples of contributions to back stress in ice are local pinning (grounding) points, side shear of ice flowing through the confines of a fjord, and lateral drag as slower moving ice, bordering a faster moving ice stream, is "sucked in" and dragged along, thus slowing the faster stream. Another cause of back stress is the buttressing effect an ice stream experiences as it flows into a large, floating ice shelf, as is the case in many locations in Antarctica (Thomas, 1973a,b). There are numerous ice streams that flow from both West and East Antarctica into the Ross Ice Shelf, as well as streams flowing into the Filchner and Ronne Ice Shelves in East and West Antarctica, and streams that flow into the Amery Ice Shelf, also in East Antarctica.

This chapter will make use of fracture mechanics in an attempt to predict the magnitudes of this back stress. If crevasses exist in floating ice and do not penetrate to their maximum allowed depth, as a fracture mechanics analysis would predict, then some back stress can be assumed to exist. The back stress must then be explicitly included in the overall stress analysis, resulting in crevasse penetration depths less than $a_{\max}$. When observed crevasse depths are matched to the results of an analysis

that includes the back stress, the magnitudes of the resistive/compressive stresses will then be known. This procedure will be carried out along the floating portion of Byrd Glacier.

4.2 Stresses in Floating Ice

A quantitative analysis of back stress has been done by Rist et al. (2002) on the Ronne Ice Shelf using fracture mechanics. Field data, including ice cores to determine density profiles and fracture toughness, were taken along a flowline on the floating ice. Measurements of basal crevasse penetrations were also taken along the same flowline.

In order to employ a fracture mechanics analysis, the stresses in floating ice need to be determined. The longitudinal extending stress σ_{xx} can be written as

$$\sigma_{xx} = \sigma'_{xx} + \frac{1}{3}\left(\sigma_{xx} + \sigma_{yy} + \sigma_{zz}\right)$$

where σ'_{xx} is the deviator stress. The incompressibility of ice requires that

$$-\left(\sigma'_{xx} + \sigma'_{yy}\right) = \sigma'_{zz}$$

which allows the simplification

$$\sigma_{xx} \approx \sigma'_{xx} + \sigma_{zz}$$

The deviator stress is determined by the flow law of ice

$$\sigma'_{xx} = B(z)\left(\frac{\dot{\varepsilon}_{xx}}{\Theta}\right)^{1/3}$$

so with these simplifications the stress in the horizontal direction can be written as (Thomas, 1973a,b)

$$\sigma_{xx} = B(z)\left(\frac{\dot{\varepsilon}_{xx}}{\Theta}\right)^{1/3} + \sigma_{zz} \tag{4.1}$$

The term in parentheses is the contribution to the stress due to creep of the ice, while the second term, σ_{zz}, is the ice overburden pressure. Here, B is the ice softness

parameter, which is dependent on depth through temperature, and Θ is a combination of variables that incorporate the relative contribution of shear and transverse stresses. The term in parentheses is taken to be constant (Rist et al., 2002). With this assumption, the constant term can then be isolated and solved for by balancing the force exerted by the ice column and that due to water pressure (Weertman, 1957)

$$\int_b^s \sigma_{xx}\,\mathrm{d}z = \rho_w g \int_b^0 z\,\mathrm{d}z \tag{4.2}$$

where b and s represent the base and surface of a floating ice shelf with a coordinate system originating at sea level (Fig. 4.1). Substituting Eq. 4.1 into Eq. 4.2 and integrating the right hand side explicitly gives

$$\int_b^s \left\{ B(z) \left(\frac{\dot{\varepsilon}_{xx}}{\Theta} \right)^{1/3} + \sigma_{zz} \right\} \mathrm{d}z = -\frac{1}{2}\rho_w g (H-h)^2 \tag{4.3}$$

for ice with a total thickness H and height above sea level h. Since ice density ρ_i is not constant with depth (Paterson, 1994; Rist et al., 1996, 1999, 2002), ice overburden pressure is written as

$$\sigma_{zz} = -g \int_z^s \rho_i(z')\,\mathrm{d}z'$$

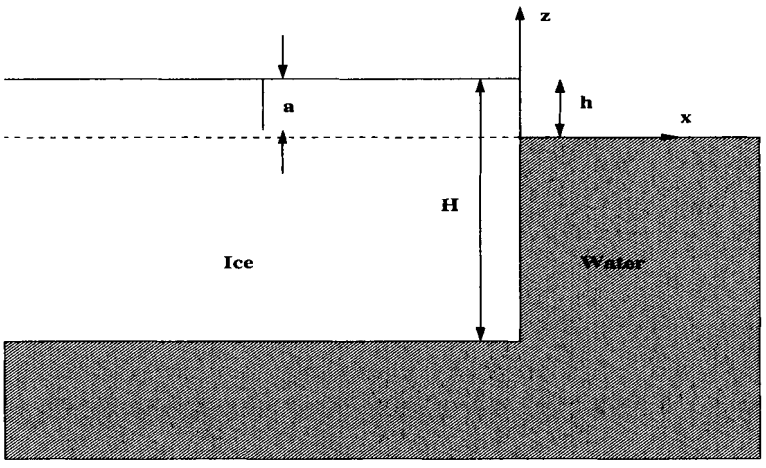

Figure 4.1: Geometry for stress and fracture mechanics analysis.

where z' is a dummy integration variable, and the height above sea level to which a floating ice column will rise is

$$h = H - \frac{1}{\rho_w} \int_b^s \rho_i(z)\,\mathrm{d}z$$

Substituting these values into Eq. 4.3 and solving for the constant term gives

$$\left(\frac{\dot{\varepsilon}_{xx}}{\Theta}\right)^{1/3} = \frac{1}{\int_b^s B(z)\,\mathrm{d}z}\left\{g\int_b^s\int_z^s \rho_i(z')\,\mathrm{d}z' - \frac{g}{2\rho_w}\left(\int_b^s \rho_i(z)\,\mathrm{d}z\right)^2\right\} \tag{4.4}$$

which can then be inserted into the original expression for the longitudinal stress in Eq. 4.1 to yield

$$\sigma_{xx} = \frac{B(z)}{\int_b^s B(z)\,\mathrm{d}z}\left\{g\int_b^s\int_z^s \rho_i(z')\,\mathrm{d}z' - \frac{g}{2\rho_w}\left(\int_b^s \rho_i(z)\,\mathrm{d}z\right)^2\right\} - g\int_z^s \rho_i(z')\,\mathrm{d}z' \tag{4.5}$$

This relation now gives one an explicit formula for the longitudinal stress acting at any depth z in floating ice. It is a non-linear relation determined by the dependence of density on depth and the dependence of B on temperature. Both of these effects will be explicitly addressed later.

4.3 Back Stresses in Floating Ice

Back stress can be accounted for in the treatment by considering a depth averaged back stress σ_{back} of the form (Thomas and MacAyeal, 1982)

$$\sigma_{\text{back}} = \frac{1}{H}\left(\frac{\dot{\varepsilon}_{\text{back}}}{\Theta}\right)^{1/3}\int_b^s B(z)\,\mathrm{d}z \tag{4.6}$$

This can then be subtracted from the stress given in Eq. 4.5 to give a final depth dependent stress

$$\sigma_{xx} = \frac{B(z)}{\int_b^s B(z)\,\mathrm{d}z}\left\{g\int_b^s\int_z^s \rho_i(z')\,\mathrm{d}z' - \frac{g}{2\rho_w}\left(\int_b^s \rho_i(z)\,\mathrm{d}z\right)^2 - \sigma_{\text{back}}H\right\}$$

$$- g\int_z^s \rho_i(z')\,\mathrm{d}z' \tag{4.7}$$

The inclusion of a back stress term allows for a general description of the stresses acting on the ice. In a fracture mechanics framework, the stress described by Eq. 4.7 lets one calculate the stresses acting on a crevasse within the ice. Ice around a non water-filled crevasse (most likely a surface crevasse in the presence of little or no surface melting) will be subject to a tensile stress σ given by

$$\sigma = \sigma_{xx} \tag{4.8a}$$

while a for water filled crevasse (on the surface or at the base), σ will be given by

$$\sigma = \sigma_{xx} + \sigma_w \tag{4.8b}$$

where $\sigma_w = -\rho_w g z$.

A final note on the abstruse notion of back stress. This treatment does not attempt to make obvious where the back stress contributions arise. As written, σ_{back} incorporates *any* effect that does not aid in the forward progress of the ice. Stresses can not be measured outright; rather, they can only be inferred through the measurement of other quantities. What is being done here is to take the inference one step further. Only the magnitudes, not the causes, of back stress are found. Future analysis would be necessary to validate the magnitudes determined here, as well as the actual causes.

4.4 Fracture Mechanics

A previous chapter in this work dealt with fracture mechanics and the results of an analysis utilizing only constant tensile stresses. It is now necessary to utilize a stress intensity factor that is derived for a depth dependent tensile stress. In order to do this, it is necessary to recast the stress in terms of a polynomial expansion

$$\sigma = \sum_n C_n \left(\frac{z}{H}\right)^n \tag{4.9}$$

With the stress written in this form, the mode I stress intensity factor can be found by using (Fett et al., 1990)

$$K_I = \sqrt{a\pi} \sum_n C_n F_n \left(\frac{a}{H}\right)^n \tag{4.10}$$

where a is the crevasse depth and the F_n are weighting functions determined to be

$$F_n = \frac{\sqrt{2}}{\pi} n! \left[\frac{\Gamma(1/2)}{\Gamma(n+3/2)} + A_1 \frac{\Gamma(3/2)}{\Gamma(n+5/2)} + A_2 \frac{\Gamma(5/2)}{\Gamma(n+7/2)} + A_3 \frac{\Gamma(7/2)}{\Gamma(n+9/2)} \right] \tag{4.11}$$

with Γ representing the standard gamma function.

The expression given by Eq. 4.10 is determined by Fett et al. to be valid for $n \leq 5$ and crevasse depths $\alpha = a/H \leq 0.9$. The A_i are relations in α given by Fett et al. as (including a sign correction in A_3 discovered by Rist et al. (2002))

$$\begin{aligned} A_1 &= (0.4523 + 1.1690\alpha + 8.5078\alpha^2 - 13.6598\alpha^3 \\ &\quad + 4.4806\alpha^4)/(1-\alpha)^{3/2} \end{aligned} \tag{4.12a}$$

$$\begin{aligned} A_2 &= (0.7017 - 2.2134\alpha + 2.7344\alpha^2 + 4.6756\alpha^3 \\ &\quad - 6.0185\alpha^4)/(1-\alpha)^{5/2} \end{aligned} \tag{4.12b}$$

$$\begin{aligned} A_3 &= (-0.3102 + 0.9970\alpha - 0.5156\alpha^2 - 2.0149\alpha^3 \\ &\quad + 1.8843\alpha^4)/(1-\alpha)^{5/2} \end{aligned} \tag{4.12c}$$

Figure 4.2 shows the agreement of the stress intensity factors calculated using Eq. 2.12 and Eq. 4.10 for the simple case of a constant stress σ_o. In this case, the C_n of Eq. 4.9 with $n \geq 1$ are zero and $C_0 = \sigma_o$. Confidence in applying Eq. 4.10 to systems with more complicated stresses is increased due to the excellent agreement shown in Figure 4.2.

For these more complicated systems, the use of Eq. 4.10 is then a straightforward matter of recasting the stress given by Eq. (4.8a) or (4.8b) as a polynomial in z. Coefficients with $n \leq 5$ are then inserted into Eq. 4.10 and the stress intensity factor is calculated.

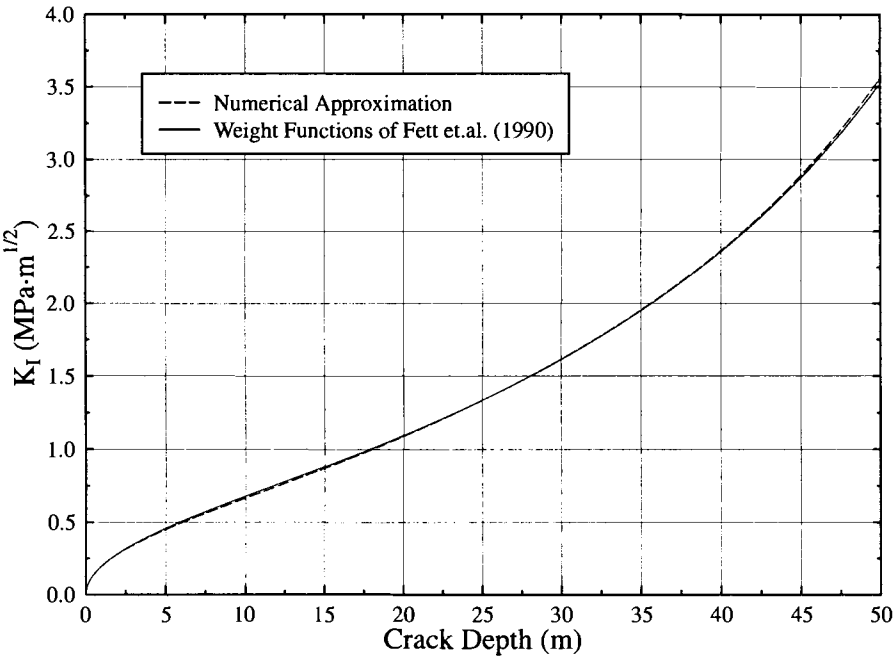

Figure 4.2: Comparison between the weight function given by Eq. 4.10 and the numerically derived solution in Eq. 2.12 for an edge crack subjected to constant tensile stress. Tensile stress $\sigma_o = 0.1$ MPa and sample thickness $H = 100$ m.

4.5 Back Stress: Byrd Glacier

Studies have been done to determine a map of back stress contours along the Ross Ice Shelf (Thomas and MacAyeal, 1982, pg. 409). This earlier work dealt mainly with the western portion of the ice shelf, calculating what the authors call a "retarding force," using measurements of strain rate at a number of field stations and numerically computing the retarding force necessary to reconcile these measured strain rates with strain rates calculated assuming the ice shelf was unopposed.

This new work will deal with a portion of the ice shelf on the eastern side, although a comparison can be made to the earlier results from the west. Data collected in previous flights over Byrd Glacier, which flows from the East Antarctic Ice Sheet through a fjord in the Transantarctic mountains, into the Ross Ice Shelf, resulted in

a number of elevation and velocity measurements along the grounded and floating portion of the glacier (Brecher, 1982; see also Appendix A). Using these data allows one to see that there are portions of Byrd Glacier that are experiencing compressive flow. In these regions it can be expected that crevasses will not form, since the stresses are no longer purely extending, or are of a small enough magnitude that a crevasse is impeded in its growth. Satellite imagery also allows one to see that within the fjord the floating ice seems to be uncrevassed. It is after the ice leaves the confines of the fjord and is released into the ice shelf that an extending and divergent flow pattern becomes apparent. Crevasse patterns also appear at this point in the imagery. Because crevasse depths are dependent on the net applied stresses, if the depths are known, or assumed to be some value, the net stress at any given location along the flowline can be deduced.

The data necessary to apply Eq. 4.8a include a knowledge of the relation of density with depth, the thickness of the floating portions of the ice, and some idea of how the flow law parameter $B(z)$ is defined. As noted earlier, it has been found that an exponential relation best describes the density as a function of depth

$$\rho_i(z) = \rho_i - (\rho_i - \rho_s)\, e^{-z/c} \tag{4.13}$$

where ρ_i is the density of pure ice, ρ_s is density of snow and firn at the surface, z is the depth below the surface, and c is a constant determined by location.

The determination of $B(z)$ is a little more involved since it is a function of temperature T, which varies with depth. However the relation between T and z can be quite complicated so a numerical solution for $B(z)$ is necessary. The most general form for $B(z)$ is an Arrhenius relation

$$B(z) = B_o \exp\left(\frac{Q}{nRT(z)}\right)$$

with n the number of moles, R the universal gas constant ($8.31\,{}^{\mathrm{J}}/_{\mathrm{mol\,K}}$), and Q the activation energy for creep in ice, which is double-valued, depending on temperature.

The values most commonly chosen are given as (Paterson, 1994)

$$Q = \begin{cases} 60,000\,\mathrm{J/mol} & T < -10\,^{\circ}\mathrm{C} \\ 139,000\,\mathrm{J/mol} & T \geq -10\,^{\circ}\mathrm{C} \end{cases}$$

The value of $B(z)$ also then depends on temperature in this binary fashion; thus, B_o is also double-valued and is chosen so that the function is continuous, but not necessarily differentiable, at the point where the transition takes place.

Finding the temperature profile of a glacier is a complicated process that will not be covered here. It is derived from the steady-state heat equation

$$\alpha \frac{\partial^2 T}{\partial z^2} = u_z \frac{\partial T}{\partial z}$$

describing the temperature T as a function of depth z. The vertical velocity u_z describes heat advection in the vertical direction and α is the thermal diffusivity (not to be confused with the α's found in Eq. 4.12). A more complete discussion of heat flow and temperature profiles in glaciers can be found in sources dedicated to the topic (see Zotikov, 1986, chapters 3 & 4). It can be noted here that the temperature profile of a glacier is dependent on its mass balance. Calculations to find the mass balance, the location of the grounding line, and thus the extent of floating ice and derived ice thicknesses can be found in Appendix A at the end of this thesis.

For calculations done here, the surface ice temperature is chosen as -25 °C (Thomas, 1976; Thomas et al., 1984). Basal temperatures, for ice in contact with sea water, are taken to be near -3 °C, slightly lower than earlier calculations. The results in Appendix A indicate that Byrd Glacier is undergoing basal melting. A typical temperature profile for basal melting conditions can be seen in Figure 4.3.

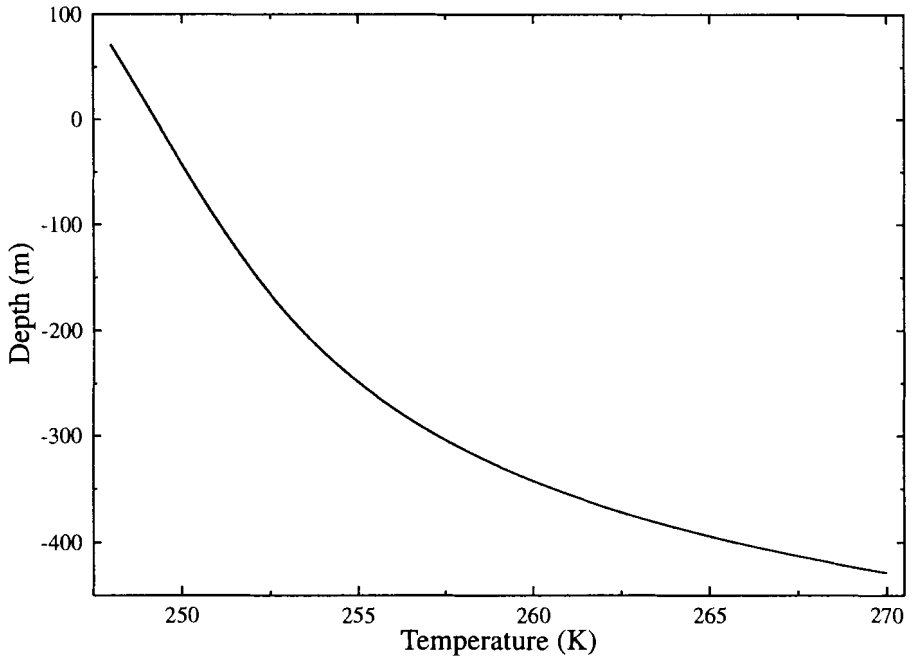

Figure 4.3: The temperature profile as a function of depth for a glacier of thickness 500 m experiencing basal melting. Surface ice temperature is -25 °C and basal ice temperature is -3 °C.

4.6 Calculation

A lack of firm crevasse data does not preclude a calculation of the back stresses in Byrd Glacier from being performed. Instead, consider the following two cases (see Figure 2.8 for definitions of stable and unstable crevasse growth):

1. *No unstable surface crevasse growth* - This case would result in the minimum back stress required so that surface crevassing would remain within the stable regions of crack growth. The magnitude of the stress intensity factor for the crack would remain below the fracture toughness for all crack depths a.

2. *50% crevasse growth* - This case results in the back stress if crevasses are assumed to be present and are 50% of the maximum depth ($a_{\max}$) they would attain through a fracture mechanics analysis of unimpeded flow, i.e. $\sigma_{\text{back}} = 0$.

These two cases will give a solid demonstration of the use of the model developed here and any later use can be easily adapted to match collected data. Values of the back stress can be found by application of Eq. 4.8a and iterating through the back stress until surface crevasse depths found using Eq. 4.10 match what is observed or is posited to exist. At points in the fjord, Byrd Glacier is undergoing compressive flow and it is assumed that surface crevasse formation is completely retarded in this region. Once the glacier begins to float, ice thicknesses are inferred using the non-linear density relation given by Eq. 4.13 and the ice elevation measurements. Thicknesses range from 800 m near the grounding line to 350 m as the ice exits the fjord. Utilizing Eq. 4.7 for these various ice thicknesses H enables one to calculate the stresses present in the ice. There are three unique components to the stress: the constant tensile stress due to creep, the ice overburden stress, and the back stress. The mode I stress intensity factor for tensile cracks is found by recalling that the net stress intensity factor is the sum of the individual stress intensity factors contributing to the stress

$$K_{\text{total}} = \sum_i K_i = K_{\text{tensile}} + K_{\text{overburden}} + K_{\text{back}}$$

where each K_i is found using Eq. 4.10 (subscript I denoting the mode for each K is assumed to be understood, thus is omitted for clarity).

The method to determine the desired back stress is relatively simple. The steps given here are for the first case listed at the start of this section, but can be extended to cover any known crevasse data. First, the total stress is calculated for a given ice thickness H with $\sigma_{\text{back}} = 0$ in Eq. 4.7. This allows for a calculation of the maximum stress intensity factor for that ice thickness, using Eqs. (4.9) and (4.10). The values of $a_{\max}$ can also be found by solving $K_{\text{total}} = K_{Ic}$. Figure 4.4 illustrates the complete results for this calculation. Second, the stress in Eq. 4.7 is re-calculated with some non-zero value of σ_{back} included, and the stress intensity factor is again determined. This process continues for various values of σ_{back} until the maximum value of the resulting SIF is tangent to the fracture toughness K_{Ic}. (For the second case listed

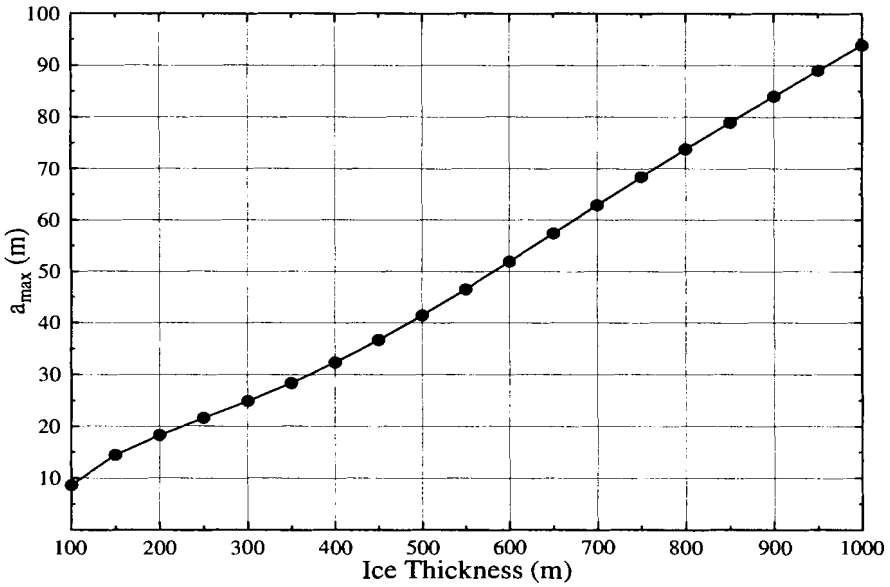

Figure 4.4: Maximum crevasse penetration as a function of ice thickness for zero back stress. Note how this plot differs from the ones shown in Figs. 2.13 and 2.14 along a similar range of ice thicknesses.

earlier, the back stress is varied until the SIF curve intercepts the fracture toughness at $a = \frac{1}{2}a_{\max}$.) The value of back stress that produces this effect is the critical back stress σ_{crit} required to inhibit unstable fracture. The process is then repeated for other ice thicknesses until the entire length of the flowline is covered. As a graphical illustration of this process, calculated stress intensity factors for ice of thicknesses $H = 400\,\text{m}$ and $H = 750\,\text{m}$ are shown in Figure 4.5. In each figure, the dashed line represents the fracture toughness of the surface ice K_{Ic}, determined by Rist et al. (2002) to be $0.15\,\text{MPa}\cdot\text{m}^{1/2}$ for floating shelf ice. Both figures also show the SIF whose maximum is tangent to the fracture toughness, which results in no unstable crevasse growth. A map of the back stresses necessary for this condition to hold true is shown in Figure 4.6.

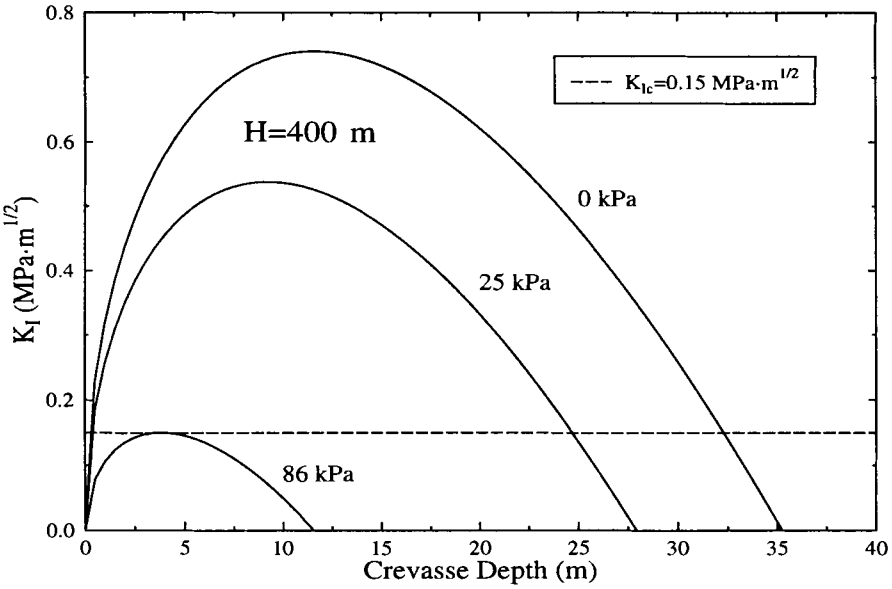

(a)

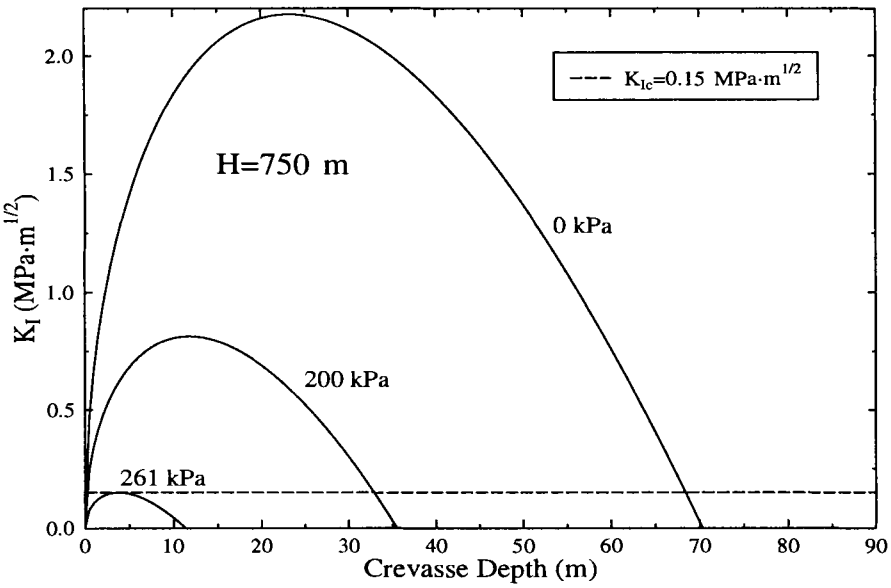

(b)

Figure 4.5: Stress intensity factor as a function of crevasse depth for a range of back stresses. In these figures, the back stress is varied until the maximum value of the SIF function is tangent to the fracture toughness. This process determines the value of σ_{crit} for a given ice thickness.

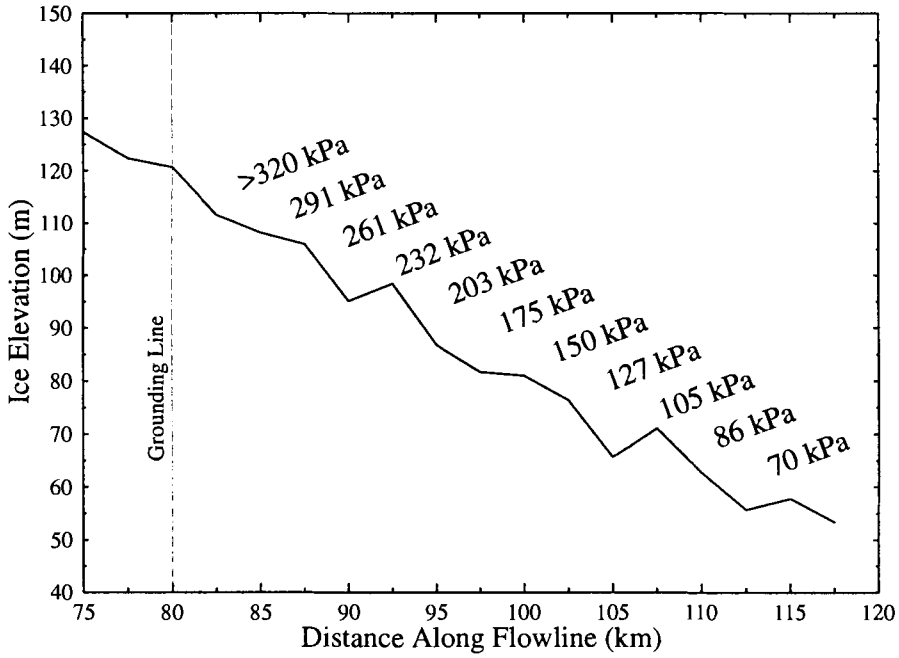

Figure 4.6: Back stresses required at locations along the floating portion of Byrd Glacier to prevent unstable crevasse growth. These values of back stress correspond to σ_{crit} discussed in the text.

The second case to be examined is for crevasse growth equal to $\frac{1}{2}\,a_{\text{max}}$. This fractional value of a is chosen simply as a midpoint between zero and maximum unstable surface crevassing. Any other fraction of a_{max} can just as easily be examined. Maximum crevasse depth as a function of ice thickness was shown in Figure 4.4; values of $\frac{1}{2}a_{\text{max}}$ are calculated from these results. The back stresses necessary to obtain cracks that are half their maximum allowed value are found by solving

$$K_{\text{total}}(a) = K_{Ic}$$

with the requirement that $a = \frac{1}{2}a_{\text{max}}$. A map similar to the one presented in Figure 4.6 is shown in Figure 4.7.

This work demonstrates the procedure for determining the back stresses along a flowline in floating ice. It can be applied to any field data that are collected, so

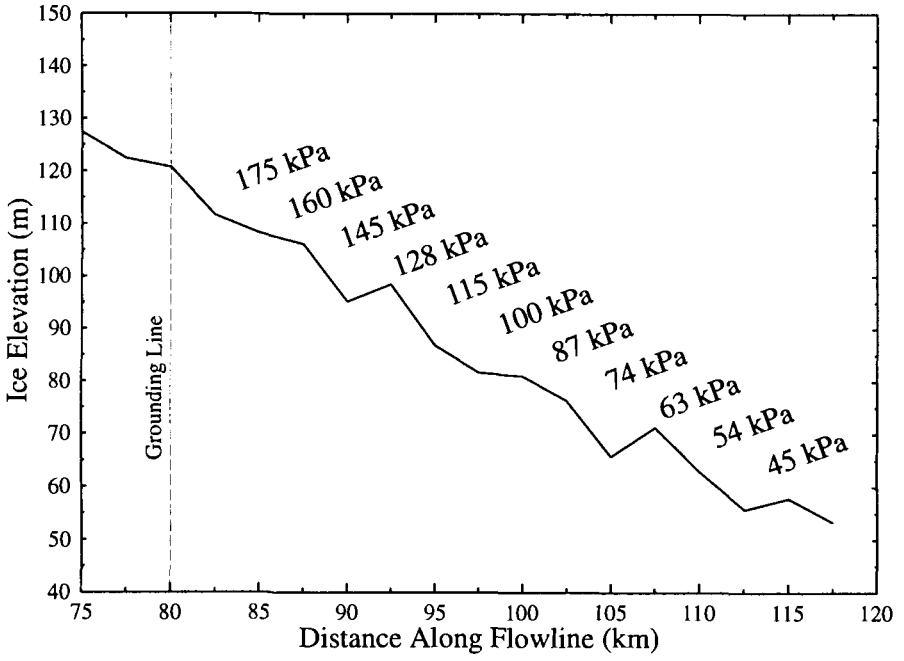

Figure 4.7: Back stresses at locations along the floating portion of Byrd Glacier such that crevasse growth $a = \frac{1}{2} a_{max}$ occurs.

when a crevasse is measured to be at some depth a_{observed}, the procedure can be implemented by following the steps outlined earlier. The values of back stress found here are appropriate when compared to previous work (Thomas and MacAyeal, 1982; Rist et al., 2002). While this may not be conclusive, it presents another avenue that future analysis can employ.

4.6.1 Basal Crevasses

The results of this analysis when applied to basal crevasses is interesting. A basal crevasse is the most obvious example of a water filled crevasse, since sea-water will rise into the crevasse as it penetrates into the ice. Water filled surface crevasses are inherently unstable due to the difference in the densities of water and ice (see §2.4.2 and references therein). The ice overburden pressure may not be sufficient to close a

crevasse that is filled to a high enough level with the denser water. Figure 4.8 shows the stress intensity factor for a basal crevasse, using Eq. 4.8b with $\sigma_{\text{back}} = 0$.

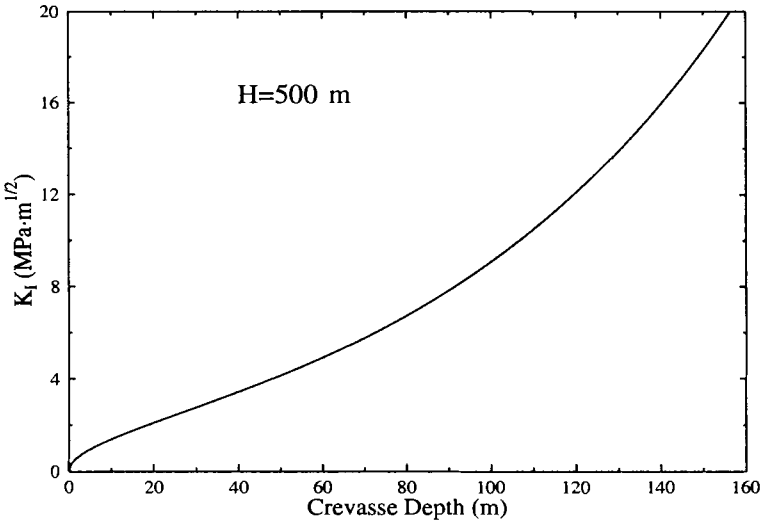

Figure 4.8: Stress intensity factor for a basal crevasse as a function of penetration depth, measured from the base of the ice, for $\sigma_{\text{back}} = 0$.

4.6.2 Instability of Water Filled Crevasses

The instability shown in the previous section leads to the observation that floating ice located where there is little or no back stress, as in the case of an unconfined ice tongue, can not exist when water filled crevasses are prevalent (Rist et al., 2002). Figure 4.8 shows that a basal crevasse in the presence of zero back stress has a stress intensity factor which increases for all crevasse depths a. This implies that any crevasse that forms can grow without bound. Basal crevasses which penetrate the entire thickness of ice shelves, providing they do not freeze shut first, have been discussed earlier (Weertman, 1980; Rist et al., 2002) and the results here support that earlier work.

The recent breakup of the Larsen Ice Shelf on the Antarctic peninsula provides an example of the instability of water filled surface crevasses (MacAyeal et al., In press).

It is hypothesized that local warming resulted in extensive meltwater production, causing surface crevasses to fill with water. Back stresses that may have been present, including those due to pack ice that is commonplace in the Weddell Sea, were not sufficient in preventing the catastrophic breakup of the ice. The pack ice has always been present in the area, but the localized warming and resulting pooled water are seen to be new factors that caused the ice shelf to destabilize and disintegrate.

4.7 Constant Parameters With Depth

The previous analysis utilized parameters that were dependent on depth in the ice (namely B, which depends on temperature $T(z)$, and ice density ρ_i, which has z-dependence given by Eq. 4.13). The situation where these values are constant with depth is shown here for comparison. In this case Eqs. (4.5) and (4.7) simplify to

$$\sigma_{xx} = \frac{1}{2}\rho_i g H \left(1 - \frac{\rho_i}{\rho_w}\right) - \rho_i g z \tag{4.14}$$

and

$$\sigma_{xx} = \frac{1}{2}\rho_i g H \left(1 - \frac{\rho_i}{\rho_w}\right) - \sigma_{\text{back}} - \rho_i g z \tag{4.15}$$

Results using $\rho_i = 917\,\text{kg/m}^3$, $\rho_w = 1030\,\text{kg/m}^3$, and $H = 500\,\text{m}$ are shown in Figures 4.9 and 4.10. Figures 4.10(a) & (b) show that the critical back stress needs to be higher when constant values for the density and temperature are used. It is not entirely clear why this should be the case. One notable difference between the stresses in Figure 4.9 is the flotation height of the ice in each case. The constant density solution results in a flotation height $h \approx 54\,\text{m}$ while $h \approx 71\,\text{m}$ for the parameterized density. The non-linearity of the true stress is also clear in this picture and this no doubt influences the stress intensity factor to a great degree.

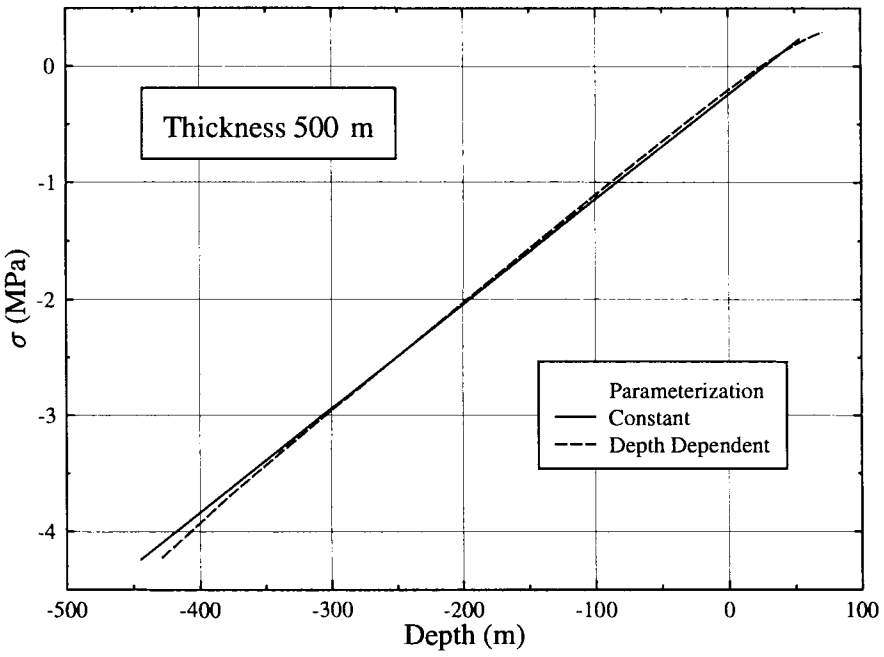

Figure 4.9: Comparison of the stresses in floating ice of thickness 500 m for depth dependent and constant parameters. In this picture, positive stress values indicate tension.

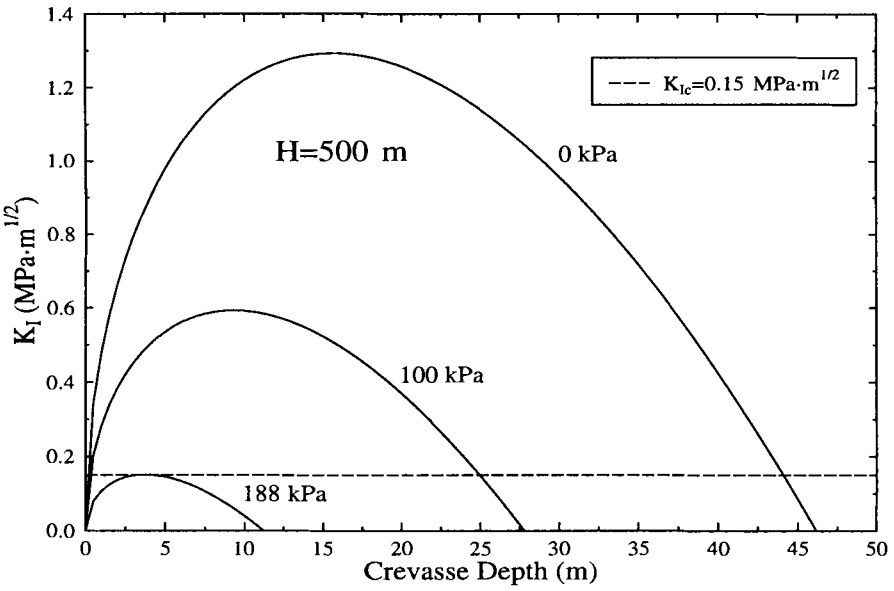

(a)

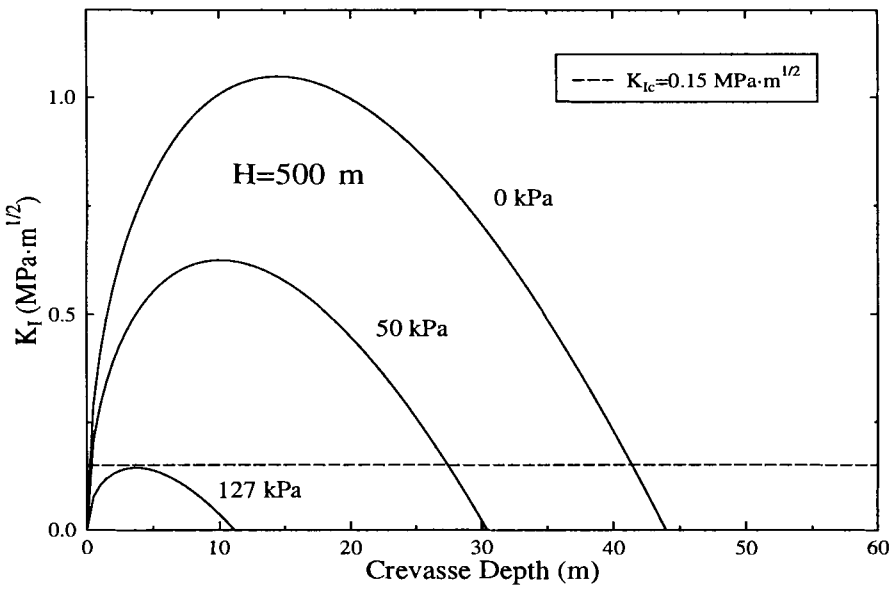

(b)

Figure 4.10: Comparison of stress intensity factors for depth dependent and constant parameters. Stress intensity factors are shown with the critical back stress necessary to retard unstable fracture for **(a)** constant parameters and **(b)** depth dependent parameters.

4.8 Crevasse Initiation

The subject of crevasse initiation is also speculative. How a new crevasse forms in glacial ice is unclear, but some possibilities may include the effects of bed conditions for grounded ice or tidal flexure at a grounding line (Lingle et al., 1981). In particular, crevasses formed at grounding lines can have their growth stifled if, as in the case of Byrd Glacier, the flow is compressive at some point downstream along the flowline and then becomes extending farther downstream.

The direction of crack propagation has been discussed using the strain energy density concept (Sih, 1991). The first hypothesis of this concept states that "crack initiation will start in a radial direction along which the strain energy density is a minimum" (Sih, 1991, pg. 8). The strain energy density is given by

$$S = a_{11}k_1^2 + 2a_{12}k_1k_2 + a_{22}k_2^2 + a_{33}k_3^2 \tag{4.16}$$

where the a_{ij} are functions of the angle θ from the crack tip to the infinitesimal volume element being analyzed, Poisson's ratio ν, and the shear modulus of elasticity μ. The k_i represent normalized stress intensity factors for mode I, II, and III cracks. In the case of mode I fracture, Eq. 4.16 takes the form

$$S = \frac{\sigma^2 a}{16\mu}\left[(3 - 4\nu - \cos\theta)\,(1 + \cos\theta)\right] \tag{4.17}$$

where $k_1 = \sigma a^{1/2}$ and $k_2 = k_3 = 0$. In order to find the minimum of Eq. 4.17, the derivative with respect to θ is taken and set equal to zero. This yields solutions

$$\begin{aligned} \theta &= 0 \\ \cos\theta &= 1 - 2\nu \end{aligned}$$

Equation (4.17) and its derivative are seen in Figure 4.11. Inserting these values into the second derivative of S determines whether the value is a maximum or minimum. Using this criteria, $\theta = 0$ is found to be a minimum. Coupled with the hypothesis

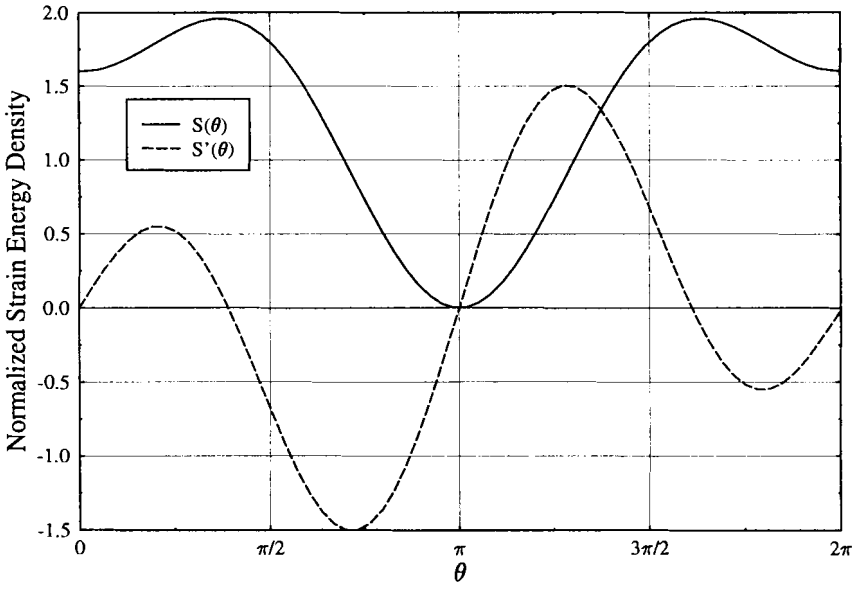

Figure 4.11: Normalized strain energy density $S(\theta)$ and derivative $S'(\theta)$ using $\nu = 0.3$ for ice.

presented above, this indicates that cracks will grow in a direction along the axis of the initial crack, perpendicular to the applied stress.

To determine the actual size of a "starter" crevasse, an examination of the stress intensity factor functions is necessary. Figure 4.5 shows that the general shape of the stress intensity factor vs. crevasse depth is convex. This means that the SIF curve will intercept the fracture toughness curve at two locations. The point where the SIF intercepts K_{Ic} for the second time has already been discussed and allows one to calculate the maximum depth to which a crevasse will penetrate. Points along the SIF curve where its magnitude is greater than the toughness are unstable, so it is valuable to know what minimum crack length is required to pass into this region of instability. The minimum crack depth $a_{\min}$ for a given back stress is determined by solving $K = K_{Ic}$ for the first intersection point (see Fig. 2.8). Once a crack obtains this minimum depth, the magnitude of the SIF function will be greater than the

fracture toughness and the crack can propagate to its maximum depth $a_{\max}$. The minimum crevasse depths required for unstable growth are shown in Figure 4.12. Because of the semi-convex nature of the SIF function, as the back stress increases, the values of $a_{\min}$ also increase. Therefore, the deepest initial crevasse that can form will be the one that results when the back stress is just below its critical value σ_{crit}. This crevasse, symbolized by a_0, will be the maximum initial crevasse that can form, since values of the back stress much less than σ_{crit} will result in shallower starter crevasses (see Fig. 4.5 for an illustration). Explicitly, a_0 can be determined by solving

$$K(a_0; H, \sigma^-_{\text{crit}}) = K_{Ic}$$

for some ice thickness H and some back stress σ^-_{crit} that is slightly less than σ_{crit}, as calculated in §4.6. The range of starter crevasse depths $a_{\min}$ for $\sigma_{\text{back}} \leq \sigma^-_{\text{crit}}$ in a given ice thickness H will then be

$$0 < a_{\min} \leq a_0.$$

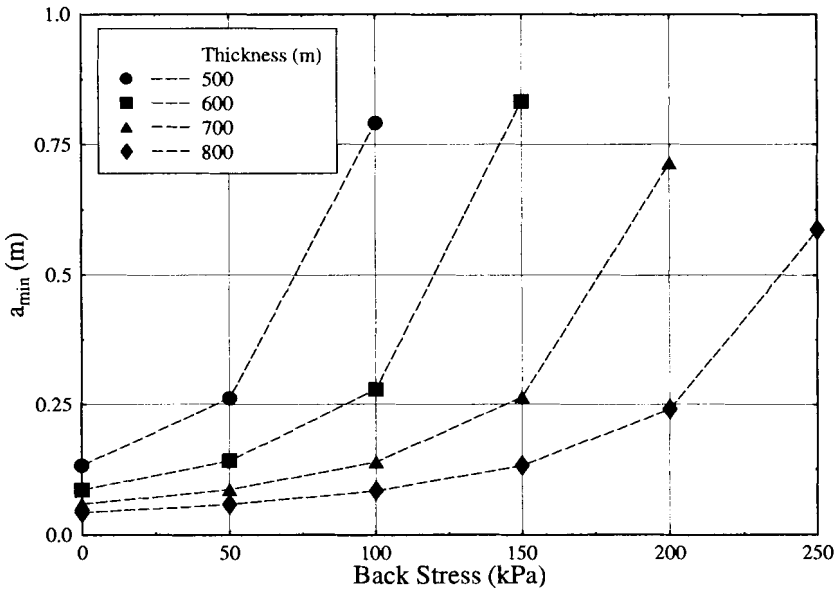

Figure 4.12: Minimum crack depths required to achieve unstable crack growth for a range of ice thicknesses.

4.9 Discussion

The results of this chapter are impressive. The combination of fracture mechanics and crevasse depth data allows for a powerful tool in the calculation of back stresses in floating ice. The back stress, like any stress, cannot be measured; it can only be inferred by the measurements of related quantities like strain rate. This requires multiple trips to locations in the field where strain networks can be assembled and the resulting data recorded. Theoretical stress calculations must be made and then rectified with the data. The back stress is then included *a posteriori* to match what is observed. The procedure that was shown in this chapter relies only on crevasse depth and ice thicknesses, both of which can be determined by remote sensing techniques, eliminating the need for expensive and possibly dangerous field excursions.

The results that were determined for the back stress on Byrd Glacier are based on assumed crevasse data. The calculations do match well with the data presented in Thomas and MacAyeal (1982), which were calculated in the manner described in the previous paragraph, for the western portion of the Ross Ice Shelf. The results presented here help to fill in a gap that is present in that dataset for the eastern portion of the ice shelf. Maximum and minimum crevasse depths were also derived based on ice thickness and applied stress. These results should be compared with those of §2.4.1. The analysis of this chapter uses a more accurate representation of stress with depth and it is seen that this greatly influences allowed crevasse depths.

Since back stresses cannot be ascertained directly, only inferred from other measured quantities, having a model which employs a fracture mechanics analysis and allows for theoretical predictions of back stress based on real or assumed crevasse data is most valuable.

CHAPTER 5

LARGE SCALE ICEBERG FORMATION

5.1 Background

Studies of crevassing in glacial ice invariably lead to the examination of the processes that result in calving, whether it be small scale slab calving or large scale tabular iceberg formation. A detailed examination of slab calving has been covered in both Hughes and Nakagawa (1989) and Hughes (2002), where the controlling process was thin (on the order of meters) ice bending along shear planes and collapsing in place (Fig. 5.1), similar to a building being razed by dynamiting the foundation from underneath. The impetus for a model of this type was observation of calving ice walls on Deception Island, where the ratio of slab height h to depth c was around 3 (see Hughes, 1998, pgs. 218–221). Clearly, this model will not explain larger iceberg formation, where bending mechanisms are not applicable and the ratio of height to thickness (length) is much smaller.

To undertake a study of tabular icebergs (those icebergs with the infamous "area comparable to that of Rhode Island" tag) calved from ice shelves, it is necessary to consider the processes that occur much farther upstream, at the points where the ice first crosses the grounding line and enters the ice shelf, or at locations where the strains that exist in the ice are at their highest. Crevasses formed by mechanisms at these locations are assumed to be the controlling factor in the formation of large icebergs once they reach points closer to the ice front.

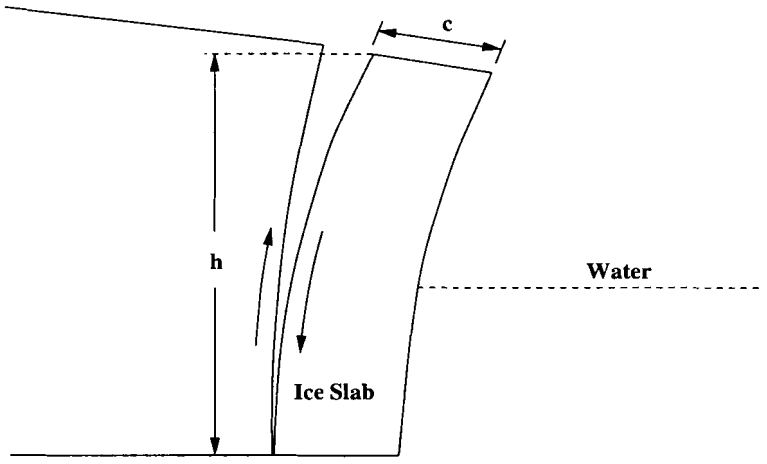

Figure 5.1: Illustration of slab calving. The slab has dimensions of height h, depth c, and the arrows represent shear acting along shear planes in the ice.

5.2 Strains in Floating Ice

When ice becomes afloat, the longitudinal strain rate induced by stresses in a 2-D ice shelf can be written as (Thomas, 1973a)

$$\dot{\varepsilon}_{xx} = \left[\frac{\rho_i g H}{4A}\left(1 - \frac{\rho_i}{\rho_w}\right) - \frac{\sigma_c}{2A}\right]^3 \tag{5.1}$$

where H is the total thickness of the ice, A is the ice hardness parameter and σ_c is the contribution due to a compressive back stress in the ice. Contained within this expression is the overall longitudinal deviator stress

$$\sigma_{xx} = \frac{1}{4}\rho_i g H\left(1 - \frac{\rho_i}{\rho_w}\right) - \frac{1}{2}\sigma_c \tag{5.2}$$

which is also sometimes written as $\sigma_T - \sigma_B$, or the difference between tensile pulling stress and overall back stress. Using these two equations, it can be shown that under certain assumptions regarding the behavior of crevasse growth and crevasse spacing, strain considerations alone are not sufficient to create crevasses that are separated by a great enough distance to form large icebergs.

The additional assumption needed is that the ratio of crevasse width w to spacing s is constant as the crevasse migrates downstream, i.e.

$$\frac{w_i}{s_i} = \frac{w_f}{s_f} \tag{5.3}$$

where subscript i and f refer to initial and final conditions. Initial crevasse widths have been determined earlier using the Weertman dislocation theory approach (see §2.10.2 and §2.10.3). In this model newly formed crevasses are only on the order of millimeters, at their widest, at the surface. The initial spacing of newly formed crevasses was also given by Weertman (1977) as

$$s_{\min} = \frac{3}{2}\left(\frac{K_c}{\sigma_{xx}}\right)^2 \tag{5.4}$$

where $s_{\min}$ denotes the minimum spacing required to have any crevasse growth in ice with fracture toughness K_c. This equation is a simplification of a relation describing crevasse spacing as a function of crevasse depth a. The functional relation $a(s)$ can be written as (Weertman, 1977, pg. 41, Eq. 41)

$$a(s) = \frac{1}{\rho_i(z)g}\left[\sigma_{xx} - K_c\left(\frac{2}{\pi s}\right)^{1/2}\left(\frac{2\pi}{\pi+1}\right)\right] \tag{5.5}$$

Solving Eq. 5.5 for s as a function of crevasse depth a results in

$$\begin{aligned} s(a) &= \frac{8\pi}{(\pi+1)^2}\left(\frac{K_c}{\sigma_{xx} - a\rho_i(a)g}\right)^2 \\ &\approx \frac{3}{2}\left(\frac{K_c}{\sigma_{xx} - a\rho_i(a)g}\right)^2 \end{aligned} \tag{5.6}$$

where the density is also now a function of crevasse depth. Equation (5.6) is plotted in Figure 5.2 for three values of longitudinal deviator stress σ_{xx}. In order to get the final spacing s_f the final width of the crevasse is needed. This can be found by calculating the strain rate in the ice using Eq. 5.1 and applying it appropriately to the initial crevasse width.

Strain rates on the Ross Ice Shelf can be calculated through the use of data presented in Thomas and MacAyeal (1982) and Bentley and Jezek (1981). Data were

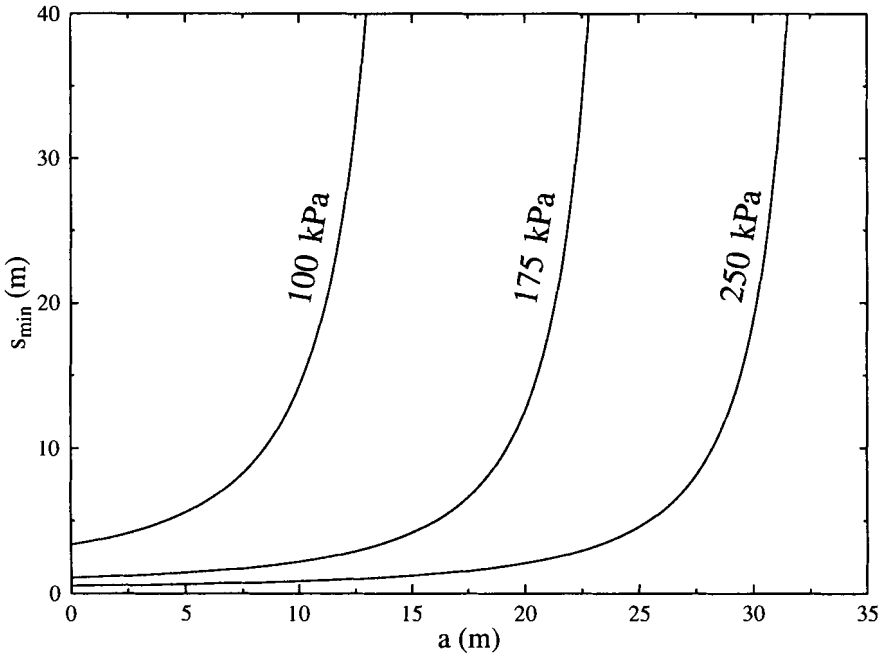

Figure 5.2: Minimum spacing necessary to allow crevasse growth. Spacings for three values of the longitudinal stress σ_{xx} are shown.

collected for the flowband that originates at Byrd Glacier and travels towards the ice front (Table 5.1). Using these data, strain rates were calculated at three locations using Eq. 5.1. The results of that calculation can be seen in Figure 5.3. The largest strain rate is found at the location nearest the fjord entrance, 50 km downstream. Assuming a constant velocity of 750 $^{m}/_{yr}$ (see Appendix A), it takes the ice exiting the fjord approximately 67 years to reach this point. Using this time, the strain rate can be converted to a strain by the simple relation

$$\varepsilon_{xx} = \dot{\varepsilon}_{xx}\Delta t$$

When this strain is applied to an initial crevasse width of 1 millimeter the final width at the ice margin is *at most* only twice the initial width, since strains farther downstream are very small and contribute negligibly to widening. Clearly this result is not an accurate description of how crevasses behave, since widths on the order of

Distance from fjord entrance (km)	Ice thickness (m)	Retarding force per unit width of flowband ($^{MN}/_{m}$)	Calculated back stress (kPa)	Ice hardness parameter (10^7 Pa·s$^{1/3}$)
50	600	50	83	15
175	400	45	112	17
350	300	10	33	19

Table 5.1: Ross Ice Shelf data. Ice thickness is taken from Bentley and Jezek (1981) while retarding force and ice hardness parameter are taken from Thomas and MacAyeal (1982).

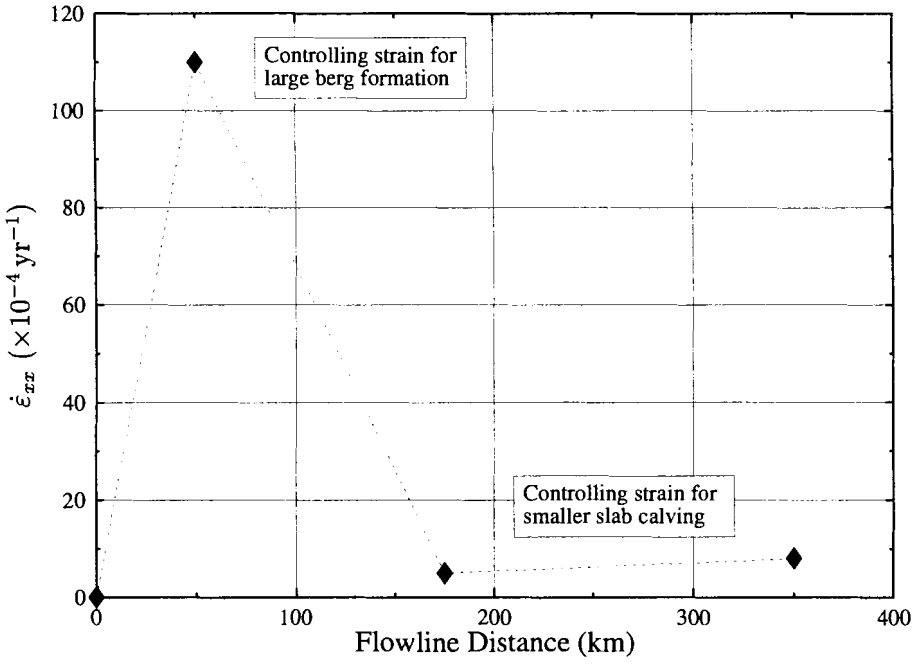

Figure 5.3: Calculated strain rates along the Byrd Glacier flowband on the Ross Ice Shelf. Larger strain rates farther upstream may be the controlling mechanism for large scale iceberg formation, while smaller strains nearer the calving front may control the smaller and more frequent calving events.

meters have been observed. This also would result in final crevasse spacings that are only double the initial spacing, at most, which itself is on the order of tens of meters. This exercise does not result in anything near a tabular sized spacing between successive crevasses, so it may be assumed that stretching due to a straightforward calculation of the strain is insufficient.

5.3 A New Assumption

Simply allowing for a pair of consecutive crevasses to spread under the influence of ice shelf strain alone is insufficient for producing large crevasse spacings. A new assumption and model formulation is presented in this section. This model makes use of a random distribution of crevasse depths and then utilizes a factor that will allow or prohibit crevasses to grow and contribute to iceberg formation.

5.3.1 Enhancement Factors and Observation

A model described in Chapter 3 allowed for crack widening as the crack penetrated more deeply into the material. This is the mechanism considered now so that crevasse width w can be related to depth a by a relation of the form

$$w = f(a)a \tag{5.7}$$

where $f(a)$ is an enhancement factor that is dependent on depth. Emphasis here is not on the actual form of $f(a)$, but rather on observations that support the hypothesis that widths are not simply driven by strains in the ice. When a crevasse forms due to local conditions favoring crevasse initiation, back stresses and other effects will prevent it from penetrating to its maximum allowed depth. Instead it is likely to grow in spurts as local conditions change during its journey downstream (see Fig. 5.4). This new effect of widening as a function of depth provides greater opening widths, resulting in greater spacings downstream.

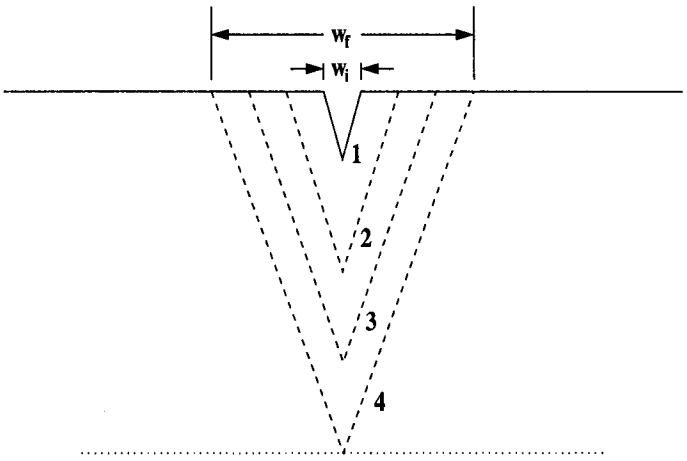

Figure 5.4: Illustration of crevasse widening as depth increases. The depth grows in steps from situation 1 to 4. The latter represents its maximum penetration depth as determined by fracture mechanics. The crevasse widens from w_i to w_f during the time it is penetrating into the ice.

Consider the data in Table 5.1 for the 50 km location. This is where the largest strains occur; thus it can be inferred that crevasses will form here and that they may be the controlling factors in large iceberg formation. (See also the left-hand panel of Figure 6 in Kenneally and Hughes (2002) which is appropriate for crevassed ice that is floating or resting on a low friction bed.) The calculated back stress at 50 km is 83 kPa and the ice is 600 m thick. Earlier calculations showed that crevasse penetration depth could be determined for various back stresses. With a back stress of 83 kPa, a maximum crevasse depth, $a_{\max}$, of approximately 30 m results. If this value of $a_{\max}$ is inserted into Eq. 5.6 with a density relation again given by

$$\rho_i(z) = \rho_i - (\rho_i - \rho_s)\, e^{-z/c}$$

the initial spacing necessary to allow for crack growth is found to be $s_i \approx 20\,\text{m}$. If it is now assumed that the final crevasses are meters in width (pers. comm. Hughes; Swithinbank, 1999) while the initial ones are millimeters in width, Eq. 5.3 yields a

final spacing of

$$\begin{aligned} s_f &= s_i \frac{w_f}{w_i} \\ &\approx 10^3 s_i \end{aligned} \tag{5.8}$$

These values of the final spacing are certainly large enough to result in the tabular icebergs that are of such interest. The relation in Eq. 5.8 is plotted in Figure 5.5 for two values at the lower end of observed final widths w_f. Initial width in each case is taken to be only 1 mm. This result implies there may be a need for some type of "un"-enhancement factor to limit the spacing

$$s_f = g(p_j) s_i \frac{w_f}{w_i} \tag{5.9}$$

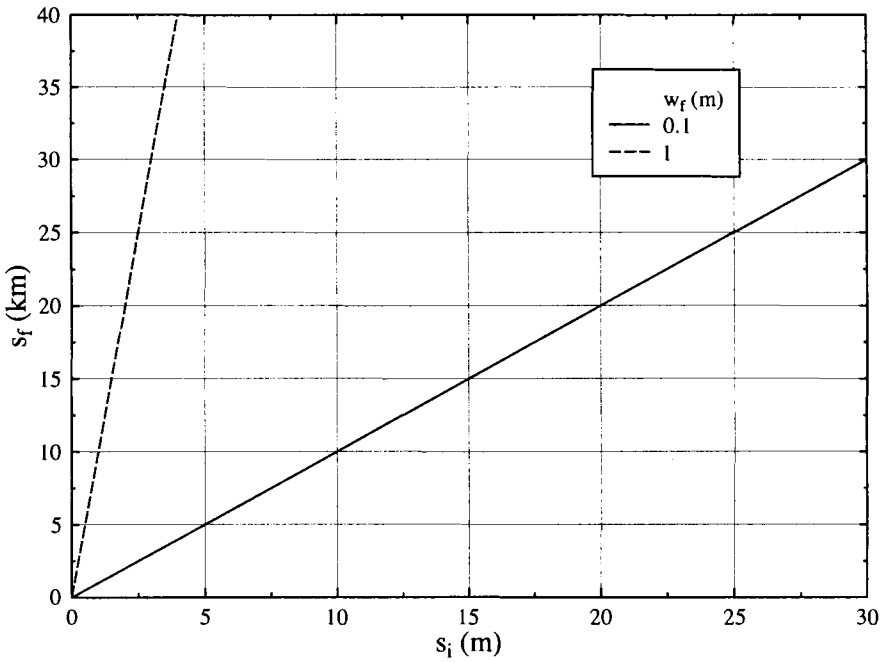

Figure 5.5: Final crevasse spacing under the current analysis. Two values for final crevasse width, w_f, result in spacings on the order of the largest observed tabular icebergs.

where $g(p_j)$ can be a function of the relevant parameters p_j used to describe the problem. One specific p_j could be included to model healing of crevasses by refilling with snow and low density firn. This parameter would probably be dependent on crevasse depth and location, healing the shallower crevasses in high accumulation areas while allowing deeper crevasses to continue their growth regardless of their location. Another parameter could be a probabilistic factor, determined by observation, that dictates how often icebergs of a certain size are allowed to form. For instance, if the largest tabular icebergs are observed to form with a frequency T_o, then $p(T_o)$ would represent a crevasse pair that propagated entirely through the ice with a spacing that results in the necessary dimensions in the required time, keeping all intermediate crevasses at shallower depths. These intermediate crevasses would then be responsible for smaller scale events closer to the ice front.

5.3.2 Stochastic Modeling

In order to utilize the mechanism discussed in the previous section, a model that includes a stochastic distribution of crevasse depths is considered. At a location far upstream from the ice front, a function $r(x_i)$ is used to create crevasses with a random distribution of depths throughout some length, Δx, of the ice flow where crevasses are known to form. Crevasse depths and spacings would be dictated by the fracture mechanics arguments shown earlier. Localized values of back stress would result in crevasse depths less than the maximum allowed value in some areas, and this could be explicitly included in the randomizing function by making it dependent on location and stress. This would then result in one possible functional relationship $r(x, \sigma_{\text{back}})$. Crevasses that are found to be the deepest initially could then be "chosen" to be those that evolve into releasing tabular icebergs. The random placement of crevasses would then be modified by the factor $g(p_j)$, healing some crevasses and allowing others to

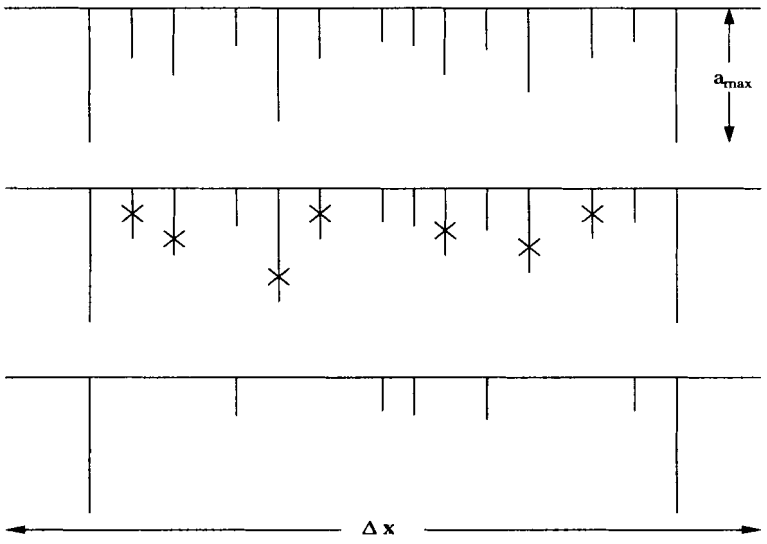

Figure 5.6: Illustration of randomly created crevasses which are chosen to contribute to iceberg formation. **Top**: Crevasses will be created in some longitudinal distance Δx by a modeled stochastic process. **Middle**: The factor $g(p_j)$ will "pick out" crevasses, shown with the $\times$, that will not be allowed to continue their growth. **Bottom**: The remaining crevasses grow, with the deepest crevasse pairs contributing to tabular iceberg formation, and the shallower crevasses resulting in smaller scale iceberg and slab calving events at the ice front.

grow based on empirical data and other requirements of the model. An illustration of this behavior is shown in Figure 5.6.

This model should be compared with Figure 5.7, which is similar to the figure mentioned earlier from Kenneally and Hughes (2002). Figure 5.7 shows crevasses forming at regular intervals on a wet, slippery bed, which would result in a nearly constant strain rate. The crevasses that form earliest are allowed to penetrate the deepest in a given amount of time, while all others lag behind. Thus, the crevasses that form first will dictate iceberg dimensions. The model illustrated in Figure 5.6 is similar in concept except that the distribution is random, and some crevasses are excluded entirely, through arguments given earlier, and this leads to crevasse pairs that dictate iceberg size.

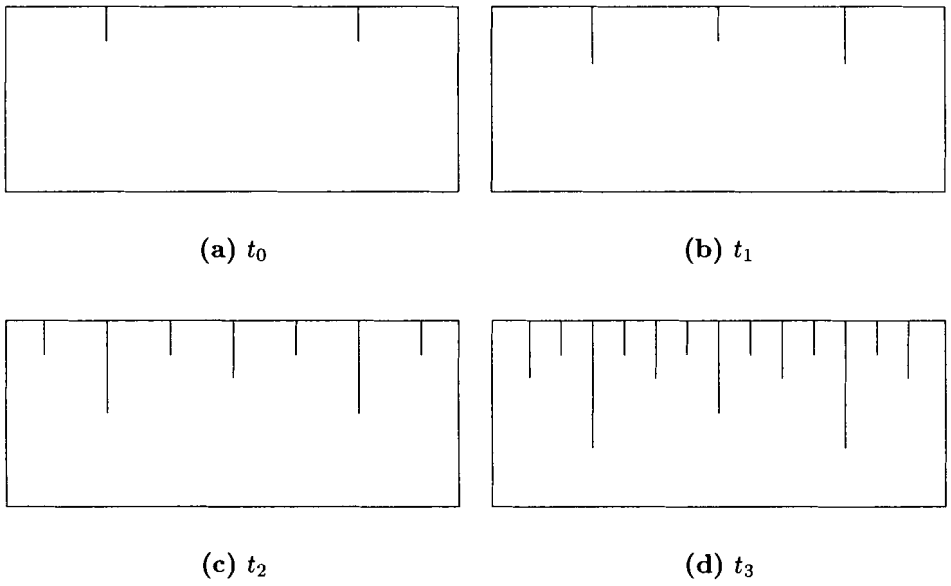

Figure 5.7: Modeled crevasse growth for ice on a very low friction bed. Ice on a low friction bed is subjected to a nearly constant strain rate, resulting in crevasses that open at equal rates. During a given time interval Δt, crevasses that first form, shown in (**a**), will penetrate deeper into the ice as other crevasses nucleate and grow, shown in (**b**)–(**c**).

5.4 Discussion

Any discussion that attempts to explicitly determine a relation describing calving processes from a theoretical standpoint is a precarious venture. There are many factors that can influence the outcome, resulting in a certain degree of "looseness" when adjusting the parameters. Thus one is able to attain any results desired. The solid foundations laid out in the work of other authors and in the earlier work of this thesis can be rendered almost useless if too much leniency is allowed when trying to apply those results to such a speculative process as calving. However, it is not an absolute or ironclad result that is desired here. Instead, it is important to merely demonstrate that the physics can be applied in such a manner that is not entirely inconsistent with reality, and that it resolves itself into a meaningful and realizable solution.

Finally, the idea of modeling crevasse depths and spacings as a random process with rules derived from sound physical arguments is presented as another avenue of exploration. The work thus far has demonstrated that attempting to determine hard and fast rules for iceberg formation is difficult at best. Random distributions of crevasses in a crevasse field, with depths and spacings governed by fracture mechanics results, along with a mathematical model that chooses crevasses to grow based on observed data and modeling needs, permits one to loosen the physical requirements in favor of a parameterized solution. This model could be a valuable first order approximation in large scale modeling of calving events.

CHAPTER 6

CONCLUSION

6.1 Overview

A detailed analysis of crevassing and calving is a difficult task, as the work to this point has demonstrated. Given the dangers in collecting real field evidence, and the complexities in mathematically modeling the processes responsible, progress in this branch of glaciology has been slow. This final section will present arguments for the validity of the work presented, as well as future paths to be explored by any glaciologists brave enough to do so.

6.2 Validity of Work

The approximations covered in this thesis do compare well with previous results referenced throughout the work. The crevasse depths calculated in Chapter 2 are based on the same approach as van der Veen (1998a,b) so they agree well with the added condition that the solution is only valid for thicker ice ($H \geq 1000\,\mathrm{m}$). The ad-hoc spacing criteria derived seems to be qualitatively correct, but there is no real proof to back this result. Limitations, presented in terms of the extent of the plastic zone, on the use of linear elastic fracture mechanics also provide a guide as to whether or not fracture mechanics can be considered valid. In the case of thick ice and a von Mises yield criteria, LEFM seems to be a valid and reliable approach.

The model in Chapter 3 is presented as a stimulus for further exploration. The power law creep crack growth rate equation derived provides realistic results for the

time scales involved in fracture of a material experiencing creep, but again, this is a difficult result to verify by measured field quantities.

Back stresses calculated in Chapter 4 are representative of previously calculated quantities (Rist et al., 2002), although there is no reason to believe that they should be greatly different since the analysis that was employed is the same. The greatest difference in calculation would probably arise only in the use of a temperature profile specific to the location under consideration. When the theoretical calculations are compared to those values presented in Thomas and MacAyeal (1982), the agreement is more impressive. The calculations done by Thomas and MacAyeal were based on real field data, with the calculated "retarding force" being that force which was necessary to rectify differences in measured and calculated strains on the Ross Ice Shelf. The procedure used was not the same as the one presented in Chapter 4, where linear elastic fracture mechanics was employed, yet the results are comparable in magnitude. The calculations in this thesis for the eastern portion of the ice shelf also help to fill in a gap that exists in the original work (see Thomas and MacAyeal, 1982, pg. 409, Fig. 8).

Like Chapter 3, the ideas presented in Chapter 5 are meant mainly as an impetus to further discussion on the topic of large iceberg formation. The slab calving mechanism discussed in the chapter does a good job of explaining the mechanics of the smaller ice slabs that peel away from ice fronts. However, there is still no reliable mechanism that can explain the extremely large icebergs that less frequently form. These icebergs are in all likelihood controlled by processes that take place far upstream, where crevasses have the most time to penetrate and laterally spread apart. It is hoped that the concepts presented in this chapter will encourage more analysis of the processes that lead to crevasse formation upstream, resulting in large scale phenomena at the ice front. The stochastic model discussed could be a valuable

first order approximation for modelers, since the scale of the problem is not necessary (see §6.4.3); only the final results that determine when calving events take place and the dimension of the resulting iceberg are required.

Overall, the solutions presented are for the most part only first order. Shear stresses were neglected as well as transverse spreading of the ice. Most discussions of calving follow this same approach. Greater sophistication in computing and programming techniques will hopefully allow for second order solutions to become the norm. An example of a possible second order correction is presented in §6.4.1.

6.3 Shortcomings

There are always shortcomings in any work that tries to predict the behavior of glacial ice. Numerous approximations are made when dealing with systems that are as large as modern day and paleo ice sheets. Over the domain where these approximations are made, the sheer scale of the system will usually minimize any error that may arise. The results determined in this work also involve many smaller scale approximations. In Chapter 4, solving a complex temperature model was eschewed in favor of using a simpler parameterization. Ice density functions were taken to be continuous exponential functions, and the parameters used were based on earlier work. The calculation of back stress for the floating portion of Byrd Glacier was done for width-averaged values of thickness and velocity, rather than those appropriate for a single flowline. The effects of side shears would surely have some impact on a calculation done for ice in a fjord. The basal melting calculation presented in Appendix A is also width-averaged. These calculations do, however, result in values that agree with earlier work and thus can act as a springboard for those who decide to undertake the problem in the future.

The two areas where some real liberties are taken with the problem are the sections dealing with the creep fracture process in Chapter 3 and the large iceberg formation

in Chapter 5. The analysis involving creep fracture ignored air filled surface crevasses, where the effects of ice overburden would negate the use of the derived model, but the model may still be viable for basal crevasses where hydrostatic pressure arising from water filling the crevasse will be greater than the ice overburden, at least until the crevasse penetrates to sea level. The analysis does show that a creep fracture process will allow for slower formation of crevasses, with times that are appropriate to the time scales of glacial processes. This process may be more appropriately used in a discussion of the lateral opening of crevasses. This could then be used to determine when crevasses will meet up with localized margins of weakness, such as the boundary where adjoining ice streams meet to form a larger stream, or other proposed "weak underbellys." An analysis of this type could be used to predict the maximum lateral extent to which icebergs will form, as well as the time it would take for this process to occur.

The theory put forth in Chapter 5 is speculative, but it is still based on physically realizable parameters and processes. It is hoped that a presentation of this kind results in further discussion. Since the problem is infrequently addressed, some kind of answer would be valuable, both on a scientific level, where reliable iceberg predictions would be quite a coup, and on a more practical, human level, where these prediction may aid in preventing disasters incurred during a monster iceberg's journey through the oceans.

6.4 The Future

The history of fracture and its effects on calving is short, even in the relatively young field of glaciology. A broad groundwork has been laid out, but there are many more avenues of investigation open to the intrepid explorer. (Field work involving fractured ice isn't the only dangerous undertaking when studying calving.) With this short

history comes a long future. Presented here are some issues that can and should be addressed by the next generation of researchers interested in this problem.

6.4.1 Mixed-Mode Cracking

The entirety of this thesis, and almost all previous work that explored the subject of fracture mechanics in glaciology, dealt with a single mode of cracking, namely mode I cracking, or tensile opening (see Figure 2.2). Proceeding in this way is proper for crevassed ice that is only subject to stresses that are perpendicular to the crevasse walls, which is a good approximation for floating ice where the stresses are longitudinal extending stress coupled with the resistive ice overburden and hydrostatic stresses. Thus, very wide expanses of floating ice can be examined by a mode I cracking analysis, since it can be assumed that side shear stresses have minimal effect when the shear margins are located far from a central flowline under consideration. If crevassing is examined in narrow fjords or on grounded ice, typical to valley glaciers as well as the fast moving ice streams of the large ice sheets, then the stresses applied would no longer be purely tensile (Fig. 6.1) and some combination of the remaining modes of cracking would need to be considered for a more thorough and proper

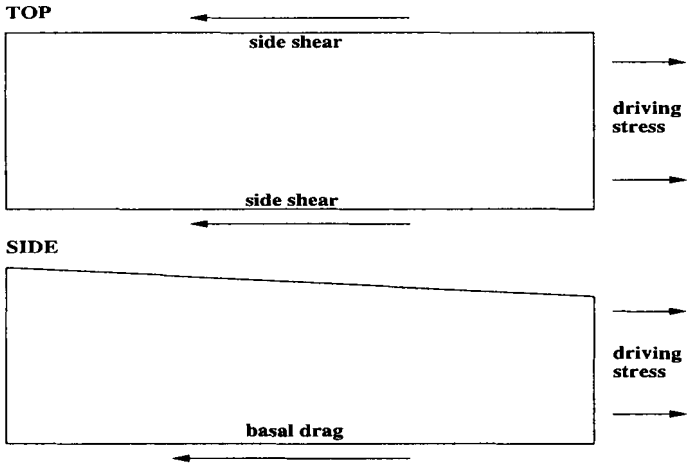

Figure 6.1: Top and side view of ice subjected to side and basal shear stresses as well as a longitudinal driving stress.

treatment. Mixed mode cracking may explain the crevasses that are observed to exist, specifically the crescent shape that crevasses tend to display as they penetrate the ice. The crescent shape of crevasses has been noted before, both in the field (pers. comm., Mikhail Grosswald, Russian Academy of Sciences) and in mathematical models (see Iken, 1977, pgs. 599–601), a model which should be noted does not make specific use of fracture mechanics. To solve the problem of mixed mode cracking, the system is rotated to its principal axes coordinate system, where only the principal stresses remain. In doing this, the geometry of the system is changed, and cracks may not necessarily propagate straight down from the surface. While mixed-mode cracking may be a second order effect, it needs to be considered if a truly accurate representation is desired.

6.4.2 Sub-critical Crack Growth

In any discussion of calving processes, the question most often heard is, "What is the impetus behind a calving event?" A superficial answer is obviously that the ice had completely cracked through and was released when it approached the terminus, whether that terminus is on a valley glacier or marine ice shelf. This answer doesn't get at the true heart of the matter. Why did the crevasse form in the first place? Were the conditions necessary for this crevassing contained in the ice itself, or in the overall environment? If the external environment is responsible, how does the climate influence the ice and when it initially fractures? Before the advent of more sophisticated measuring devices, most calving studies dealt with glaciers from afar. Measurements were made of the ice front position as well as the overall speed of the glacier. If the front remained stationary, the calving rate was determined empirically to balance the glacier velocity. Similar conclusions could be drawn if the ice front advanced or retreated. There are few, if any, direct measurements of why the ice failed in the first place. It is hoped that this issue has at least been looked into at

some level within this thesis. It was mentioned in §4.8 that the subject of crevasse initiation is speculative, but that some avenues exist to be explored. One such avenue is mentioned here, with the hope that in time the methods and data will exist to allow an in-depth analysis.

In the case of ice flowing across a grounding line and continuing into a marine ice shelf, there are effects that arise from tidal flexure in the grounding zone. As the tides cyclically rise and fall, the ice is subjected to a cyclic stress due to bending, with the ice at the grounding line, or within the grounding zone, acting as a hinge. Crevasse initiation could be influenced by this flexure, which may stress the ice to such an extent as to exceed its fracture toughness. Deep and dangerous crevasses are usually found some distance downstream rather than in an area near the grounding line. It is possible that the cracks formed as a result of this tidal flexure are kept in reserve under the influences of back stresses, perhaps until they are reactivated at some point downstream where the back stress is less, where they are then free to continue their growth through the ice, influencing the formation of medium to large scale icebergs.

A sub-critical crack is a crack whose associated stress intensity factor does not have a magnitude that exceeds the fracture toughness of the material. The critical and sub-critical regimes are illustrated in Figure 2.8. In the sub-critical region, unstable crack growth will not occur, but experience has shown that materials that are not stressed past their ultimate strength will still fail. This situation is most notable in the airline industry, where the stresses induced during takeoff, landing and normal flight conditions tend to stress the plane's structure in a periodic manner. There have been studies done on the influence of cyclically applied stresses on sub-critical crack growth (Paris et al., 1961; Paris and Erdogan, 1963) to see what, if any, relation could be determined. When a material is subjected to a cyclically applied stress with extreme values σ_1 and σ_2, a difference $\Delta\sigma = \sigma_2 - \sigma_1$ arises; thus there is an associated range in the stress intensity factor $\Delta K = K_2 - K_1$. For a given number of cycles

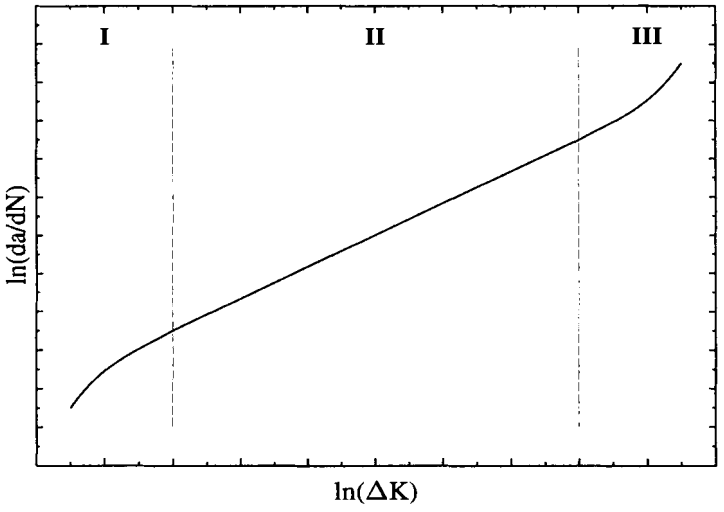

Figure 6.2: Illustration demonstrating the experimental results of crack growth per cycle as a function of a cyclicly applied stress. Actual experimental data plots can be seen in Paris et al. (1972) or Kanninen and Popelar (1985, pg. 500)

N, a pre-existing sub-critical crack will grow some length $\mathrm{d}a$. When a log-log plot comparing $\mathrm{d}a/\,\mathrm{d}N$ to ΔK is examined, there are three distinct regions of interest, shown in Figure 6.2. In regions **I** and **III** the relation is clearly non-linear. In region **II** the relation seems to be linear. With this assumption, one can write for region **II**

$$\begin{aligned} \ln\left(\frac{\mathrm{d}a}{\mathrm{d}N}\right) &= C' + n \ln \Delta K \\ &= \ln\left(C \Delta K^n\right) \end{aligned}$$

where C and n are constants that need to be experimentally determined. This is known as the Paris law. Further simplification results in the most common form of the Paris law,

$$\frac{\mathrm{d}a}{\mathrm{d}N} = C \Delta K^n \tag{6.1}$$

The Paris law allows one to determine the rate of crack growth per cycle for a given change in SIF over the cycle. (Recall that for the simplest case of a Griffith crack

$K = \sigma\sqrt{\pi a}$, so $\Delta K = \Delta\sigma\sqrt{\pi a}$.) One use for this law is to determine critical safety thresholds for cracks in various materials and to aid in scheduling maintenance inspections before these thresholds are passed. In the case of a floating ice shelf, the law could be used to quantify how a sub-critical crack behaves. As the ice rises and falls with the tides, the induced stresses at grounding lines and beyond will vary and can be calculated using some straightforward mechanics (e.g. Lingle et al., 1981). The problem in applying Eq. 6.1 arises with the constants C and n. Currently there are no satisfactory data that allow for an accurate determination of these constants (pers. comm., Peter Sammonds). Until accurate and trustworthy values for these constants are known, the idea of applying the Paris law to floating ice subject to tidal flexure will have to wait. The question of whether or not tidal flexure actually causes cracks in the ice can best be answered by another first person account, again given by Swithinbank (1999, pg. 124):

> "Camped in the gentle depression at the hinge line (grounding line) 32 kilometres south-east of Maudheim, we were kept awake through part of the night by loud reports from ice cracking every few seconds, presumably as a result of the falling tide. Our presumption was confirmed when we noted a periodicity in the cracking that corresponded with the tidal cycles."

The cyclic nature of the tides initiate cracks in ice and could also be responsible for their maturation through the sub-critical regime into the region where unstable growth can take place.

6.4.3 Fracture and Calving in Ice Sheet Models

Perhaps the biggest issue that arises when attempting to include calving processes in the large scale ice sheet models such as the University of Maine Ice Sheet Model (UMISM) is the problem of scaling the required input parameters. (An overview and application of UMISM can be found in Johnson (2002).) Continent sized ice sheet models are run on grids that are kilometers in scale, which itself is a result of

the maps that are produced describing bedrock topography and current ice surface elevations (Lythe and Vaughan, 2000). This lack of refinement has served modelers well though. The ice sheets that are produced are very accurate when they are tuned to correctly recreate field data and climate conditions. It is this very tuning that is a shortcoming when it comes to the inclusion of calving processes. Models are run and ice sheets advance or retreat, as dictated by calving effects, which are adjusted via the indeterminate "knob," which represents some adjustment of the relevant parameters until what is perceived as the correct solution, i.e the solution that correctly reproduces the observed geomorphology, is achieved. Because of the small scales in which fracture and crevasse growth mechanisms take place, it is very difficult to include them as physically based processes in models whose refinement is so relatively coarse. There are still many unanswered questions as to what these mechanisms may be, and which may be vital when included in ice sheet models coupled with a physically based calving mechanism.

6.5 What to Make of it All?

What does it all mean? Where does it all lead? How can it be of use in the future? These are all questions that should be addressed at the conclusion to any work of this type.

1. What does it all mean?

Perhaps the most important lesson to be taken away is that studying calving is *hard.* Although it was stated earlier that the field is still in its relative infancy, there have been many talented and intelligent individuals working on it for that brief period of time. Many valuable results have been gleaned from this small canon of work. Both analytical and numerical approaches have strengths and weaknesses, but as more work is done that can bring the two closer, the answers should become more plentiful. For the moment, truly reliable answers are somewhat few and far between.

2. Where does it all lead?

Soon enough, calving may be at the forefront of all glaciological studies, as a link between calving, the retreat of ice sheets, and rapid climate change is explored. It was stated in the introduction to this thesis that an increase in calving events may be a bellwether to greater climatological issues. Whether changes in the climate are man-made or naturally occurring, the climate is a hot-button issue these days. As a result, any pursuit that purports to have an answer, or at least a theory, as to how climate can change rapidly will move to the front of the line for the government funding trough.

3. How can it be of use in the future?

The choice was made for the work done in this thesis to focus on the analytical solutions that exist to describe crevassing and calving. This choice led to some approximations that were necessary so that a solution could be found. Eliminating these approximations, or including them to a lesser degree, may require more complex numerical solutions. The first order analytical solutions that were presented can be extended to more complex, second order systems where sophisticated computer modeling is necessary. The small steps that were taken here can hopefully be used as a jumping-off point for any future work.

REFERENCES

Alley, R. B. and D. R. MacAyeal, 1994. Ice-rafted debris associated with binge/purge oscillations of the Laurentide Ice Sheet. *Paleoceanography*, **9**(4), 503–511.

Barnby, J. T. and R. D. Nicholson, 1977. Local stress and strain during crack growth by steady state creep. *Journal of Materials Science*, **12**, 2099–2108.

Bentley, C. R. and K. C. Jezek, 1981. RISS, RISP and RIGGS: Post-IGY glaciological investigations of the Ross Ice Shelf in the U.S. programme. *Journal of the Royal Society of New Zealand*, **11**(4), 355–372.

Berry, J. P., 1960. Some Kinetic Considerations of the Griffith Criterion for Fracture. *Journal of the Mechanics and Physics of Solids*, **8**, 194–216.

Beyer, W. H., ed., 1991. *CRC Standard Mathematical Tables and Formulae*. CRC Press, Boston, second edn.

Brecher, H. H., 1982. Photographic determination of surface velocities and elevations on Byrd Glacier. *Antarctic Journal of the United States*, **17**(5), 79–81.

Broecker, W. S., 1994. Massive iceberg discharges as triggers for global climate change. *Nature*, **372**, 421–424.

Broecker, W. S. and G. H. Denton, 1989. The role of ocean-atmosphere reorganization in glacial cycles. *Geochimica et Cosmochimica Acta*, **53**(10), 2465–2501.

Broek, D., 1978. *Elementary Engineering Fracture Mechanics*. Sitjoff & Noordhoff, Alphen aan den Rijn.

Broek, D., 1988. *The Practical Use of Fracture Mechanics*. Kluwer Academic Publishers, Boston.

Brown, C. S., M. F. Meier and A. Post, 1982. Calving speed of Alaska tidewater glaciers, with application to Columbia Glacier. *U.S. Geological Survey Professional Paper*, 1258–C.

Calov, R., A. Ganopolski, V. Petoukhov and M. Claussen, 2002. Large-scale instabilities of the Laurentide ice sheet simulated in a fully coupled climate-system model. *Geophysical Research Letters*, **29**(24), **69**–1–4.

Dulaney, E. N. and W. F. Brace, 1960. Velocity Behavior of a Growing Crack. *Journal of Applied Physics*, **31**, 2233–2236.

Epprecht, W., 1987. A major calving event of Jakobshavns Isbræ, West Greenland, on 9 August 1982. *Journal of Glaciology*, **33**(114), 169–172.

Evans, H. E., 1984. *Mechanics of Creep Fracture*. Elsevier Applied Science Publishers, New York.

Fett, T., D. Munz and J. Neumann, 1990. Local stress intensity factors for surface cracks in plates under power-shaped stress distributions. *Engineering Fracture Mechanics*, **36**(4), 647–651.

Glen, J. W., 1955. The creep of polycrystalline ice. *Proceedings of the Royal Society*, **228**(1175), 519–538.

Gold, L. W., 1993. *The Canadian Habbakuk Project*. International Glaciology Society, Cambridge.

Griffith, A. A., 1921. The phenomena of rupture and flow in solids. *Philos. Trans. R. Soc. London*, **A221**, 163–197.

Hanson, B. and R. L. Hooke, 2000. Glacier calving: a numerical model of forces in the calving-speed/water-depth relation. *Journal of Glaciology*, **46**(153), 188–196.

Hughes, T., 2002. Calving Bays. *Quaternary Science Reviews*, **21**, 267–282.

Hughes, T. J., 1998. *Ice Sheets*. Oxford University Press, New York.

Hughes, T. J. and M. Nakagawa, 1989. Bending shear: The rate-controlling mechanism for calving ice walls. *Journal of Glaciology*, **35**(120), 260–266.

Hulbe, C. L., D. R. MacAyeal, G. H. Denton, J. Kleman and T. V. Lowell, In press. Catastrophic Ice-Shelf Breakup as the Source of Heinrich-Event Icebergs.

Hutchinson, J. W., 1968. Singular behaviour at the end of a tensile crack in a hardening material. *Journal of the Mechanics and Physics of Solids*, **16**, 13–31.

Iken, A., 1977. Movement of a large ice mass before breaking off. *Journal of Glaciology*, **19**(81), 595–605.

Inglis, C. E., 1913. Stresses in a plate due to the presence of cracks and sharp corners. *Transactions of the Institute of Naval Architects*, **55**, 219–241.

Johnson, J. V., 2002. *A Basal Water Model for Ice Sheets*. Ph.D. thesis, University of Maine, Orono, ME.

Kanninen, M. F. and C. H. Popelar, 1985. *Advanced Fracture Mechanics*. Oxford University Press, New York.

Kenneally, J. P., In press. Comments on "Buoyancy-driven lacustrine calving, Glaciar Nef, Chilean Patagonia" by Charles Warren, Doug Benn, Vanessa Winchester and Stephan Harrison. *Journal of Glaciology*.

Kenneally, J. P. and T. J. Hughes, 2002. The calving restraint on inception of Quaternary ice sheets. *Quaternary International*, **95–96**, 43–53.

Lawn, B., 1993. *Fracture of Brittle Solids*. Cambridge University Press, Cambridge, second edn.

Lingle, C. S., T. Hughes and R. C. Kollmeyer, 1981. Tidal flexure of Jakobshavns Glacier, west Greenland. *Journal of Geophysical Research*, **86**(B5), 3960–3968.

Lythe, M. B. and D. G. Vaughan, 2000. *Bedmap - bed topography of the Antarctic. 1:10,000,000 scale map*. Bedmap Consortium, British Antarctic Survey, Cambridge.

MacAyeal, D. R., 1993. Binge/purge oscillations of the Laurentide ice sheet as a cause of the North Atlantic's Heinrich events. *Paleoceanography*, **8**(6), 775–784.

MacAyeal, D. R., T. A. Scambos, C. L. Hulbe and M. A. Fahenstock, In press. Catastrophic ice-shelf break-up by an ice-shelf fragment capsize mechanism. *Journal of Glaciology*.

Mott, N. F., 1948. Fracture of Metals. *Engineering*, **165**, 16–18.

Muskhelishvili, N. I., 1953. *Some basic problems on the mathematical theory of elasticity; fundamental equations, plane theory of elasticity, torsion, and bending*. Noordhoff, Groningen.

Nemat-Nasser, S., A. Oranratnachai and L. M. Keer, 1979. Spacing of water-free crevasses. *Journal of Geophysical Research*, **84**(B9), 4611–4620.

Paris, P. and F. Erdogan, 1963. A Critical Analysis of Crack Propagation Laws. *Journal of Basic Engineering*, **85**, 528–534.

Paris, P. C., R. J. Bucci, E. T. Wessel, W. G. Clark and T. R. Mager, 1972. An Extensive Study on Low Fatigue Crack Growth Rates in A533 and A508 Steels. In *Stress Analysis and Growth of Cracks*. American Society for Testing and Materials, Philadelphia, PA, Part I, ASTM STP 513, 141–176.

Paris, P. C., M. P. Gomez and W. P. Anderson, 1961. A Rational Analytic Theory of Fatigue. *The Trend in Engineering*, **13**, 9–14.

Parry, R. H. G., 1995. *Mohr Circles, Stress Paths and Geotechnics*. E & FN Spon, New York.

Paterson, W. S. B., 1994. *The Physics of Glaciers*. Pergammon, Oxford, third edn.

Pelto, M. S. and C. R. Warren, 1991. Relationship between tidewater glacier calving velocity and water depth at the calving front. *Annals of Glaciology*, **15**, 115–118.

Pickover, C. A., 1998. *Strange Brains and Genius: The Secret Lives of Eccentric Scientists and Madmen*. Plenum Trade, New York and London.

Reeh, N., 1968. On the calving of ice from floating glaciers and ice shelves. *Journal of Glaciology*, **7**(50), 215–232.

Rice, J. R. and G. F. Rosengren, 1968. Plane strain deformation near a crack tip in a power-law hardening material. *Journal of the Mechanics and Physics of Solids*, **16**, 1–12.

Rignot, E., 2001. Evidence for rapid retreat and mass loss of Thwaites Glacier, West Antarctica. *Journal of Glaciology*, **47**(157), 213–222.

Rignot, E. and S. Jacobs, 2002. Rapid Bottom Melting Widespread near Antarctic Ice Sheet Grounding Lines. *Science*, **296**, 2020–2023.

Rist, M. A., P. R. Sammonds, S. A. F. Murrell, P. G. Meredith, C. S. M. Doake, H. Oerter and K. Matsuki, 1999. Experimental and theoretical fracture mechanics applied to Antarctic ice and surface crevassing. *Journal of Geophysical Research*, **104**(B2), 2973–2987.

Rist, M. A., P. R. Sammonds, S. A. F. Murrell, P. G. Meredith, H. Oerter and C. S. M. Doake, 1996. Experimental fracture and mechanical properties of Antarctic ice: preliminary results. *Annals of Glaciology*, **23**, 85–102.

Rist, M. A., P. R. Sammonds, H. Oerter and C. S. M. Doake, 2002. Fracture of Antarctic shelf ice. *Journal of Geophysical Research*, **107**(B1), **ECV 1** 1–13.

Roberts, D. K. and A. A. Wells, 1954. The Velocity of Brittle Fracture. *Engineering*, **178**, 820–821.

Rooke, D. P. and D. J. Cartwright, 1976. *Compendium of Stress Intensity Factors*. Her Majesty's Stationery Office, London.

Scambos, T. A., C. Hulbe, M. Fahnestock and J. Bohlander, 2000. The link between climate warming and break-up of ice shelves in the Antarctic Peninsula. *Journal of Glaciology*, **46**(154), 516–529.

Sih, G. C., 1973a. *Handbook of Stress-Intensity Factors; Stress-Intensity Factor Solutions and Formulas for Reference*. Institute of Fracture and Solid Mechanics, Lehigh University, Bethlehem, PA.

Sih, G. C., ed., 1973b. *Methods of Analysis and Solutions of Crack Problems*. Noordhoff International Publishing, Leyden.

Sih, G. C., 1991. *Mechanics of Fracture Initiation and Propagation: Surface and volume energy density applied as failure criterion*. Kluwer Academic Publishers, Dordrecht.

Simmons, G. and H. Wang, 1971. *Single Crystal Elastic Constants and Calculated Aggregate Properties: A Handbook*. The M.I.T. Press, Cambridge, MA.

Smith, R. A., 1976. The application of fracture mechanics to the problem of crevasse penetration. *Journal of Glaciology*, **17**(76), 223–228.

Swithinbank, C., 1999. *Foothold On Antarctica – The First International Expedition (1949 - 1952) Through the Eyes of its Youngest Member*. The Book Guild Ltd, Sussex, England.

Tada, H., P. C. Paris and G. R. Irwin, 1973. *The Stress Analysis of Cracks Handbook*. Del Research Corporation, Hellertown, PA.

Thomas, R. H., 1973a. The creep of ice shelves: Interpretation of observed behaviour. *Journal of Glaciology*, **12**(64), 55–70.

Thomas, R. H., 1973b. The creep of ice shelves: Theory. *Journal of Glaciology*, **12**(64), 45–53.

Thomas, R. H., 1976. The distribution of 10 m temperatures on the Ross Ice Shelf. *Journal of Glaciology*, **16**(74), 111–117.

Thomas, R. H. and D. R. MacAyeal, 1982. Derived characteristics of the Ross Ice Shelf, Antarctica. *Journal of Glaciology*, **28**(100), 397–412.

Thomas, R. H., D. R. MacAyeal, D. H. Elvers and D. R. Gaylord, 1984. Glaciological studies on the Ross Ice Shelf, Antarctica, 1973-1978. In *The Ross Ice Shelf: Glaciology and Geophysics*, American Geophysical Union, vol. 42 of *Antarctic Research Series*, 21–53.

van der Veen, C. J., 1996. Tidewater calving. *Journal of Glaciology*, **42**(141), 375–385.

van der Veen, C. J., 1998a. Fracture mechanics approach to penetration of bottom crevasses on glaciers. *Cold Regions Science and Technology*, **27**, 213–223.

van der Veen, C. J., 1998b. Fracture mechanics approach to penetration of surface crevasses on glaciers. *Cold Regions Science and Technology*, **27**, 31–47.

van der Veen, C. J., 1999. *Fundamentals of Glacier Dynamics*. A. A. Balkema, Rotterdam.

van der Veen, C. J., 2002. Calving glaciers. *Progress in Physical Geography*, **26**(1), 96–122.

Warren, C., 1999. Calving speed in freshwater at Glaciar Ameghino, Patagonia. *Zeitschrift für Gletscherkunde und Glazialgeologie*, **35**(1), 21–34.

Warren, C. and M. Aniya, 1999. The calving glaciers of southern South America. *Global and Planetary Change*, **22**, 59–77.

Warren, C., D. Benn, V. Winchester and S. Harrison, 2001. Buoyancy-driven lacustrine calving, Glaciar Nef, Chilean Patagonia. *Journal of Glaciology*, **47**(156), 135–146.

Weertman, J., 1957. Deformation of floating ice shelves. *Journal of Glaciology*, **3**, 38–42.

Weertman, J., 1973. Can a water-filled crevasse reach the bottom surface of a glacier? *IASH Publ*, **95**, 139–145.

Weertman, J., 1977. Penetration depth of closely spaced water-free crevasses. *Journal of Glaciology*, **18**(78), 37–46.

Weertman, J., 1980. Bottom crevasses. *Journal of Glaciology*, **25**(91), 185–188.

Weertman, J., 1996. *Dislocation Based Fracture Mechanics*. World Scientific, New Jersey.

Zotikov, I. A., 1986. *The Thermophysics of Glaciers*. D. Reidel Publishing, Dordrecht.

APPENDIX A

LOSSES BY MELTING: BYRD GLACIER

Overview

Byrd Glacier is an outlet glacier located in a fjord through the Transantarctic mountain range, draining ice from the higher elevation, relatively stable ice of East Antarctica to the Ross Ice Shelf. The glacier passes through a fjord approximately 35 km wide before emerging into the Ross Ice Shelf, which is the largest ice shelf in Antarctica with an area of approximately 520,000 km^2 and ice from 200 to 2000 m thick. Henry Brecher of The Ohio State University in December 1978 and January 1979 measured numerous elevations and displacements with the use of aerial triangulation from two sets of aerial photography (Brecher, 1982). The data coverage included points on the ice stream located upstream and downstream of the glacier's assumed grounding zone. In total, 471 velocity measurements were obtained as well as 1003 elevation measurements. These data provide a substantial coverage of the glacier in the fjord as well as some coverage onto the Ross Ice Shelf itself (Figure A.1).

Using these data, mass losses or gains to Byrd Glacier can be determined by employing a conservation of mass argument. The mass flux through the grounding line must be conserved at all points subsequent to the grounding line. Determining the flux is simple, since the velocity data describe how fast the ice is moving through the fjord and, at least for the floating portion of the ice, the elevation data are an indirect measurement of the overall ice thickness. It is assumed that mass loss or gain due to surface ablation or accumulation is negligible, thus all losses or gains will be due to basal melting or refreezing.

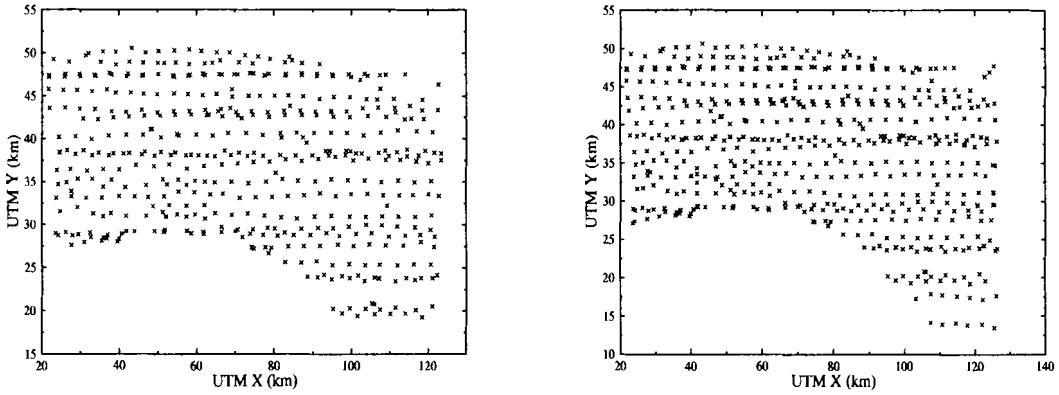

(a) Velocity (b) Elevation

Figure A.1: Velocity and elevation data coverage on Byrd Glacier. Axes are UTM grid.

Determination of the Grounding Line

In order to begin a conservation of mass calculation, a reasonable location of the grounding line is needed. In fact, it is believed that Byrd Glacier has a grounding zone that is influenced by effects such as the tide, rather than a static grounding line that remains constant regardless of outside influences. For the purposes of calculation, a single grounding line needs to be specified. A simple way to do this is to examine the average elevation of the ice and locate the point where the down-glacier slope of the ice approaches zero.

To determine average elevation and velocity profiles for the glacier, the data shown in Figure A.1 are broken into data slices perpendicular to the flow. Average quantities for elevation and velocity are then determined for each slice. The data slices are located as shown in Figure A.2.

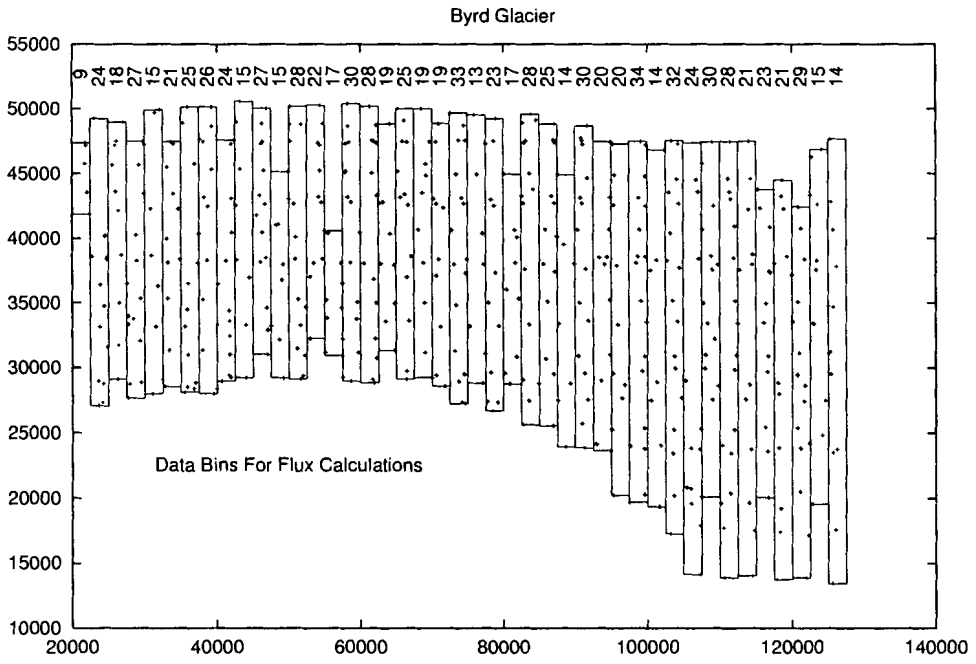

Figure A.2: Data slices created for calculating the average profile values of velocity and elevation. The numbers across the top of each bin represent the number of elevation measurements located within that slice. Each slice is 2500 m wide and flow is to the right.

Velocity Profile

Each velocity measurement lying within a single slice is averaged together with all other measurements located in that same slice to get a profile of the average velocity. It should be noted that because of the confines of the fjord walls, the motion of the ice is almost entirely longitudinal, with divergence only occurring near the entrance to the ice shelf. Velocity vectors can be seen in Figure A.3(a). Using the slices shown in Figure A.2 and assigning each slice the average velocity for the data contained within that slice, the average velocity profile is determined. The results are shown in Figure A.3(b).

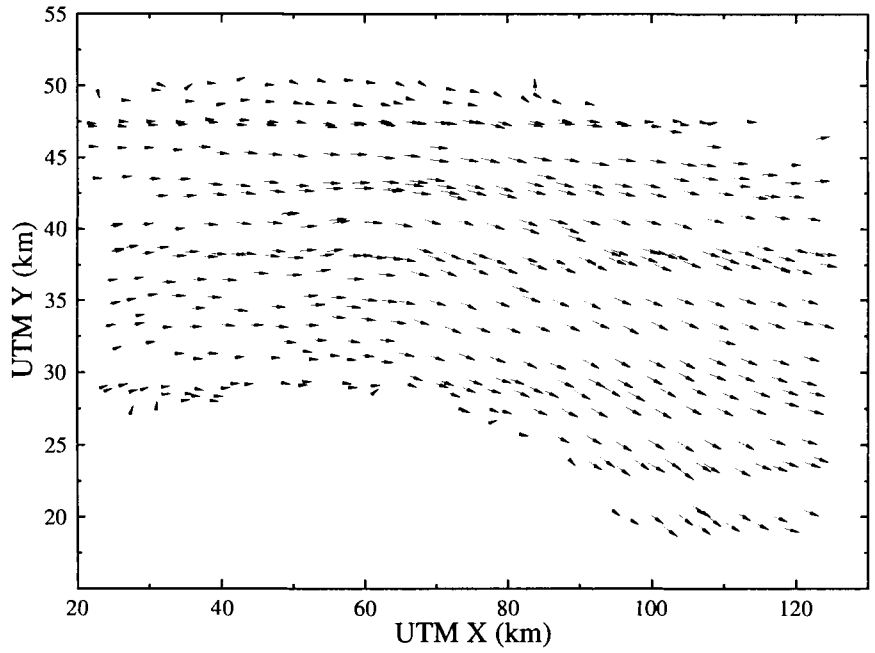

(a) Velocity vectors.

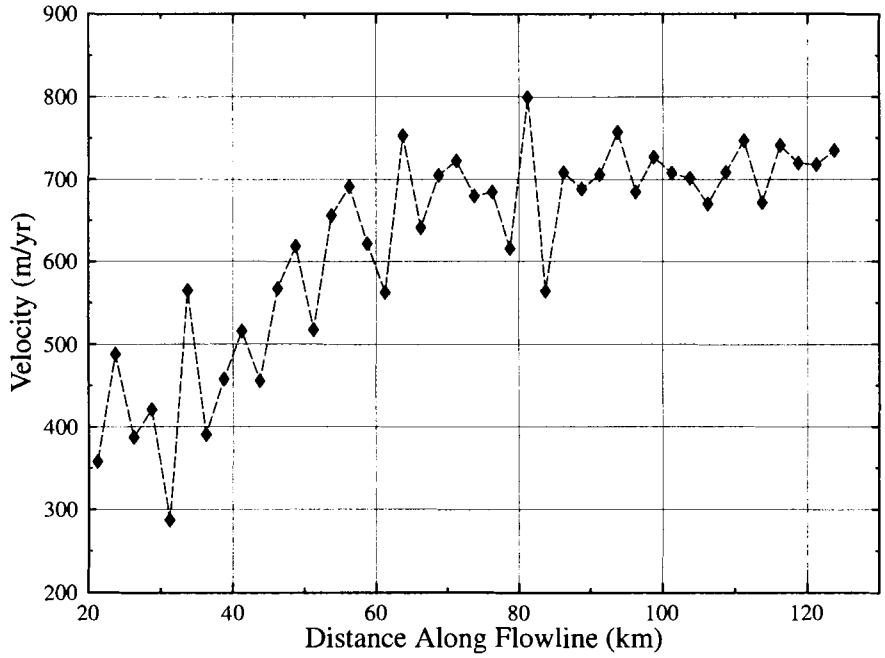

(b) Average velocity profile.

Figure A.3: Calculated velocity data for Byrd Glacier. The velocity approaches a nearly constant value at points downstream from $x = 80\,\text{km}$.

Elevation Profile

The elevation profile is found in the same manner as the velocity profile. From Figure A.4, an initial guess of the location where the ice becomes afloat can be made. Using the argument given earlier, the surface slope seems to approach zero somewhere in the region 70,000 m$< x <$75,000 m. In order to determine a single location for the grounding line, a numerical derivative of the data must be taken. Finding the point where the derivative goes to zero, i.e. where the surface slope becomes constant, will determine a location for the grounding line. In order to really see any trend that is occurring within the data a smoothing algorithm called a moving average is employed.

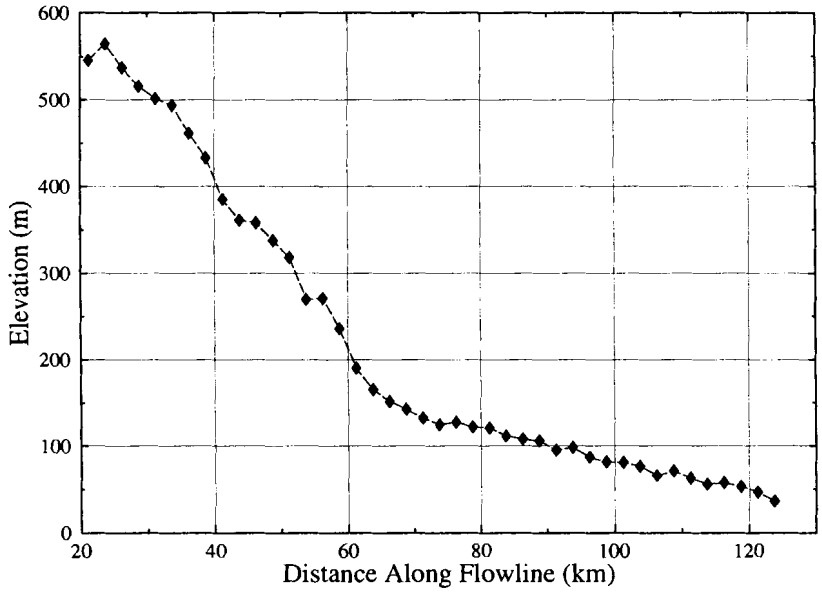

Figure A.4: Average elevation profile for Byrd Glacier.

The moving average is a simple data smoothing algorithm that is used to find trends in normally noisy data. It is defined as follows: Given a sequence of numbers $\{a\}_{i=1}^{N}$, the *n-moving average* is a new sequence $\{s\}_{i=1}^{N-n+1}$ defined from the a by taking an average of subsequences of n terms

$$s_i = \frac{1}{n} \sum_{j=i}^{i+n-1} a_j \tag{A.1}$$

As an example, consider the 3-moving average. In this case, Eq. A.1 will give a new set of data s

$$s = \frac{1}{3}\left(a_1 + a_2 + a_3, a_2 + a_3 + a_4, \ldots, a_{N-2} + a_{N-1} + a_N\right)$$

where N is the total number of data points.

Results found by smoothing the derivative data using a moving average with n equal to 3 and 5 are shown in Figure A.5, along with the unsmoothed derivative data. The derivative appears to be close to zero along all points of the flowline, but the data all approach a constant and nearly zero value at approximately $x = 80\,\text{km}$. Using these results, it is estimated that the approximate grounding line for use in subsequent calculations is located at $x_g = 80\,\text{km}$.

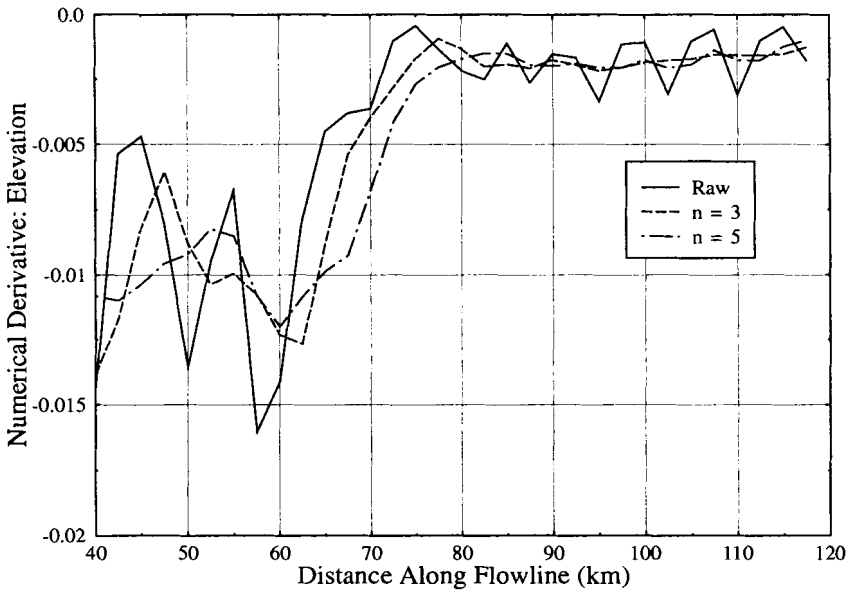

Figure A.5: Smoothed data representing the derivative of surface slope. The data converge to a stable and nearly zero value at $x = 80\,\text{km}$.

Flux

With a determination of the grounding line, it is now possible to find the mass balance for the floating portion of Byrd Glacier using a flux calculation. Any ice that flows over

the grounding line must be conserved at downstream points along the flowline. The initial flux of ice, Φ_o, will either remain the same at later points, increase, signifying a gain of mass, or decrease, signifying a loss of mass. It is then possible to determine a rate of mass loss or gain using the results of the flux conservation calculation.

The flux through a region is defined as

$$\Phi = \vec{A} \cdot \vec{v} \tag{A.2}$$

where $\vec{A}$ is the area of the region in question and $\vec{v}$ is the velocity of the material through that area. The area and the direction of flow may not necessarily be perpendicular to one another so the dot product picks out the component of flow that is normal to $\vec{A}$ (see Figure A.6).

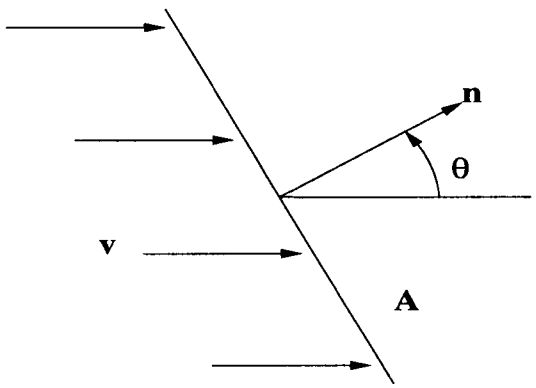

Figure A.6: Geometrical representation of the flux through a surface with area $\vec{A}$ and material velocity $\vec{v}$.

For mathematical purposes, an outward unit normal vector $\hat{n}$ is defined as shown in Figure A.6. The vector area is then written as $\vec{A} = A\hat{n}$. Given the picture shown in Figure A.3(a), velocity and area are very nearly perpendicular throughout the flow. Because of this fact, only considering flow lateral to the fjord walls is a valid assumption. The flux for the i^{th} data slice from the grounding line on is then calculated as

$$\Phi_i = W_i \langle H \rangle_i \langle v \rangle_i \tag{A.3}$$

where $\langle H \rangle$ and $\langle v \rangle$ are average values taken from the profile calculations done earlier and W_i is taken as the maximum extent of the data coverage in the transverse y-direction for the i^{th} slice. The flux is plotted in Figure A.7.

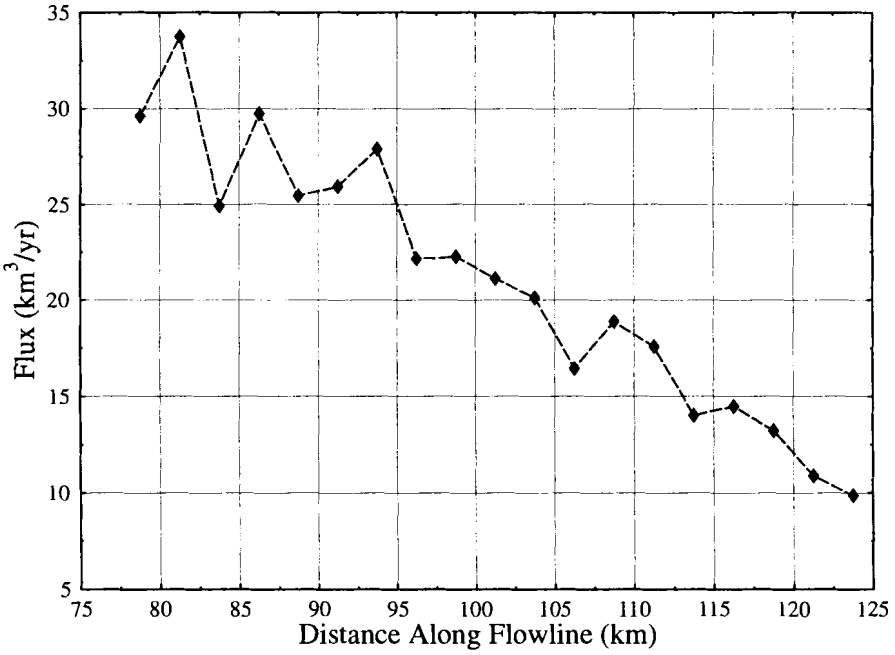

Figure A.7: Flux in km^3/yr for the floating portion of Byrd Glacier. The flux is decreasing along the flowline profile, indicating mass loss.

Melt Rate

Once a calculation of the flux through a given slice is made, it must be determined if the flux has been conserved between slice i and $i+1$. If they are not equal, mass has been added or removed from the system from an outside source. Since surface ablation and accumulation are nearly zero, basal processes are assumed to be the dominant factor in any mass imbalance. These processes could be either basal melting or local basal refreezing. The term melt rate will be used for both, with a negative melt rate signifying actual melting and a positive melt rate signifying refreezing.

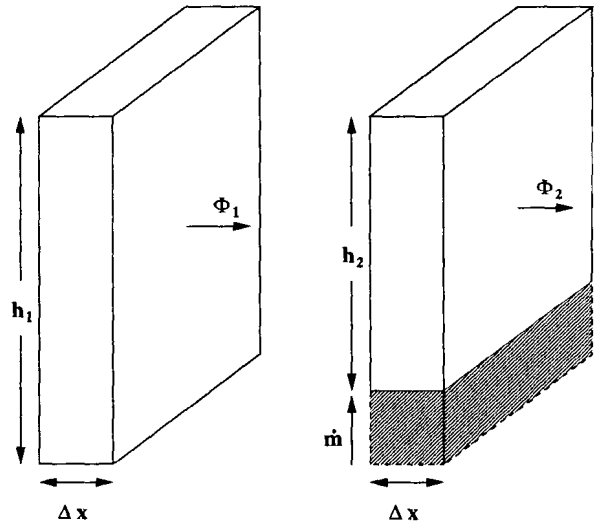

Figure A.8: Illustration demonstrating basal melting between two consecutive data slices. If $\Phi_2 \neq \Phi_1$ the hatchured portion must be melting at a rate $\dot{m}$ in order to conserve mass.

Figure A.8 gives a pictorial description of basal melting. As the flux changes from slice i to slice $i+1$, the melt rate is found by taking the difference in fluxes and dividing by the surface area between the slices

$$\dot{m}_{i+1} = \frac{\Phi_{i+1} - \Phi_i}{\Delta x \, W_{i+1}} \tag{A.4}$$

The melt rate along the floating portion is shown in Figure A.9. The results in Figure A.9 are wildly erratic, with extreme points ranging from -90 $^{m}/_{yr}$ to 50 $^{m}/_{yr}$. These extreme points are located nearest to the assumed grounding line, and the data do tend to smooth out slightly farther downstream. An overall melt rate, found by simply averaging the results, yields $\langle \dot{m} \rangle = -11.8\,^{m}/_{yr}$. To see if this is indeed an accurate representation of the melt rate, the moving average is once again employed. The data are smoothed using values of n equal to 3 and 5 to determine what constant value they approach.

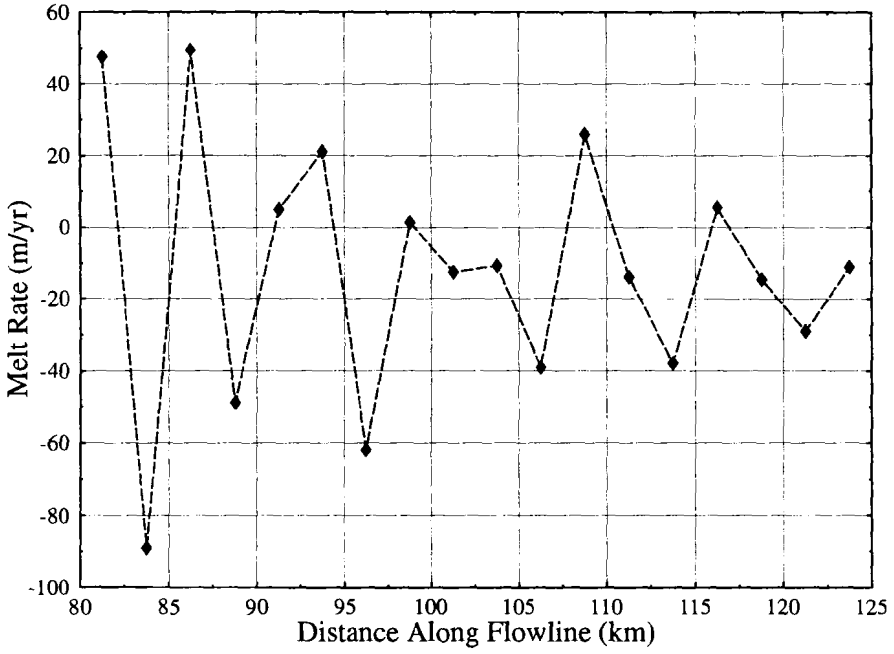

Figure A.9: Melt rate $\dot{m}$, measured in m/yr, calculated using Eq. A.4 for consecutive data slices.

The overall melt rate for the raw and smoothed data is summarized in the following table:

Smoothing Value n	Average Melt Rate $\langle \dot{m} \rangle$ ($^{m}/_{yr}$)
Raw	-11.8
3	-12.3
5	-12.6

An exact value of the melt rate is not the goal of this calculation. However, with the numerical values presented and the results plotted in Figure A.10, it is safe to assume that Byrd Glacier is experiencing mass loss along its floating portion, which is most likely due to bottom melting. With this knowledge, assumptions can be made when calculating the temperature profile for use in the stress analysis on Byrd, which was the goal of this section.

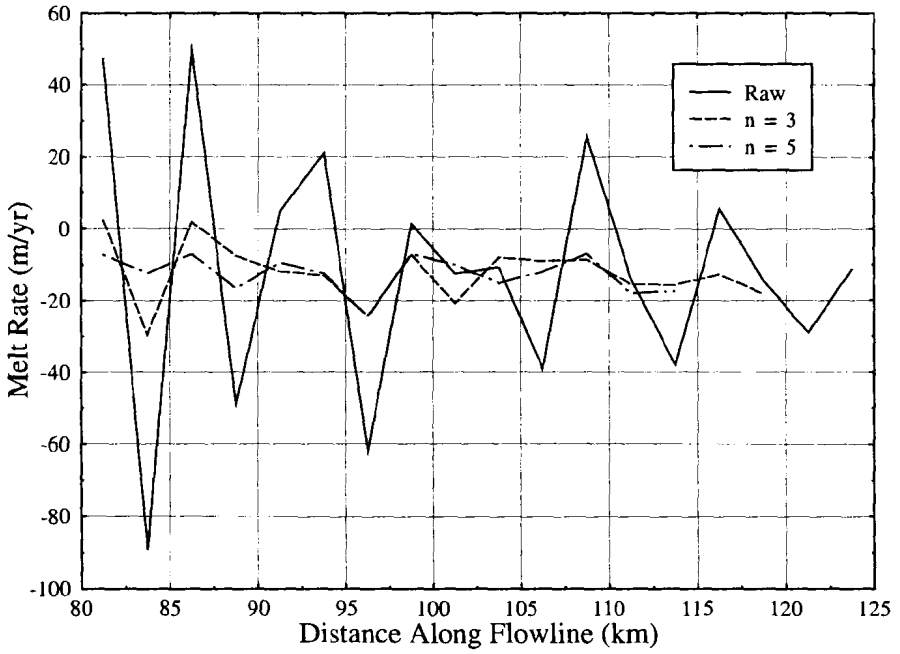

Figure A.10: Smoothed melt rates for the the data shown in Figure A.9. An overall average is taken for each to see where $\dot{m}$ converges.

An average melt rate on the order of $\langle \dot{m} \rangle \approx -10\,^{\mathrm{m}}/_{\mathrm{yr}}$ for the floating portion of Byrd Glacier is not unreasonable; work done on Thwaites Glacier (Rignot, 2001) as well as other areas in Antarctica (Rignot and Jacobs, 2002) has resulted in similarly high melt rates.

APPENDIX B

A STRANGE BRAIN INDEED

There are always those who are willing to disregard what others may think and act on what they believe is right, regardless of the repercussions to their character or career. The field of glaciology has many colorful characters even to this day, but perhaps one of the most colorful, influential, and still least known was Geoffrey Pyke. (The title of this section comes from Pickover (1998), which illustrates the unfortunate correlation between truly original scientific thinkers and the rates at which they suffer from mental illness. Historical information presented here is condensed from this book.) Pyke was an Englishman who worked primarily as an inventor, but he also spent much time working in numerous other fields such as philosophy, economics, finance and journalism. Pyke also suffered from several mental illnesses, including hypergraphia (excessive writing) and depression. Around the time that the English were suffering heavy losses due to the sinking of their supply ships in the North Atlantic by the Germans, the English government put forth the challenge to come up with some way to help thwart the German attacks and maintain the supply routes through the North Atlantic shipping channels. Pyke came up with the idea of an "ice navy," where all ships would be built out of the easily renewable and readily found material. These ships would be built from a mixture of ice and wood chips called "pykrete," which Pyke believed would raise both the strength of the ice and the melting point, creating an armada that was impervious to attack and environmental factors. Prime Minister Winston Churchill and Lord Louis Mountbatten, who was Chief, Combined Operations (a group that organized and planned combined military operations) were intrigued and set Pyke's idea in motion by starting the Habbakuk

Project in northern Canada (Gold, 1993). It was during this project that many in-depth studies into the physical properties of ice were conducted for the first time. Prior to this study, ice had not been considered for use as a construction material. Thus, inquiries into the physical properties of ice were neglected. In order to realize Pyke's idea of an ice navy, values for the ice strength were necessary. Experiments to determine this were undertaken for large scale ice structures, as well as ice properties for a range of temperatures and wood/ice mixtures. The pykrete that was created was bombed, shot, torpedoed, and dropped in hot water with little or no damage inflicted. Ice ship mockups were built and one even survived an entire summer in Canada. Sadly for Pyke (but happily for everyone else) the war neared its end and the ice ship navy became unnecessary. One observer has noted that if an ice ship had actually been built and employed, it would have been "the second most spectacular device of the war, outshadowed only by the atomic bomb" (Pickover, 1998, pg. 150). Pyke continued with his furious pace of creating new ideas for a few more years until he ultimately committed suicide in 1948, for reasons that are unclear.

While Pyke may have toiled in a self-inflicted obscurity for the time he was alive, it was his vision and commitment to an idea, no matter how outrageous it may have seemed, that has lasted well beyond his time.

BIOGRAPHY OF THE AUTHOR

James Kenneally was born in Coventry, Rhode Island during the hot summer. At the age of five he moved to Rehoboth, Massachusetts, where his family resides to this day. He graduated from Dighton-Rehoboth Regional High School and attended Rensselaer Polytechnic Institute in Troy, New York, where he was awarded a Bachelor of Science degree in physics with a minor in mathematics. He later enrolled at the University of California, San Diego where he earned a Master of Science degree in physics. He enrolled at the University of Maine in September of 1999.

James is a candidate for the Doctor of Philosophy degree in Physics from The University of Maine in August, 2003.